Development of An Atomic Force Microscope and Measurement Concepts for Characterizing Martian Dust and Soil Particles

Dissertation
Submitted to the faculty of Sciences of the University of Neuchâtel, in fulfillment of the requirements for the degree of "*Docteur ès Sciences*"

by

Sebastian Gautsch

Diplômé en électronique-physique
de l'Université de Neuchâtel

Institute of Microtechnology
University of Neuchâtel
Rue Jaquet-Droz 1, CH – 2007 Neuchâtel
Switzerland

July 2002

IMPRIMATURE

Abstract

The present thesis is devoted to the development of a space qualified atomic force microscope (AFM) for a robotic mission to Mars. The working principle of such an instrument relies on a sharp tip at the end of a soft cantilever, which senses the topography of a surface. The main objective of the AFM is the characterisation of small dust particles present in the Martian soil and atmosphere. It is part of a microscopy experiment onboard the scientific payload MECA. This payload focuses on the assessment of harmful effects that human explorers would have to face on the surface of Mars.

In a first assessment, bulkiness, high sensitivity and required interaction between the instrument and an operator render atomic force microscopy unsuitable for planetary missions. However, microfabrication technologies combined with innovative design ideas allowed to build an error tolerant system with functionality for addressing the challenges generated by a 9-month space travel and the Martian surface conditions. The AFM passed all the space-qualification tests and has been delivered to NASA.

It has been shown that the instrument is able to characterize dust particles in the expected size range of Martian dust (0.2 - 3 μm in diameter). Properties like shape, size distribution, hardness and mass can be assessed using different measurement techniques. The advantage of the presented instrument over commonly used dust analysis techniques is the much higher resolution (down to a few nanometers) and its small size and weight. Without the electronics that drive the instrument, it has the size of a matchbox and weights 15g.

Based on the instrument behavior at simulated Martian conditions, and on AFM images obtained by measuring Mars equivalent samples, operational concepts for autonomous measurements have been developed.

Until this day, prediction on the mineralogical composition of the airborne dust of Mars relies on theoretical diffraction models where the particles size distribution plays a major role. Scientific results returned by the AFM will start new investigations in this field and limit the speculations on mineral composition.

The genuine topography of dust samples, as they would be returned from Mars at the present status of the instrumentation, would be affected by the measurement concepts and by technical limitations. To improve the image quality at low temperatures and the reliability of particle measurements, several developments for future work are proposed.

The first opportunity for this AFM to fly to Mars has been cancelled in the year 2000 due to back-to-back loss of two robotic Mars missions (Mars Climate Orbiter and Mars Polar Lander). However, new scientific studies and field-testing with the presented instrument have been proposed recently to promote its candidature for a new flight to Mars.

Résumé

Le sujet de cette thèse porte sur le développement d'un microscope à force atomique (AFM) qualifié pour l'espace. Son principe de fonctionnement est basé sur une pointe très effilée montée à l'extrémité d'un levier qui mesure, par balayage, la topographie d'une surface. Intégré dans une mission scientifique nommée MECA, son objectif principal est la caractérisation de fines particules de poussières du sol et de l'atmosphère martienne. MECA est dédiée à l'évaluation des effets nuisibles de l'environnement martien auxquels les futurs explorateurs humains seraient exposés.

A première vue, l'AFM est u instrument mal adapté à l'exploration planétaire du à son volume excessif, à sa haute sensibilité et aux fréquentes interactions avec l'opérateur. Pourtant, les progrès technologiques de la microfabrication et les idées innovantes ont permis de construire un système faisant face aux défis générés par un voyage spatiale de neuf mois et par les conditions drastiques régnants à la surface de Mars. L'AFM a passé avec succès les tests de qualifications spatiales et a été soumis à la NASA.
Il a été démontré que l'instrument est capable de caractériser des particules de taille équivalente aux poussières présentes sur Mars (entre 0.2 et 3 μm de diamètre). Des propriétés telles que la forme, la distribution de taille, la dureté et la masse peuvent être évaluées en utilisant différentes techniques de mesures. Les avantages de cet AFM par rapport à d'autres techniques d'analyses sont sa résolution plus élevée (quelques nanomètres), sa miniaturisation et sa légèreté. Sans l'électronique qui contrôle l'instrument, il a la taille d'une boîte d'allumettes et pèse 15 g.
En simulant le comportement de l'instrument en conditions martiennes, et par la mesure d'images AFM de poussières équivalentes, des concepts de fonctionnements autonomes ont été développés.
A ce jour, les prédictions sur la composition minéralogique des particules suspendues dans l'atmosphère martienne se basent sur des modèles théoriques de diffraction où le paramètre de distribution de taille des poussières est prédominant. La restriction de ce paramètre grâce aux résultats scientifiques pouvant être obtenus avec cet AFM permettrons de limiter les spéculations sur la nature des minéraux.
Dans l'état actuel de l'instrumentation, la topographie authentique des échantillons de poussières martiennes serait altérée par les concepts de mesures et des limitations techniques. Afin d'améliorer la qualité des images à basse température et la fiabilité des techniques de mesures, plusieurs développements pour de futurs travaux sont proposés.
La première opportunité de vol sur Mars pour cet instrument a été supprimée en 2000 suite à la perte consécutive de deux missions robotiques (Mars Climate Orbiter et Mars Polar Lander). Néanmoins, de nouvelles études scientifiques et des tests en conditions réelles avec l'instrument ont été proposées récemment pour promouvoir sa candidature pour un nouvel envol vers Mars.

1. INTRODUCTION

The FAMARS (First Afm on Mars) instrument presented in this thesis has been specifically designed to measure small dust particles of the Martian soil. To give the reader a general overview, the first section of this introduction chapter describes the objectives of this work and how the FAMARS project came to realization. It also describes how this thesis is structured. The other sections of this chapter are dedicated to introducing the reader to the different topics related to this work:

Section 2 describes the global characteristics of Mars to highlight the differences between our neighbouring planet and Earth. It also describes the general topography and surface features to understand the environmental conditions the FAMARS instrument will face, once it will have arrived on Mars.

The scientific interest in characterizing the airborne particles present in the Martian atmosphere is very high since it helps to understand the seasonal variation of the Martian climate and the geological history of the planet. During the last 30 years, the size, shape and composition of the Martian dust has been evaluated by using analytical models to match the data returned by scientific instruments. Until this day, individual particles have never been measured in terms of size and shape. The characterization of individual dust particles will be the principle goal of the FAMARS instrument. The third section of this introduction focuses on the theoretical characteristics of the dust particles inferred by previous Mars missions. As this review is chronologically structured, it will also give the reader an overview on the history of robotic exploration of Mars. As the FAMARS AFM will help to assess the risks for a manned mission to Mars, the final part of this section is dedicated to the current status of planning a human Mars expedition.

The FAMARS instrument is part of the scientific payload MECA (Mars environmental compatibility assessment). Section 4 of this introduction describes the general architecture and the scientific goals of each instrument of this payload. It also highlights the interactions between the AFM and the other instruments. One of the goals of MECA is the detection of quartz particles in the dust and soil of Mars. The abundant presence of this mineral on Mars would be a serious threat to a manned mission to Mars for engineering and health issues. Therefore, the fourth section also gives an overview on silicosis, the most likely disease that human explorers would be confronted with, if small quartz particles in the respirable size range were present on the planet's surface. In the end of 1999, 2 missions sent to Mars by NASA were lost due to very regrettable reasons. This caused the cancellation of MECA's opportunity

to fly to Mars in 2001. The end of this section describes the circumstances under which the 2001 opportunity to send a lander to Mars was cancelled and what new opportunities will be available for MECA in the years to follow.

The AFM designed in this work is a microscope that will return topographic images of dust particles from Mars with a resolution in the order of a few nanometers. The working principle of such an instrument is described in the fifth section of this introduction. It describes the different design options that were available to build an instrument that could work on an autonomous basis. As the AFM is used in many application fields but was, to my knowledge, never used to image micrometer-sized dust particles, a paragraph is dedicated to the common applications of AFM.

The heart of the FAMARS microscope is a small chip microfabricated in silicon. The fabrication techniques used to shape the tiny structures of this chip are generally used to fabricate MEMS (micro electro mechanical systems). The last section of this introduction chapter describes the advantages of using such devices in space applications.

1.1 Scope, objectives and structure of this thesis

In August 1998, the engineering team of the scientific payload MECA (Mars environmental compatibility assessment) approached IMT for designing and building a space-qualified atomic force microscope. This AFM would be part of the microscopy station of the payload to characterize Martian dust particles. At that time, MECA was selected to fly to Mars with the Mars Suveyor 2001 Lander, which would be launched to Mars in April 2001, and arrive at Mars in February 2002.
IMT's background in the field of AFM was already known through previous research projects where AFM tips and other probes based on different technologies have been developed. Its well-equipped facilities for creating small structures in silicon would enable the fabrication of the required tips and cantilevers of the instrument.
At that time, IMT was working on the development of an array of AFM probes based on CMOS detection for fast scanning application called FAMOS (Fast scanning probe microscopes on silicon) [1]. This project was funded by the Swiss priority program for the development of new technologies called MINAST. As the development of an AFM for Mars would necessitate the fabrication of an array of cantilevers and tips, it would fit the project outline of FAMOS. Thus, the necessary funding source could be rapidly obtained for the Mars AFM project. This project was since then called FAMARS, which stands for "first AFM on Mars".
Due to close collaboration on previous projects with the company Nanosurf AG, the electronics department of the University of Basel and the CSEM (centre Suisse d'électronique et de microtechnique), all the partners for developing such an instrument were brought together.

Nanosurf was developing a new scanner for their commercial AFM based on electromagnetic actuation. This scanner would fit the power and environmental requirements specified by the engineers of MECA.
The electronics department of the University of Basel had collaborated with IMT on the development of the amplifying unit for the FAMOS project and was working on the electronics of the commercial AFM of Nanosurf. It was therefore the ideal partner for designing and building the electronics for the FAMARS instrument.
To be able to image hard particles without wearing the tip apex, hard tips needed to be implemented. The CSEM masters the technology of creating diamond tips in silicon moulds and due to the fact that it was IMT's neighbour, was the right institution to work with.
The objectives of this thesis have been clear from the day the agreement with the microscopy team of MECA was signed, namely:

- Providing an AFM to MECA to image micrometer-sized particles with a resolution approaching the nanometer.
- Characterizing the instrument under Mars equivalent conditions
- Implementing the instrument into the MECA payload
- Developing autonomous measurement cencepts for the instrument
- Showing the feasibility of imaging loose particles on a substrate by AFM
- Creating a database of particle images of Mars equivalent samples
- Establishing safe AFM measurement techniques to increase the scientific throughput of the mission

These objectives can be divided into 2 distinct categories, engineering and science. Thus, the structure of this work is divided into 2 main parts. The chapter entitled "FAMARS design" describes the architecture, the characterization and the mission specific operations schemes of the instrument. The following chapter entitled "particle measurements" focuses on the performed measurements and the special techniques developed to image small particles.

1.2 The planet Mars

Mars, the fourth planet from the Sun, is more like Earth than any other body in our solar system. It has mountains and valleys, polar ice caps and dry riverbeds. It has seasons, an atmosphere with clouds, winds and dust storms, and a solid rocky surface covered with dust.
Compared to all the other known planets besides our own, Mars also has a relatively moderate climate. As a result, Mars is the only place other than the Moon that humans can realistically think about exploring.
Mars is only half as large as our planet. Its thin atmosphere is comprised of about 95 percent carbon dioxide (CO_2). Its atmospheric pressure is about 100 times less than on Earth. The sunlight that reaches Mars is only half as intense as on Earth. This makes of Mars a very cold place on a human perception scale. In winter, the temperatures often fall to about minus 120 degrees Celsius. Table 1-1 summarizes some general data about Mars and compares it to those of Earth [2].

Table 1-1
Basic information about Mars.

	Mars	**Compared to Earth**
Mass:	6.42 x 1023 kg	0.1074 Earth-mass
Gravitation constant:	3.73 m/sec^2	9.81 m/sec^2
Diameter:	6786 km	0.26 Earth diameter
Mean distance from the Sun	227.9 x 10^6 km	149,6 x 10^6 km
Mean orbital velocity:	24.13 km/sec	29.79 km/sec
Length of year:	687 days	1.88 Earth-year
Length of day:	24 h 39 min 35 sec	1.02 Earth-days
Number of satellites:	2 (Phobos and Deimos)	1 (the Moon)
Mean air pressure:	7 mbar	1013 mbar
Sunshine:	88 J / cm^2 / day	200 J / cm^2 / day
Surface temperature range:	- 133 to + 22 °C	- 73 to + 72 °C

Mars has many interesting geological features on its surface that first became apparent with the spacecraft Mariner 9 that orbited Mars in the early 70's. These surface features were subsequently studied by the Viking (1976) and Pathfinder (1997) Landers. Many of them are visible from the Hubble Space Telescope as well:

Volcanoes

The volcanoes on Mars are now extinct, but they indicate a preceding period of significant Martian volcanism. The largest volcano is called *Olympus Mons*, and is 600 km across its base and about 25 km above the surrounding plain, which is about 2 $^{1}/_{2}$ times the height of Mount Everest. The inset of Figure 1-1 shows a satellite view of the volcano.

Canyon Systems

The Martian surface has some large canyon systems. The largest is Valles Marineris, which extends for about 5000 km, is 500 km wide, and as much as 6 kilometers deep Figure 1-1 shows an image of the planet Mars with the entire Valles Marineris.

Polar Caps

Mars has polar caps that wax and wane with the Martian seasons. These polar caps appear to be partially composed of frozen carbon dioxide (dry ice) and frozen water.

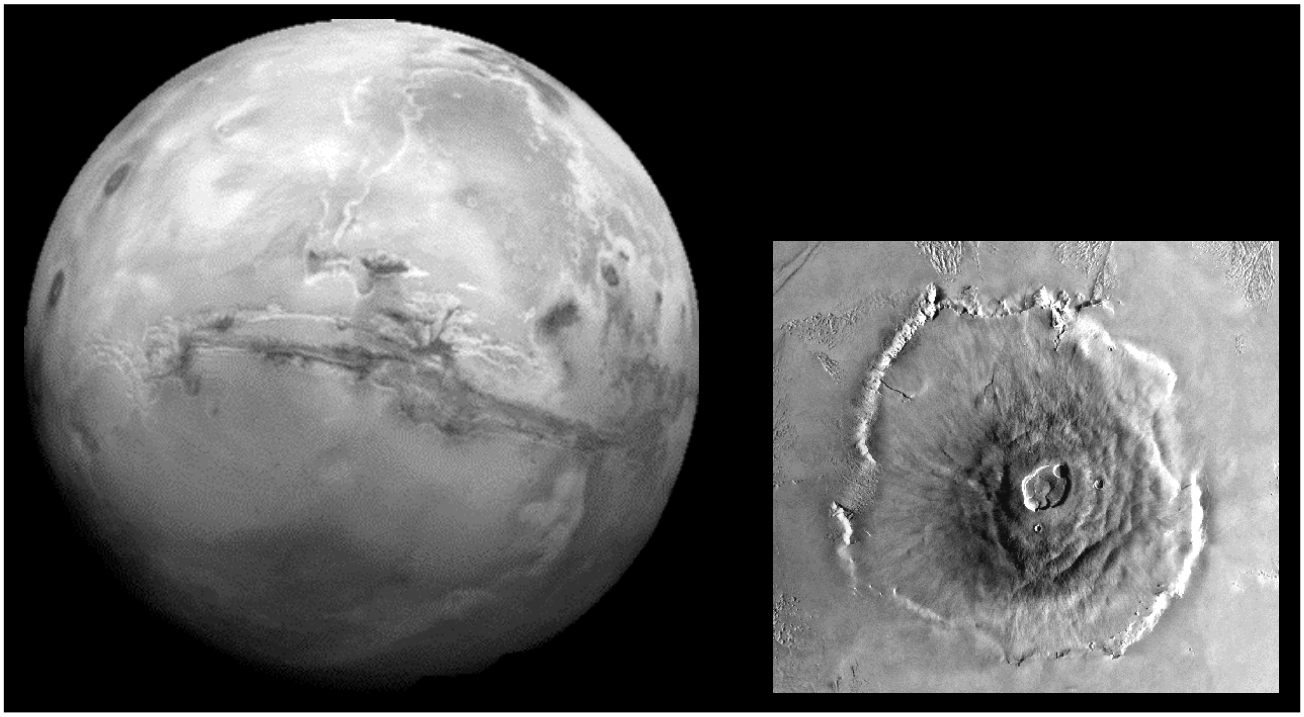

Figure 1-1

The Valles Marineris canyon system. The mosaic is composed of 102 Viking Orbiter images of Mars. The three Tharsis volcanoes (dark spots), each about 25 km high, are visible to the west. The inset image shows a close-up view of the Olympus Mons volcano.

Surface features

The landing site inferred by the Pathfinder mission in 1997 shows a surface covered by rocks ranging from a few centimetres (boulder and cobble) to as large as 7 m. A mix of ground-up rock and fine dust, called regolith[1] covers the ground on Mars. These fines, which have a broad size range, can be divided into two broad classes of materials:

- Soil: unconsolidated particulate material that is originated by environmental factors like climate and host rock mineralogy.
- Dust: Most fine grained component of the soil, which can be easily transported by Aeolian processes.

Red deposits on the upper surface of many rocks at the landing site are inferred to be dust settled from suspension in the atmosphere. Figure 1-2 shows a panoramic view of the landing site of the Pathfinder mission.

Figure 1-2

Panoramic view of the Pathfinder landing site showing a planetary surface covered with rocks and fine-grained soil. The 2 hills visible at the horizon have been called the "Twin Peaks".

Dust devils and dust storms

The major temperature control of the atmosphere is the amount of dust in the atmosphere [3]. Pressure and temperature can undergo rapid changes accompanied by spinning, columnar vortices of wind also called dust devils [4]. More global events can entrain the dust into suspension called dust storms [5]. During 2001, a dust storm of massive proportions has been raging over almost the entire surface of Mars. Such a global dust storm has not been seen on Mars for several decades. It has raised a cloud

[1] Regolith: fragmental and unconsolidated rock material that forms the surface of land and overlies the solid rock.

of dust that engulfed the entire planet for over four months [6]. As the Sun warmed the airborne dust, the upper atmospheric temperature has been raised. Figure 1-3 shows images of Mars taken by the orbiter Mars Global Surveyor (MGS) before and during the dust storm of 2001.
Dust devils and dust storms may also have an important geological influence on Mars. In fact, they may be the primary soil erosion process, since the thin atmosphere of Mars supports high velocity winds that are correlated with solar heating of the surface. Chapter 1.3 gives a more detailed description of the dust characteristics.

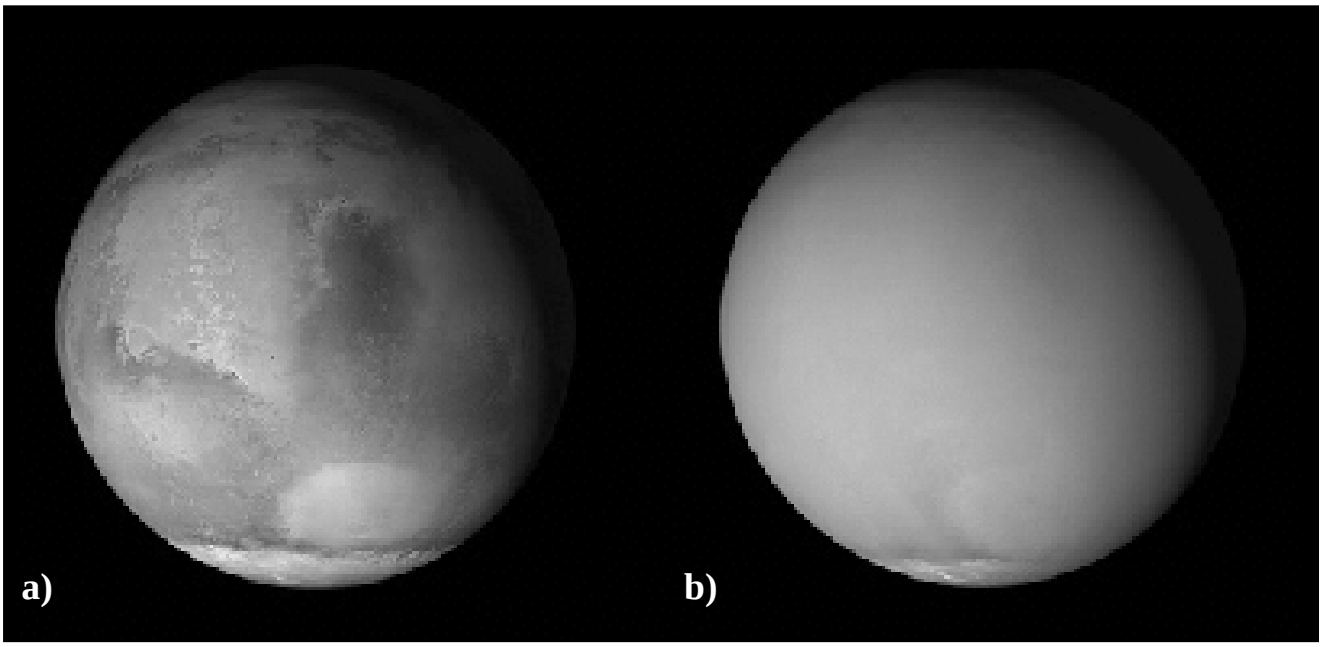

Figure 1-3
Global dust storm of summer 2001 taken by the MGS' Mars Orbiter Camera (MOC). Picture a) was taken before (June 10) and picture b) during the dust storm (July 31). [7]

Radiation
A continuous flux of galactic cosmic rays (GCR) produced by supernovae and occasional but intense fluxes of solar energetic particles (SEP) impose hazards on expeditions in outer space. Unlike earth, which is inside a protective magnetic field called the magnetosphere, Mars does not have a magnetic field to shield it from solar flares and cosmic rays (Mars' internal magnetic dynamo turned off about 4 million years ago). This constant radiation can account for most of the planet's lost atmosphere by solar wind erosion. Today, the atmosphere of Mars is only one percent that of Earth's, making it very thin to block or absorb most types of radiation from space.

1.3 Martian dust and soil

By understanding the mineralogy of the surface materials on Mars, insight into the availability of liquid water, and the duration, mode, and extend of weathering occurring throughout the Martian history can be provided. As found by the in situ experiments on Mars, silicon (Si) and iron (Fe) are the two most abundant elements [8], but how these are combined into surface minerals has not been directly determined. Section 1.3.1 gives a general overview on mineral and rock classification to better understand the prediction on mineralogical composition of the Martian dust
Dust aerosols are always present in the Martian atmosphere. Their presence significantly affects the thermal structure of the atmosphere. They absorb solar radiations in the visible wavelength while emitting in the infrared. Section 1.3.2 gives an overview on the Radiative properties of the Martian atmosphere and the influence of dust in the thermal emission spectra.
Analysis of the chemical composition of the Martian atmosphere had been performed since the invention of astronomical spectroscopy in the 1860s, using the sunlight reflected off the Martian surface. Infrared imaging from Orbiters or landing sites have been analysed for the last 30 years to gain information on size distribution, vertical profile and composition of the atmospheric dust. Section 1.3.3 gives a chronological overview of the history of Mars exploration and the inferred characteristics related to airborne dust.

1.3.1 Classification and characteristics of common rocks and soils

This section gives an overview of the classification of minerals, rocks and soils [9]. It also describes the techniques commonly used to characterize and distinguish different minerals.

1.3.1.1 Mineral and rock classification

A mineral is an inorganic natural solid, which is found in nature. Its atoms are arranged in definite patterns and it has a specific chemical composition that may vary within certain limits. A Rock can be described as an aggregate of one or more minerals. On a high level classification, one can distinguish 4 groups of rocks:

1) Common rock minerals
2) Igneous rocks
3) Sedimentary rocks
4) Metamorphic rocks

1) Common rock minerals can be described by 2 general terms:

    - **Mafic** (MA for magnesium and FIC for iron) is used for silicate minerals and rocks, which are relatively high concentration of heavier elements like magnesium and iron.
    - **Felsic** (FEL for feldspar and SIC for silica) is used for silicate minerals and rocks, which are enriched in the lighter elements, such as silica and oxygen, aluminium, and potassium.

    More precisely, mineral rocks can be classified by their chemical composition:

    - **Native elements:** Platinum, gold, silver, carbon (graphite or diamond)
    - **Oxides:** Magnetite (Fe_3O_4), maghemite (Fe_2O_3),
      Goethite or limonite ($HFeO_2$)
    - **Carbonates**: Limestone ($CaCO_3$), dolomite ($CaMg(CO_3)2$)
    - **Sulfides:** Pyrite (FeS_2)
    - **Sulfates:** Gypsum ($CaSO_4.2H_2O$)
    - **Phosphates:** Apatite ($Ca_5F(PO_4)3$)
    - **Halides :** Chlorides (NaCl, HCl), fluorides (CaF_2)
    - **Silicates** (- SiO_2, - SiO_3, - SiO_4, - Si_3O_8):
        - Olivine: Mg_2SiO_4, Fe_2SiO_4
        - Pyroxene, amphibole (common in meteorites): $CaSiO_3$, $MgSiO_3$
        - Feldspar (Al, Na, Ca, K) silicates: anorthosite ($CaAl_2SiO_8$)
        - Mica: biotite $K(Mg,Fe)3(AlSi_3O_{10})$), zircon (Zr (SiO_4))
        - Quartz: SiO_2
        - Clays (hydrous aluminium silicates): montmorillonite, nontronite

2) Igneous rocks are formed by the crystallisation of magma. Depending on the cooling rate of such a magma, 2 different rocks will be created:

    - Intrusive igneous rocks form when the magma slowly cools inside the lava crust. Intrusive rocks have high silica content. Granite (quartz, mica, K-feldspar) is a good example of an intrusive igneous rock with 65 to 73 % of SiO_2 content.
    - Extrusive igneous rocks form when the magma rapidly cools at the surface. Extrusive rocks have lower silica content. Basalt (olivine, pyroxene, Ca-feldspar) and andesite (Na-feldspar, amphibole) are good examples of extrusive rocks with lower SiO_2 content (52 - 63 %)

3) Sedimentary rocks consist of rocks and grains derived from chemical or mechanical breakdown (weathering) of pre-existing rock. They can be further classified on the basis of grain size:

- Conglomerates (> 2 mm): Boulder (> 256 mm)
  Cobble (65-256 mm)
  Pebble (4-64 mm)
  Granule (2-4 mm)

- Sand (62 μm – 2 mm): Very coarse (1-2 mm)
  Coarse (500 μm – 1mm)
  Medium (250 μm – 500 μm)
  Fine (125 μm – 250 μm)

- Shales (< 62.5 μm): Silt (3.9 μm – 62.5 μm)
  Clay[1] (200 nm – 3.9 μm)
  Colloid (< 200 nm)

4) Metamorphic rocks have been chemically altered by heat, pressure and deformation, while buried deep inside the planet's crust. These rocks show changes in mineral composition or texture.

1.3.1.2 Soil classification

Soil can be described as the collection of natural bodies on a planet's surface. Its upper limit can be defined by the gas present in the atmosphere, and its lower limit by the underlying hard rock. To give an example of soil composition, the following list describes the soil components for planet Earth:

- Mineral fraction: 45 - 50 %
- Organic matter: 0.5 – 5 %
- Water: 25 %
- Air: 25 % of soil volume
- Organisms: a small fraction of soil comprising:
  - Macro organisms (insects, earthworms)
  - Micro organisms (protozoa)
  - Bacteria, fungi and others.

As for minerals and rocks, soil can be classified by size. A distinction between unweathered and weathered materials can be made:

- Unweathered primary materials: Gravel: 2 - 4 mm
  Sand: 50 μm – 2 mm
  Silt: 2– 50 μm

[1] Same denomination as the sub-group of the silicates

- Weathered secondary materials: Clay: < 2 μm
  - Three-layer clays (Si - Al - Si lattice): montmorillonite
  - Two-layer clays (Si - Al lattice): kaolinite
  - Amorphous clays, iron and aluminium oxides

1.3.1.3 Mineral and rock identification techniques

Many minerals look very similar, and the effects of weathering often mask identifying characteristics. Several tests are combined to recognize a specific mineral. Typical characteristics like shape, magnetism, cleavage, colour, hardness and light reflection or scattering properties can be used:

Shape:
Minerals are usually formed in layers, which build up over time, generally in a shape specific to that mineral. Such shapes are called crystals and help to identify the mineral. In nature, minerals are often found in irregular shapes due to weathering and mechanical changes. Samples may retain their specific, recognizable shapes if they have not been exposed to environmental changes. Depending on the size of the minerals, optical microscopy is generally used for shape recognition.

Magnetism:
The physical properties of minerals are a direct result of their chemical and structural characteristics. Magnetic remanence is carried by ferromagnetic materials; usually iron oxides with titanium impurities. Experiments to determine the magnetic properties of a mineral can be carried out using permanent magnets to exert an attractant or repelling force.

Cleavage:
Breaking a mineral is often a good way to discover its identity. Every mineral has its proper "cleavage pattern". Some minerals, such as quartz, have no definite cleavage and will simply shatter when broken.

Colour and streak:
Colour is often one of the most useful methods for identifying a mineral, but should be used in combination with other diagnostic methods, as the exterior surfaces of many samples are discoloured due to weathering. Breaking a sample helps to reveal the true mineral colour.

Hardness:
Minerals vary substantially in hardness. Scientists are able to determine ranges of hardness by using the Moh's Scale. This simple comparative scale ranges from the softest mineral (talc) to the very hardest (diamond). If two minerals are scratched across each other, the one that leaves a streak will always be softer than the other.

Reflective, refractive and radiative properties:
Each mineral interacts differently with light. Depending on the wavelength, it will absorb and refract light differently. To be able to determine the optical properties of a mineral, it needs to be cut and polished into slabs before looking at reflection and refraction angles of an incident beam [10].
On the atomic scale, minerals can be analysed by X-ray powder diffraction. When an X-ray beam interacts with planes of atoms, part of the beam is diffracted. Depending on what atoms make up the crystal lattice and how these atoms are arranged, different diffraction patterns are produced. For this type of analysis, the mineral or rock needs to be ground to a fine powder (typical particle sizes of less than 10 microns).
In addition, each mineral emits different thermal radiations at infrared wavelength depending on its composition. The next chapter describes this phenomenon and the used detection techniques for aerosol minerals of the Martian atmosphere.

1.3.2 Thermal emission spectra of the Martian atmosphere

Mars emits infrared radiation due to the heating by the sunlight. This radiation is the sum of three contributions: the light reflected by the surface and attenuated by the atmosphere, the light backscattered by the atmosphere before reaching the surface, and the light scattered by the aerosols and reflected by the surface.
In a first approximation, the thermal emission spectrum of Mars can be described by a black body source. The Planck equation describes the radiance of a black body relative to temperature and wavelength. Since no real surface emits like a blackbody, the radiance is usually modified by a factor known as the emissivity, which varies between 0 and 1.
The CO_2 atmosphere of Mars causes a large absorption band at 15 μm in the spectra of the ideal black body radiance. Water-ice particles suspended in the atmosphere have an absorbing influence at around 12 μm. The principal features arising from the dust in the radiance curve are broad diffuse absorption bands centred near 9.2 and 20 μm. Additionally to bands in the infrared region, the dust particles suspended in the atmosphere also have strong absorption in the ultraviolet region (0.2 – 0.3 μm) [44]. Figure 1-4 shows different radiance spectrum of Mars inferred by the Mars Global Surveyor orbiter in 1997 compared to ideal black body radiance curves.
The described absorption bands related to dust are commonly observed in silicate minerals and represent the bending and stretching vibration modes respectively. The precise shape of the absorption bands and their location relative to the ideal black body radiation provides information concerning the mineral composition and particle size distribution of the dust cloud.

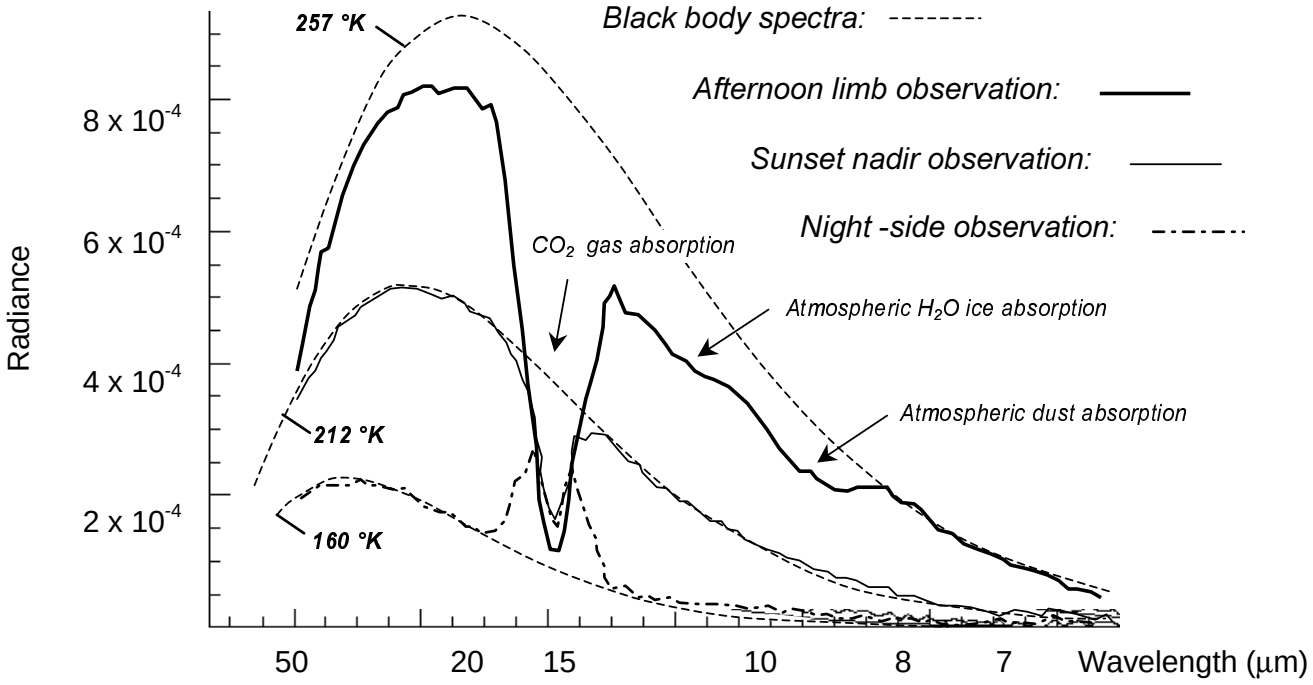

Figure 1-4

Thermal emission spectra of Mars measured by the thermal emission spectrometer (TES) onboard Mars Global Surveyor in 1997[11]. Theoretical black body radiance spectra at different temperatures are shown as a reference.

Different size distribution curves have been proposed like a lognormal or a modified gamma distribution. The size distribution can generally be expressed by its first two coefficients, which are the effective radius r_{eff} (cross section weighted mean particle radius) and variance ν_{eff} (width of the distribution). These values differ substantially from more intuitive values like the average radius r_0 and standard deviation σ_0:

$$r_0 = \frac{r_{eff}}{(1+\nu_{eff})^{5/2}}$$

$$\sigma_0^{\,2} = \ln\,(1+\nu_{eff})$$

For example, a distribution with r_{eff} = 1.85 and ν_{eff} = 0.51 will correspond to an average particle radius r_0 of 0.66 μm with a standard deviation σ_0 of 0.64, which means that 64 % of the dust particles of this particular distribution have a radius between 20 nm and 1.3 μm, or that 96% have a radius between 0 nm and 1.9 μm.

The deduction of dust composition from the observed radiance curves relies on theoretical scattering models. These models use approximations and predictions of the following parameters:

- Relative composition of the dust mixture
- Particle optical index: real and imaginary part (absorption coefficient)
- Particle size distribution: r_{eff} and ν_{eff}
- Particle shape (spheres, disks, cylinders, sharp or smooth edges)
- Particle surface roughness
- Vertical density profile of the particles in the atmosphere
- Atmospheric transfer function: absorption (optical depth), emission and diffusion

Ideally, the radiance spectrum of the Martian dust should be modelled by carrying out the spectral calculations for all possible minerals and rocks and mixtures thereof. As so many parameters are involved in the simulations, and due to the fact that the optical constants (real and imaginary refractive index) for only a small set of candidate minerals is available today, a completely unique dust particle composition cannot be claimed.
Besides absorbing the light coming from the surface, the dust particles themselves emit their own thermal radiation. It is therefore difficult to differentiate between the relative contribution of surface and atmospheric emissivity. Removing the effect of the atmospheric dust to infer the composition of the Martian soil is a formidable challenge and is has been a permanent thorn in the side of workers in this field.

1.3.3 Chronology of Mars exploration related to dust analysis

The following paragraphs give a chronological enumeration of Martian dust characteristics inferred from the first astronomic observations to the important discoveries of successful Mars missions [12].

1.3.3.1 Early Mars observations:

First astronomic observation from earth in 1809 by Flaugergues revealed “badly defined patches” without attributing them to dust. In 1873, Flammarion wrongly attributed the red colour of Mars to vegetation. In 1877, Schiaparelli made the first reliable observations of dust clouds. He wrote in his notebook: "Mars is beautiful. The Mare Erythraeum in large part appears covered by cloud”. First spectroscopic measurements originally focused on water vapour detection concluded that the Martian atmosphere is extremely arid compared to Earth (W. W. Campbell, 1909).

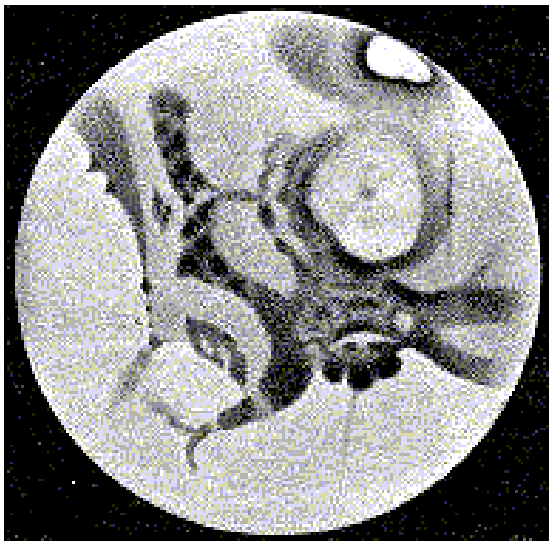

Figure 1-5
Drawing of Mars
by E. M. Antoniadi, 1909.

In 1911, Antoniadi found large parts of Mars covered for several weeks with yellowish clouds (see Figure 1-5). He correctly thought that the yellow clouds consisted of fine dust carried aloft by the winds. They were, he noted, most often seen when Mars was near perihelion. This was only to be expected, since Mars' closer position to the sun would promote a warmer atmosphere and produce stronger winds, so that the lighter sand and dust particles would be more easily picked up from the Martian deserts [13].
Observers occasionally saw huge dust storms raging over the planet, sometimes covering the entire Martian surface. Major dust storms were observed during oppositions in 1909, 1924, 1941, 1956, 1971 and 2001.
In 1947, carbon dioxide is detected as the main compound of the Martian atmosphere by infrared spectrometry (G. P. Kuiper).
The intensity changes in Martian surface markings were first explained by Dean B. McLaughlin. In a series of papers written between 1954 and 1956, McLaughlin proposed that Mars was actively volcanic. Seasonal variations in wind direction produced a redistribution in the primary ash deposits, which changed the shape and darkness of the Martian markings. Thus, according to McLaughlin, the well-documented changes were due to windblown dust rather than to the annexation of deserts by vegetation [14].
In 1963, the detection of very minute amounts of water vapour in the Martian atmosphere was announced. A photographic emulsion sensitive to infrared radiation was used to record the spectrum of Mars. The average amount of precipitable water was only about 14 micrometers, compared to 1,000 micrometers of precipitable water in even the driest desert areas on Earth. In addition, it was estimated that the partial pressure of carbon dioxide on Mars was 4.2 millibars and that the total atmospheric pressure at the surface could not be more than about 25 millibars [15]. Thus, Mars was drier and had an even thinner atmosphere than anyone had predicted before.

The reason many of the earlier investigators were so far wrong about the thickness of the Martian atmosphere was their assumption that it is usually clear and transparent. But the presence of suspended dust made the atmosphere more reflective than they had supposed.
Despite the fact that astronomers had been watching Mars for centuries, they still knew remarkably little about it. However, by the late 1950s, spaceflight technology was opening new doors for planetary astronomers. The influences of the atmospheric dust on the Martian climate [3] and geology [16] have pushed in-situ scientific investigations for the last 30 years.

1.3.3.2 Mariner 9

Between 1962 and 1973, NASA's Jet Propulsion Laboratory designed and built 10 spacecraft named Mariner to explore the solar system, visiting the planets Venus, Mars and Mercury for the first time. Mariner 4 past Mars in 1965, collecting the first close-up photographs of another planet. The pictures showed lunar-type impact craters.
The USSR had their own series of Mars missions. The Mars 2 Orbiter reached its mapping orbit successfully in 1971. The Mars 2 lander became the first human-made object to reach the surface of Mars, but it crash-landed and was unable to transmit any data. Because of a global dust storm at arrival time, the orbiter of Mars 2 could return only pictures with little surface detail. The same year, the lander of the USSR Mars 3 mission achieved the first soft landing on Mars but failed after 110 seconds of transmitting a small portion of a picture. Together with the images returned by the orbiter of Mars 2, a colour picture of the global dust storm of December 1971 was composed.
After a series of US Mars flyby missions (Mariner 3, 4, 6 and 7), Mariner 9 was the first successful US planetary orbiter of a foreign planet. Infrared images were taken by the experiment IRIS [17] during 1971 and 1972. It was designed to record the thermal emission spectrum of the Martian surface and atmosphere. It arrived at Mars during the most severe dust storm the planet experienced since the beginning of systematic observation. The measured emission spectrum of Mars, additionally to the strongly absorbing part of the CO_2 molecular band, was influenced by water-ice particles [18] and dust present in the atmosphere.
In the years following the Mariner 9 mission, several models simulating the thermal radiative properties of the dust have been built in order to reproduce the IRIS observations, and to gain information on the dust particle composition. The Toon et al. model proposed in 1977 has become a kind of standard Martian dust model [19] for the following 20 years. A particle cross-weighted mean radius r_{eff} of 2.75 μm and a variance ν_{eff} of 0.42 were used in the model. Different materials like quartz, basalt, andesite, basaltic glass, obsidian (the result of volcanic lava coming in contact with water), granite and montmorillonite were simulated. It was found that none of these materials alone could account for the spectral features of the 1971-1972 dust storm,

but concluded that a very high content of SiO_2 like it is present in montmorillonite could fit the low-infrared spectra. Montmorillonite is a member of the general mineral group of clays that contain about 65% of SiO_2 (see § 1.3.1.1)
Another model developed by Clancy et al. in 1995 [20] substantially improved the fit to the IRIS data in the far infrared. This model was also consistent with both Viking and Phobos data (see the following paragraphs). It was based on a smaller size and much broader particle size distribution than the Toon et al. model (r_{eff} = 1.8 μm ν_{eff} = 0.8). The optical properties used for the simulations were those of a mineral produced by weathering of basaltic glass called palagonite which contains only 31% of SiO_2 [21]. The same year, the thermal emission of Hawaiian palagonitic soils has been analysed on Earth. The strength of features present in the infrared spectra of Mars could not be solely provided by emissivity variations of these terrestrial palagonites [22]. Nevertheless, palagonite has since then been used as a near-infrared and visible spectral analog for bright soils on Mars.
The ultraviolet spectra during the 1971 dust storm was studied by Pang et al. to determine the particle size distribution and complex index of refraction (absorption coefficient). An effective particle mean radius of 1 μm with an effective variance of 0.2 fitted the data best. Comparison of these ultraviolet refractive indices with previously proposed materials like basalt, andesite or montmorillonite indicated that none of them had the required ultraviolet properties [44].
The information collected in the IRIS data is still not completely exploited. Even today, investigators return to this data set to confirm or complement other observations. In 1999, after correction of a 2% error due to an internal reflection of the interferogram, of the instrument [23], a more precise prediction of the dust composition could be retrieved. Using the composition of loose soil inferred by Pathfinder in 1997, the computed transmittance related to dust suggested a possible composition of 50 % silicates (albite), 10 % sulphates and 40 % mafic silicates (20 % pyroxene, 20 % olivines) [24]. Table 1-2 gives a summary of the particle properties derived from the Mariner 9 data.

1.3.3.3 Viking 1 & 2

NASA's Viking Mission to Mars in 1976 was composed of two spacecraft, each consisting of an orbiter and a lander. Both Landers transmitted images of the surface, took surface samples and analysed them for composition and signs of life, and studied atmospheric composition and meteorology. The results from the Viking experiments gave the most complete view of Mars to date [25] and remain, together with the Pathfinder data (see § 1.3.3.5), the best reference for extrapolating Martian dust properties. Figure 1-6 shows a model of the Viking lander.
Measurements of the sky brightness above the Viking Landers have been used to infer the dust single scattering properties at visible wavelength by Pollack et al. in 1979. Using the infrared dataset from the Mariner 9 orbiter experiment IRIS and the numerical model from Toon et al. [19] as a reference, parameters concerning the

mean particle radius (r_{eff} = 2.7 μm, ν_{eff} = 0.38) and shape could be retrieved [26]. The values obtained for the shape factors imply relatively smooth particles having a platelike shape, typical for clay particles.
The data collected by both Viking Landers was re-analysed 20 years later by Pollack et al. By more accurately deriving the brightness close to the sun and by using a better scattering model, it was found that the particles scatter light fairly efficiently, which implies equidimensionality and possibly very sharp corners. From the imaginary index of refraction, it was possible to retrieve the fractional composition of the dust particles. A fraction of 1.2 % of magnetite has been proposed. It was further concluded that the size distribution was not the same at the location of Viking 1 (r_{eff} = 1.85 μm, ν_{eff} = 0.5) and Viking 2 (r_{eff} = 1.52 μm, ν_{eff} = 0.5). This very slight difference could only be partially explained by different dust loading conditions at the landing sites (Viking 1 images were taken during a global dust storm of the northern hemisphere whereas Viking 2 was in an almost dust free zone). It was therefore suggested that eddy mixing[1] could be a more important mechanism for removing dust from the atmosphere than sedimentation of large particles [27].
Visible brightness images of the surface and atmosphere were taken by the Viking Orbiters as well [28]. The data was analysed in terms of dust and cloud scattering in 1991 by Clancy et al. using emission phase function (EPF) sequences, where a particular region on Mars has been observed at multiple emission angles by the Viking IRTM instrument (Infrared Thermal Mapper) [29]. Although the same single scattering model used for the Viking Lander images was applied, the suggested dust particle size was much smaller (r_{eff} = 0.4 μm) than the size suggested by previous analysis. The only work that reported such a small dust particle size was the initial analysis of the Viking Lander data in 1977 by Pollack et al. [30].
Since condensate clouds were observed in the Martian atmosphere, a number of microphysical models were developed to highlight the interactions between dust and water-ice particles. From these microphysical models, it can be assumed that the Martian dust particles play the role of cloud condensation nuclei and that the water ice is present as an outer layer on dust particles [31].
Very recently (2002), simulations based on microphysical behaviour of dust particles were carried out by Montmessin et al. Their attempt to reproduce multiple-colour images of the Martian limb provided by the Viking orbiter camera could not be obtained by using the previously predicted dust size distributions. They suggest a bimodal distribution based on sub micron-sized particles (r_{eff} = 0.2 μm) in addition to the larger (r_{eff} = 1.6 μm) now commonly used size distribution [32]. The fact that size distributions inferred from the Saharan desert have a bimodal distribution as well [33] strongly supports this hypothesis for Martian dust. Table 1-2 gives a summary of the particle properties derived from the Viking 1 & 2 data.

[1] The diffusion of atmospheric matter which is effected by whirl or circular current of air induced by pressure differences.

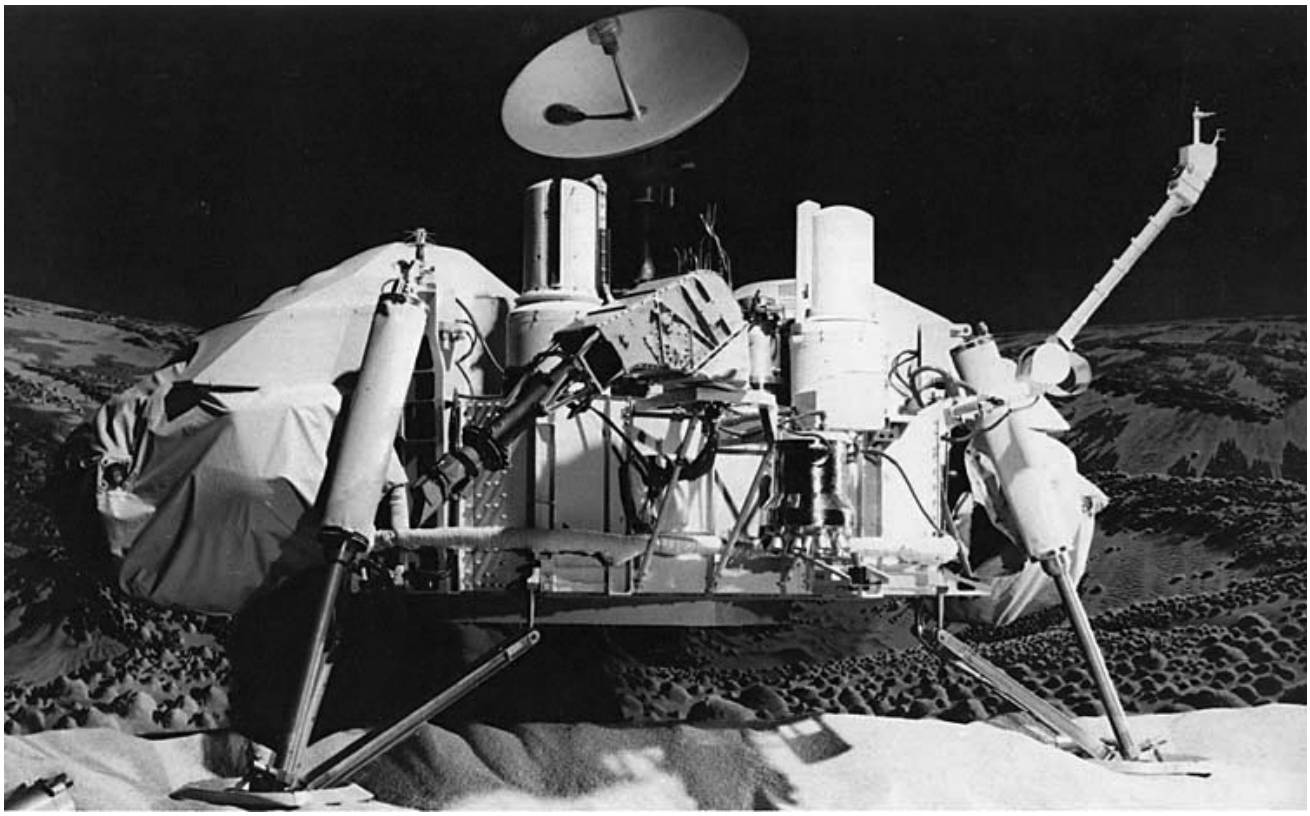

Figure 1-6
Model of the Viking 2 lander.

1.3.3.4 Phobos

The international project PHOBOS was devoted to the investigations of Mars and its moons Phobos and Deimos. Two interplanetary probes (Phobos 1 and Phobos 2) were launched in 1988. The lack of experience contributed to an error on Phobos 1, in which a command to turn the solar arrays away from the Sun was sent. Three days later contact to Phobos 1 was lost and never recovered.
The plan for Phobos 2 was to fly by Phobos at a distance of 50 meters and to deploy two Landers on the surface of the Martian moon. Phobos 2 arrived at Mars in 1989. It fired its rocket engine and inserted into Mars orbit. It took images of Phobos from a distance of 220 km and showed details 40 meters across. During the next photo session of the Martian moon, Phobos 2 turned its radio signals away from Earth and was lost as well. Fortunately, Phobos 2 had made some useful measurements of the Martian particles and field environment, which no previous probe had done over an extended period of time.
Four experiments on board Phobos 2 provided information on the characteristics of the dust particles suspended in the Martian atmosphere: Auguste (UV-visible-IR spectrometer working in solar occultation geometry) ISM (infrared spectrometer measuring the light of the Sun reflected by the planet), Thermoscan (scanning radiometer mapping the planetary thermal radiation) and KRFM (UV-visible

multiphotometer providing limb-to-limb profiles). All instruments showed that only a minor amount of dust was present in the atmosphere during the mission, which was consistent with ground-based observations made during the same period.
The results of all four experiments have been analysed together by Chassefière et al. in 1995. The vertical density profile has been measured in solar occultation geometry by the experiment Auguste and gave a consistent picture of the dust distribution in the altitude range from 15 km up to 25 km. The particle number density near the surface has been extrapolated based on the assumption that vertical transport may be treated in terms of eddy diffusion. Depending on the value for the effective variance of the particle size distribution, it varied between 1 and 6 cm^{-3}. The derived value for the dust sizes were found to be $r_{eff} = 1.7\ \mu m$ and $\nu_{eff} = 0.2$ [34].
Interesting results concerning the contribution of airborne particles to the reflectance of the planet have been published by Erard et al. in 1994. The spectrum of the ISM instrument on Phobos 2 was used to analyse the effect of the airborne particles on the spectra emitted by surface materials. Some areas showed uniform surface properties observed at widely varying elevations. As a major conclusion, the particles either form a high altitude layer or consist of mostly uplifted dust likely to be concentrated in the first few meters above the surface [35].Table 1-2 gives a summary of the particle properties derived from the Phobos data.

1.3.3.5 Pathfinder

After the highly successful Viking missions, NASA backed away from Mars for several years. During the 1980s, the only funded Mars program was the orbiter Mars Observer. It was lost in 1993 before entering Martian orbit. This loss was the low point of an unfortunate period in space exploration. The early 1990s also saw the collapse of the Space Exploration Initiative to send people to the Moon and Mars. In response to these problems, NASA introduced a new philosophy into their space science program: "faster, better, cheaper."
Launched on December 4, 1996, Pathfinder reached Mars on July 4, 1997, directly entering the planet's atmosphere and bouncing on inflated airbags as a technology demonstration of a new way to deliver a lander and rover to Mars. The lander operated nearly three times its design lifetime of 30 days, while the rover operated 12 times its design lifetime of seven days.
Pathfinder’s scientific objectives included atmospheric entry science, long-range and close-up surface imaging, with the general objective being to characterize the Martian environment for further exploration. The bulk of the Lander's task was to support the rover by imaging its operations with the imager for Pathfinder camera (IMP) and relaying data from the rover to Earth. The rover Sojourner carried two instruments: a camera to take pictures, and an alpha proton X-ray spectrometer (APXS) to measure the elemental compositions of rocks. The technique of APXS is based on three kinds of interactions of alpha particles from a radioactive source with matter. Analysis can

be performed on samples of 50 mm diameter with a depth of some tens of micrometers. Figure 1-7 shows Sojourner during an APXS measurement.
The IMP imager returned sequences of images of the Martian sky which could be analysed in terms of aerosol size distribution and optical refraction index by Tomasko et al. in the same way Pollack et al. had done 20 years earlier with the Viking I lander images [26]. The inferred mean particle radius of 1.6 μm was in good agreement with the revised analysis of Viking data in 1995 by Pollack et al. [27]. An abundance of about 1 to 10 particles per cubic centimetre was estimated. A comparison with existing laboratory measurements of mineral powders suggested that neither particles with sharp edges nor complex particles including concave surfaces would fit the spectral observations [36].

Figure 1-7
Sojourner Rover taking an Alpha Proton X-ray Spectrometer measurement of a rock named "Yogi". Dark tracks left by the wheels show the navigation sequence to get as close as possible to the rock.

Some experiments on board Pathfinder focused on the grain size of the fine soil that covered most of the landing site. Images of wheel tracks of Sojourner left low to nonexistent rims and had a reflective surface. Such tracks were produced on preliminary experiments on Earth in loose materials with grain sizes less than 40 μm

[37]. Some rocks imaged by the camera onboard Sojourner appeared to be fluted and grooved by saltating sand-sized (62 μm - 2 mm) particles in the wind [16].
Different soil colours were detected by the Sojourner imager. As the composition of these soils detected by the APXS instrument showed all similar composition, the differences in colour might be due to slight differences in iron mineralogy or differences in soil particle size and shape [38].
Five rocks and six soil sites were analysed by Rieder et al. in terms of composition by the APXS spectrometer. The composition of a relatively dust free rock called Barnacle Bill could correspond to an andesite. However, scientists could not be certain that the inferred rocks were of igneous type (formed by crystallisation of a magma), since high-resolution images of the rock surface showed sedimentary or metamorphic features.
The soil composition showed much larger fractions of magnesium and iron than the analysed rocks. Thus, even if weathering and the addition of elements provided by volcanic gasses are taken into account, the soils could not have formed from the rocks measured at the landing site [39].
Pathfinder was also equipped with an experiment to assess the magnetic phase in the Martian airborne dust. An array of five magnets with decreasing strength was mounted on the Lander and imaged by the IMP camera. The only particles to which these magnets would be exposed are the aerosols suspended in the atmosphere. From the observations of these magnets, it was concluded that most of the particles were moderately magnetic. Maghemite (γ - Fe_2O_3) was supposed to be the mineral causing magnetism in the dust and that the particles might therefore be composite clay particles [40].
The rover Sojourner carried a material adherence experiment (MAE) to quantify the effect of dust deposition from the Martian atmosphere on the performance of solar arrays [41]. The measured obscuration rate during the first 20 Martian days (sols) was 0.33 % per day. A theoretical calculation taking into account the particle size, the single particle obscuration and the dust deposition rate due to gravitational settling predicted an obscuration rate of 0.22 % [42]. This very close prediction was based on the dust properties inferred by Pollack et al in 1995 [27]. Table 1-2 gives a summary of the particle properties derived from the Pathfinder data.

1.3.3.6 Mars Global Surveyor

Global Surveyor (MGS) was a replacement mission for the failed orbiter Mars Observer, which was supposed to be sent to Mars in 1996. MGS was the second spacecraft to follow the “faster, better, cheaper” philosophy after Pathfinder. However, MGS did not perform flawlessly. One of the solar arrays did not unfold into the correct location during cruise. Like Mars Observer, it was intended to use drag against the Martian atmosphere to lower the orbit of MGS after arrival. Due to this faulty array, It took MGS six additional month to reach its 2-hour mapping orbit in 1999.

Mission	Type	Size [μm] r_{eff} (ν_{eff})	Shape	Composition	Source
Mariner 9	IR	1 - 4	Disks, flakes	7% Quartz 93% Anorthosite	Aronsen et al. 1975 [43]
Mariner 9	UV	1.0 (0.2)	Spherical	-	Pang et al. 1976 [44]
Viking Lander	IR	0.4	Nonspherical	10% magnetite	Pollack et al. 1977 [30]
Mariner 9	IR	2.75 (0.42)	Spherical	Montmorillonite	Toon et al. 1977 [19]
Mariner 9	UV	0.2 (0.9)	Nonspherical	Andesite, basalt, montmorillonite	Chylek et al. 1978 [45]
Viking Lander	Visible	2.7 (0.38)	Platelike	-	Pollack et al. 1979 [26]
Viking orbiter	Visible	< 0.4	Nonspherical	-	Clancy et al. 1991 [29]
Phobos 2	IR	1.24 (0.25)	Nonspherical	-	Drossart et al. 1991
Phobos 2	UV - Visible	0.4 (0.5)	Spherical	Goethite Limonite	Moroz et al. 1991 [46]
Phobos 2	IR	25 km: 1.0 (0.8) 12 km: 1.8 (0.4)	Spherical	Basalt, Limonite Magnetite	Korablev et al. 1993 [47]
Mariner 9	IR	0.5 (0.15)	Spherical	Palagonite	Santee et al. 1993 [48]
Phobos 2	IR	1.7 (0.2)	Nonspherical	-	Chassefière et al. 1995 [34]
Mariner 9 Viking, Phobos	UV IR	1.8 (0.8)	Spherical	Palagonite	Clancy et al. 1995 [20]
Viking 1 Lander Viking 2 Lander	Visible	1.52 (0.5) 1.85 (0.5)	Sharp corners	1.2 % magnetite	Pollack et al. 1995 [27]
Pathfinder	Visible	1.0 (0.3)		-	Smith et al. 1997 [49]
Pathfinder	Visible	1.6 (0.2)	Nonspherical	-	Tomasko et al. 1999 [36]
Pathfinder	Visible	1.71 (0.25)	Plate-like	-	Markiewicz et al. 1999 [50]
Mariner 9 Pathfinder	IR	-	-	50% Andesite 10 % Sulfite 40 % mafic Si	Grassi et al. 1999 [24]
Global Surveyor	IR	1.5 – 1.8	Cylindrical	Palagonite-like	Pitman et al. 2000 [54]
Viking orbiter	Visible	1.6 (0.5) 0.2 (0.03)	Spherical Bimodal	-	Montmessin et al 2002 [32]

Table 1-2

Chronological enumeration of dust size and composition inferred by spacecraft observations.

As for Mariner 9 in 1971, an infrared spectrometer was on board MGS. It had a much improved spectral resolution and sensitivity. The thermal emission spectrometer (TES) first flew aboard the Mars Observer spacecraft [51]. Following the loss of that spacecraft, TES was rebuilt and launched aboard MGS, along with five other Mars Observer instruments. Up to this date, it has mapped the temperature and amount of dust in the Martian atmosphere for over one Mars year (approximately two Earth years).
The TES instrument has identified water-ice clouds using the infrared spectral signature of ice [52]. A spherical approximation of the ice particle shape provided a mean radius of 2 μm, which confirmed previous data from IRIS on Mariner 9 [18].
Because of the heavy influence of dust and water ice aerosols on the infrared spectra emitted by the surface of Mars, few studies have attempted to interpret the spectra emitted by the surface in the thermal infrared. Following the results of the TES instrument, algorithms have been developed to separate spectral features coming from atmospheric on one hand, and surface components on the other. It was found that both find very similar spectral shapes, indicating that the composition of the dust in the atmosphere might be close to that of soil on Mars [53].
The discovery of ice clouds and their spectral features has initiated more precise research on the shape of the airborne dust and ice particles. Based on emission phase function (EPF) sequences of the TES instrument, where a region is observed at multiple emission angles, a scattering model using shapes like cylinders and disks in addition to spheroids has been developed. While the ice particle EPF sequence appears to be reproducible only by spheroids, the dust particle EPF sequence can be produced by cylindrical shapes with distribution of axial ratios [54]. The dust phase function could be best fitted by randomly oriented cylinders with a diameter-to-length ration of either 2.3 (disk shape) or 0.6 (coke can shape) [55]. The dust particle radii of 1.5 - 1.8 μm were consistent with the recent re-analysis of Mariner 9, Viking and Phobos infrared data [20]. Table 1-2 gives a summary of the particle properties derived from the MGS data.

1.3.3.7 Mars odyssey

NASA's robotic exploration of Mars suffered two major setbacks in the late 90's. Mars Climate Orbiter (MCO) and Mars Polar Lander (MPL), 2 missions scheduled to arrive at Mars in September and December of 1999, were both lost (see § 1.4.4). The back-to-back failures motivated a complete redesign of the U.S. long-term programme for Mars exploration by robot spacecraft. NASA cancelled the 2001 lander, but launched the 2001 orbiter named Mars Odyssey.
Odyssey's aerobraking ended in January 2002, and it began its science-mapping mission at the same time this thesis is written. The three primary instruments carried by Odyssey are:

- THEMIS (Thermal Emission Imaging System), for determining the distribution of minerals, particularly those that can only form in the presence of water
- GRS (Gamma Ray Spectrometer), for determining the presence of 20 chemical elements on the surface of Mars, including hydrogen in the shallow subsurface (which acts as a proxy for determining the amount and distribution of possible water ice on the planet)
- MARIE (Mars Radiation Environment Experiment), for studying the Martian radiation environment

The primary science mission will continue through August 2004. The spacecraft will also serve as a communications relay for U.S. and international spacecrafts scheduled to arrive at Mars in 2003 and 2004.

1.3.4 Human exploration of Mars

The world's attention is focused on the exploration of the solar system more strongly now than ever before. As world history illustrates, humans are compelled to discover new frontiers. Our exploration of the space frontier has already begun. Robotic missions and new technology are the first steps toward expanding human presence in the solar system. Human missions to Mars and beyond may become a reality in the 21st century [56]. There are many reasons why Mars is a human exploration target [57]:

- **Human Evolution** - Mars is the most accessible planetary body beyond the Earth-Moon system where sustained human presence is believed to be possible. However, it is not an objective of the Reference Mission [60] to settle Mars but to establish the feasibility of, and the technological basis for, human settlement of that planet.
- **Comparative Planetology** - The scientific objectives of Mars exploration is to understand the planet and its history in order to better understand Earth.
- **International Cooperation** - The political environment at the end of the Cold War may be conducive to a concerted international effort that is appropriate, and may be required, for a sustained program.
- **Technology Advancement** - The human exploration of Mars currently lies at the ragged edge of achievability. Some of the technology required to achieve this mission is either available or on the horizon. Other technologies will be pulled into being by the needs of this mission. The new technologies or the new uses of existing technologies will not only benefit humans exploring Mars but will also enhance the lives of people on Earth.
- **Investment** - in comparison with other classes of societal expenditures, the cost of a Mars program is modest.

Based on the Mars reference mission [60], a manned mission to Mars would begin with the assembly of different Mars spacecraft in a low-Earth orbit. Once assembled, these would deliver an Earth-return vehicle into orbit around Mars, and a launch and cargo vehicle to the surface. Twenty-six months later an astronaut crew would leave Earth orbit and begin its journey to Mars. The trip would take four to six months depending on the propulsion system used and the alignment of Earth and Mars. As the crew reached Mars, its spacecraft would enter Mars' atmosphere and land near the waiting cargo and ascent vehicle. The crew would spend about 18 months on the Red Planet, setting up a base and conducting a wide assortment of scientific tests. The search for life, past or present, would be a major objective. At the end of its stay, the crew would pack up collected samples and leave Mars using the propellant produced on the surface to reach orbit. The launch vehicle, delivered before the crew ever left the Earth, would lift the human crew off the Martian surface to the orbiting Earth-return vehicle. After a four- to six-month trip back to Earth, the crew would return almost three years after beginning their adventure.

A thorough understanding of the Martian environment is critical to the safe operation of equipment and to human health. Simulated Martian scientific field studies are carried out since the beginning of 2000 by the NASA Haughton Mars Project (HMP). This international field research program is centered on the scientific study of the Haughton impact crater in the Canadian high arctic, viewed as a Mars analog (see Figure 1-8). This project is used to support studies in exploration research, to investigate the technologies, strategies, human factors and hardware designs relevant to the future exploration of Mars by robots and humans [58].

Although the dream of human Mars exploration is very real in most people's mind, more political issues will slow down the development of a human Mars exploration plans in the future. The budget priorities set forth for the year 2002 by President Bush's administration forced NASA to scale down its budget. As a consequence, it stopped work on the Mars Advanced Exploration Technology project designed to develop a possible future human mission to Mars. NASA also announced the phasing out of Trans-Hab, the only part of the International Space Station that was being developed for future human exploration beyond Earth orbit.

On a more positive side, NASA proposed budget increases for the robotic exploration of Mars. This will assure a continued systematic exploration of the Red Planet in coming years by remote spacecrafts.

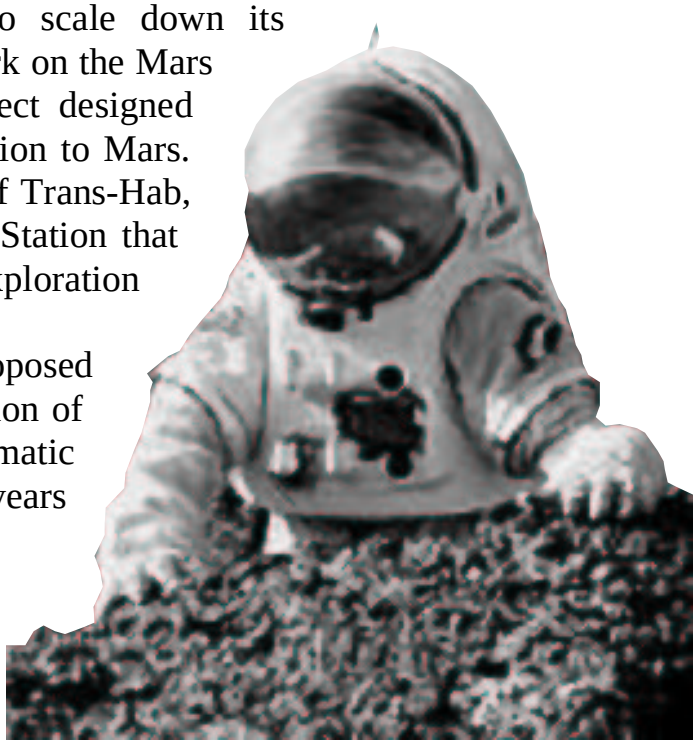

Figure 1-8
Astronaut of the Haughton Mars Project.

1.4 The scientific payload MECA

Scientific data from several Martian experiments indicate a vigorous recirculation of dust between the Martian surface and atmosphere (see §1.3.3). Although properties of the dust have been inferred from remote sensing and evaluated by surface experiments, there has been no imaging of individual dust and soil particles to determine their size distribution and shape. Such information is essential in understanding the contribution of the particles to the Martian climate and its geological past (see § 1.3).
As mentioned in § 1.3.4, a manned mission to Mars requires a thorough understanding of the Martian environment. The exact properties of the Martian dust are required for safe operation of equipment and to protect human health. MECA (Mars environmental compatibility assessment) has been designed to assess harmful effects of the dust suspended in the atmosphere and the soil covering the ground [59]. MECA was developed at the Jet Propulsion Laboratory through NASA's Human Exploration and Development of Space (HEDS) Enterprise.
The following section gives an overview on the MECA payload and it’s scientific goals. It also describes under which circumstances the first opportunity for MECA to fly to Mars was cancelled.

1.4.1 Hazards for human explorers

According to elaborated exploration plans [60], a human crew will travel to and from Mars on relatively fast transits (4-6 months) and will spend long periods of time (600 days nominal) on the surface. As the objective of human exploration will be to spent time on the surface of Mars, extensive extravehicular activity (EVA) will be required. Therefore, the presence of dust particles on the surface of Mars will present several risks [61].
For a particle to be hazardous to an astronaut, it must not only be intrinsically dangerous, but it must find its way into the astronaut's habitat, space suit, or vehicle. Adhesion is a way that particles can enter protected places: dirt can cling to the astronaut's spacesuit and be brought into the habitat where it can be inhaled or ingested, and where the toxic elements may become corrosive or poisonous. The following sections describe the different hazards that face astronauts and equipment on Mars due to adhesion.

Abrasion
Abrasion occurs when the Martian dust is rubbed against man-made surfaces. This can occur due to fast moving particles in the wind (sandblasting) or astronauts attempting to clean solar panels, windows, or lenses. Depending on the hardness of the dust particles, they will have different effects on equipment: hard particles (like quartz) will scratch the surfaces, softer particles (like clay) may polish the surfaces

and cold-weld moving parts together. Evidence for dust abrasion was found during the Apollo missions on the moon where fine moon dust particles clung to spacesuits and tools electrostatically, resisting brushing off and wearing the spacesuit material. [62]

Corrosion
When Martian chemicals are transported into habitats, they may be activated by the addition of water. These salts, acids, or alkaline materials can attack critical life-support components. Specific corrosion hazards for Mars explorers include corrosion of space suit materials and airlock seals.

Toxicity
Toxicity and pathogenicity refer to substances that cause illnesses and diseases, respectively. Breathable quartz particles are among the most dangerous particles faced by industry on Earth. Pathfinder's apparent identification of quartz on Mars focuses the search on this material and other respirable particles.
Quartz, due to its hardness and chemical composition, will probably be the most hazardous substance, for both man and machinery found on the Martian surface. It is well known from the mining and construction industry that quartz particles in the respirable size range causes silicosis and related diseases. The following section gives a more detailed description of silicosis.

Obstruction
Dust in the Martian atmosphere, lofted by a distant dust storm, presents no obvious hazard. It may, however, block sunlight for days or weeks and affect solar panel performance. A layer of dust will accumulate on the surroundings and on all the structures and equipment, leading to potential mechanical hazards.

Electronic Failure
Electrical shorting of power lines or instruments due to electrical pathways made by dust is a common phenomenon in terrestrial arid or dusty regions. On Mars, arcing and shorting occur at far lower voltages than either on Earth or in open space due to the presence of a rarefied atmosphere [63]. Conducting particles that accumulate on electrically active elements such as connectors and terminals could induce shorting of electronic circuits. Even with precautions such as shielding, defects in coatings could result in shorting paths through conducting particle films.

1.4.1.1 Silicosis

Silicosis is a disabling, non-reversible and sometimes fatal lung disease caused by overexposure to respirable crystalline silica. Silica is the second most common mineral in the earth's crust and is a major component of sand, rock, and minerals. Overexposure to dust that contains microscopic particles of crystalline silica can

cause scar tissue to form in the lungs, which reduces the lungs' ability to extract oxygen from the air.
Working in any dusty environment where crystalline silica is present potentially can increase a person's chances of getting silicosis. Today, more than 1 million U.S. workers are exposed to crystalline silica. Each year, more than 250 American workers die with silicosis. This number was much higher in the beginning of the century before safety procedures and exposure limits were set by health organizations.
Today, the most severe worker exposures to crystalline silica results from sandblasting. The now forbidden silica sand used in sandblasting typically fractured into fine particles and became airborne. In the construction industry, sandblasting is used to remove paint and rust from stone buildings, metal bridges, tanks and other surfaces. Other construction activities that may produce silica dust include jackhammer operation, rock drilling, concrete mixing and brick cutting.
There are three types of silicosis, depending upon the airborne concentration of crystalline silica to which a worker has been exposed:

- Chronic silicosis: usually occurs after 10 or more years of overexposure.
- Accelerated silicosis: results from higher exposures and develops over 5-10 years.
- Acute silicosis: occurs where exposures are the highest and can cause symptoms to develop within a few weeks or up to 5 years.

The development of silicosis depends on a number of factors including [64,65]:

- The particle size:
  Airborne dust particles are small enough to become trapped in the lungs, and are not exhaled, coughed or sneezed out, as are larger particles, like pollen grains.

  - Airborne dust particles with a size larger than 10 μm are usually caught in the nose and upper airway and discharged as sputum or swallowed.
  - Airborne particles with sizes between 4 and 10 μm usually settle out in the upper lungs and bronchial area, possibly causing asthma like symptoms.
  - Airborne particles smaller than 4 μm can be carried deep into the lower lungs where oxygen transfer takes place and cause silicosis.

- Nature of inhaled dust:
  Silicosis can only occur when free silica is involved. Free silica means that only SiO_2 is present in the crystal, opposed to combined silica, where other molecules or atoms are bound to the SiO_2 molecules.

Quartz is the best example of a natural mineral that is almost pure silicon dioxide. Other forms of free silica are tridymite and cristobalite. Tridymite forms from quartz above 870 °C into orthorhombic crystals while cristobalite forms above 1470 °C into cubic crystals. Other ceramic minerals like feldspar and clay contain free silica as well. However, they also usually contain combined silica. Other silica-containing rocks and minerals are limestone, mica, talc, granite, palagonite, montmorillonite and sandstone.

- Amount of free silica in the inhaled dust:
  As mentioned above, it is only free silica that causes silicosis. The OSHA (Occupational Safety and Heath Administration) established an occupational exposure limit to crystalline silica for a 40-hour working week [66]. This limit is set at 0.05 mg/m^3, which corresponds to a concentration of 4.6 particles per cubic centimeter for particles with a radius of 1 μm. The OSHA permissible exposure limit (PEL) is determined by the following equation:

$$\boxed{PEL = \frac{10 mg/m^3}{\%SiO_2 + 2}}$$

  PEL is a regulatory limit on the amount or concentration of a substance in the air. Therefore, a mineral containing 60 % of free silica will have a permissible exposure limit of 0.16 mg/m^3 or a concentration of about 15 particles per cubic centimeter for particles with a radius of 1 μm.

1.4.2 MECA experiments

The MECA payload will, by direct observation and experimentation, explore two central aspects of Martian dust and soil: the character of the material itself, and the propensity of the material to remain in harmful contact with materials and/or be transported to places where it can be activated with harmful consequences. The following scientific experiments have been implemented to MECA to investigate the above-mentioned threats:

- The Wet Chemistry Lab [67,68] will evaluate samples of Martian soil in water to determine the total dissolved solids, redox potential, and pH, and to detect potentially dangerous heavy metal ions, emitted hazardous gases, and the soil's corrosive potential. All wet chemistry will be done in four single-use reaction chambers, configured to accept separate soil samples. A sampling "drawer" will receive a sample from the robot arm implemented on the Lander. Excess material is swept away by the action of the drawer closure. After the drawer is re-sealed,

the soil and water will be mixed together and analysed. Figure 1-9 shows mock-ups of the chemical cells of MECA.

- The material patch plates experiment consists of materials commonly used for space suits and equipment that will be exposed to the Martian dust and soil. They are placed in view of the lander robotic arm camera to infer material wear and adhesion properties. Figure 1-9 shows the location of the different patch plates after deployment.

- The electrometer experiment will measure tribo-electric charging and atmospheric ionisation due to radiation. It is placed on the scoop of the robot arm to look at charging effects when digging the soil. These phenomena are a direct result of adhesion, which will be studied in detail using the MECA microscopy station.

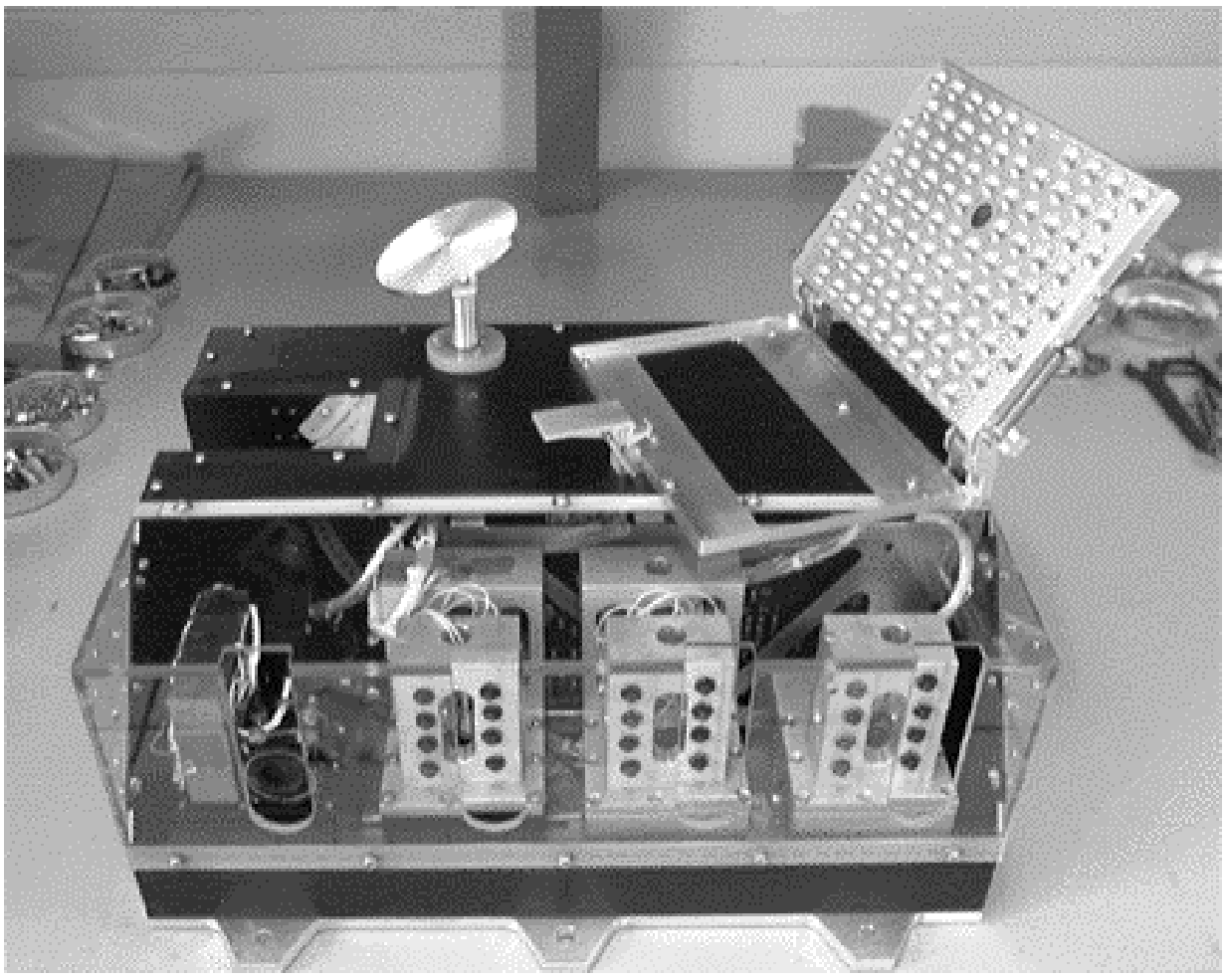

Figure 1-9
Picture of the assembled MECA payload MECA's microscopy station with mock-ups of the chemical cells in font and deployed patch plates on top. The microscopy station is enclosed in the box.

1.4.3 MECA's microscopy station

MECA contains a microscopy station to produce images of dust and soil particles. Analyses of scientific experiments indicate that the mean particle radius of Martian atmospheric dust is less than 2 micrometers (see 1.3.3). Therefore, MECA's microscopy station, in addition to an optical microscope capable of taking colour and ultraviolet fluorescent images, includes the presented atomic force microscope (AFM) to image far below optical resolution. A detailed description of the working principle of an AFM is given in § 1.5. The microscopy experiment is enclosed in the box showed in Figure 1-9 and placed on the lander platform.

Sample delivery
Delivery of the dust samples is achieved by an external robotic arm, which is part of the lander platform equipment. This robotic arm is equipped with a scoop to be able to take surface and subsurface samples. A sample-handling wheel with 69 substrates is enclosed in the MECA box. A small slit located on the top of the box will reveal only a segment of the wheel, exposing a set of 7 different substrates at once. Since the composition of the dust is not precisely known, these substrates have different hardness and adhesion properties (magnetic, conductive or non-conductive).
The dust delivered on the exposed substrates will be brought in front of the microscopes by performing a rotation and translation of the wheel. The substrates will be investigated by optical microscopy before being brought into contact with the AFM. This will allow a selection of a relatively clean area for AFM measurements. The optical resolution of the microscope is of 8 micrometers per pixel. Since the AFM X, Y range is of about 50 micrometers, the overlap between optical and AFM pictures will be of 6 pixels. By rotating the sample wheel, it is possible to position the sample in the X direction. The positioning accuracy on the rotational axis of the sample wheel is of about 30 micrometers. On the translation axis, each step corresponds to a displacement of 0.5 μm. Figure 1-10 shows a photograph of the microscopy stage.

Abrasion tool
The microscopy station includes a tool for performing simple mineralogical scratch and streak tests on the particles from the Martian soil [69]. The abrasion tool will be applied to particles that adhere themselves to highly polished substrates of various hardness. A leaf spring will be applied with a paraffin actuator to press the particles against the substrates. The pressure per particle will depend on the grain size and the number of grains adhering to the surface. The sample wheel will be rotated after the particles are placed in compression to produce the scratches or pits.
A primary goal of the abrasion tool is to identify quartz (Moh's hardness = 7) using substrates of varying hardness. The scratches will be identified using the optical microscope and profiled with the atomic force microscope.

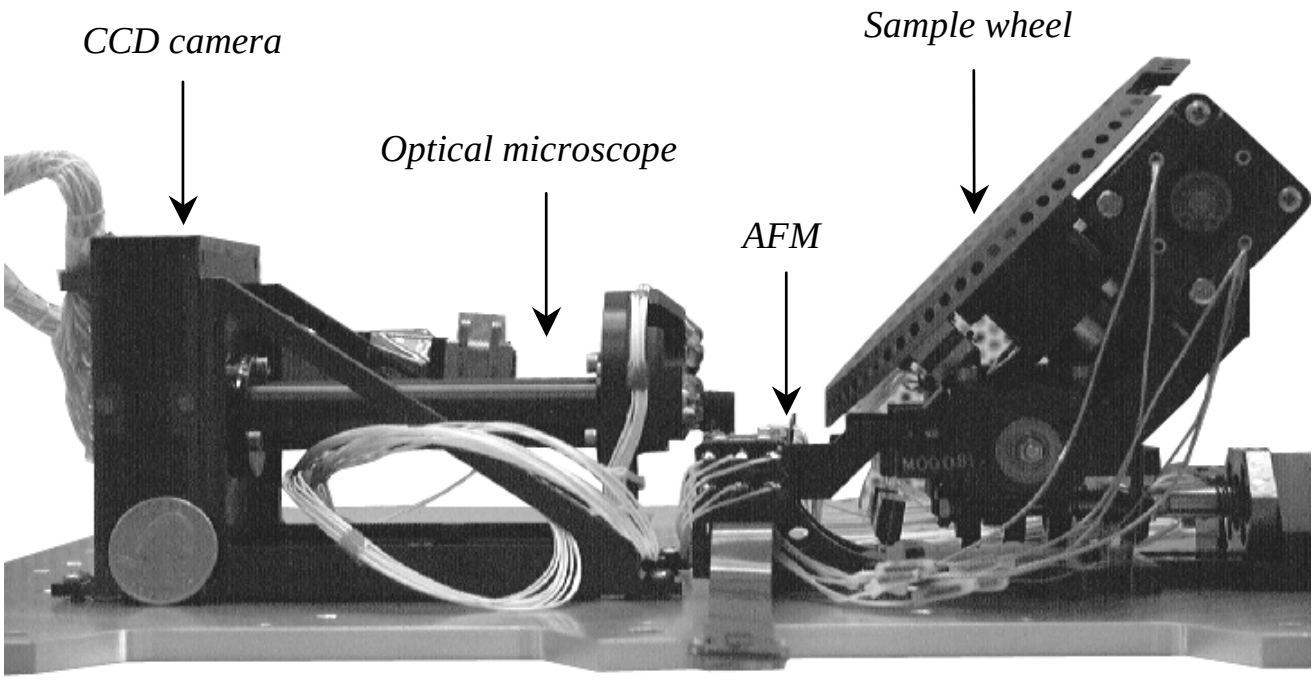

Figure 1-10
Photograph of MECA's microscopy station.

1.4.4 Cancellation causes of the Mars surveyor 2001 lander

The opportunity to go to Mars comes around every 26 months, when the alignment of Earth and Mars in their orbits around the sun allows spacecraft to travel between the two planets with the least amount of energy (opposition).
MECA was selected to fly with NASA's Mars surveyor Lander, scheduled to be launched in April 2001. The following paragraphs describe the design phase of this Lander and the circumstances under which it was cancelled [70].
The Mars Surveyor Lander was originally intended to be the first mission to collect samples of Martian rocks and soil for later return to Earth. The mission had to be sharply scaled down in early 1998 because of budgetary problems. It then consisted of a lander similar to the 1998 Mars Polar Lander (MPL), but carrying several new experiments:

- A short-range mini-rover ("Marie Curie") almost identical to Mars Pathfinder's "Sojourner" (see § 1.3.3.5)
- A set of experiments designed to gauge possible physical dangers that the Martian surface may present to human explorers (MECA)
- In-situ resource tests to assess the feasibility of manufacturing rocket propellant out of Mars' atmosphere.

In September 1999, Mars climate Orbiter (MCO) was lost during Mars orbit insertion. The root cause for the loss of MCO was the use of English units instead of metric units in a software patch that calculated the insertion trajectory. The loss of MCO had a first major impact on the 2001 Lander design. Since MCO was the first backup communication link to earth for the 2001 Lander, it was decided to add a direct link to earth antenna on the lander.
At this same time, the Mars Polar Lander (MPL) was 2 month away from its landing on Mars. During a review of MPL's entry descent and landing phase (EDL), it was discovered that the descent thrusters needed much more heating power than originally planned for. This induced another modification on the solar panels of the 2001 lander.
Then, on December 3 1999, MPL was lost during EDL. The probable cause of the loss has been traced to premature shutdown of the descent engines, resulting from a vulnerability of the software to transient signals. This software error was immediately corrected and incorporated in the 2001 lander software. The loss of MPL without being able to trace its exact crash scenario led the design of a black box that would be incorporated to the 2001 lander. This led to the cancellation of several scientific payloads to accommodate some space for it.
In March 2000, the failure review board of MPL came out with a list of recommendations for the 2001 Lander. Following these recommendations, a "return to flight" board held for the 2001 Lander. As no clear statement for the launch of the 2001 lander was given by this board, and probably due to the overall tight situation, NASA cancelled the 2001 lander.
In the next months, three options for the following 2003 mission emerged. A Pathfinder-like rover mission, an orbiter mission, and an upgraded '01 lander. A short time later, the latter option was dismissed for being "too high risk". The scientific payloads selected to fly with the 2001 Lander mission have been put on a waiting list, together with the experiments that were part of MPL and could never produce scientific data.
On the positive side, the 2001 orbiter mission called Odyssey remained on schedule, and NASA has announced an exciting dual-rover mission for the 2003 launch opportunity.

1.4.5 New flight opportunities for MECA

MECA's current architecture necessitates a stable platform equipped with a robotic arm and a camera to perform data analysis with all experiments.
Based on the missions designed by NASA, the earliest flight opportunity for MECA (or a MECA follow-on) will be in 2007 where NASA proposes to develop and to launch a long-range, long-duration mobile science laboratory that will be a major leap in surface measurements. The MECA payload would then be a precious tool to gain information on size distribution, hardness and shape of the Martian dust and soil.

1.5 Atomic Force Microscopy

The Atomic Force Microscope (AFM) has revealed itself as a reliable tool for characterizing surface topography with nanometer resolution. It can be classified in the family of scanning probe microscopy (SPM) methods, where a miniaturized probe is scanned across the surface of a sample in a raster like manner (see Figure 1-11).
At each point on the sample (pixel), a certain physical signal is measured, and finally reconstructed in a computer point by point. Physical signals that have been used to sense surfaces include electron tunnelling current, inter-atomic forces, photons, capacitive coupling, electrostatic force, magnetic force, and frictional force.
In two prominent cases (scanning tunnelling microscope (STM) and atomic force microscopy), the sensing signals depend so strongly on the probe-substrate interaction that changes in substrate height of as little as 0.01 nm can be detected. It was the ability of the STM to image individual atoms on surfaces that won the inventors of the STM the Nobel Prize for Physics in 1986 [71].
The following section describes the basic working principle of an AFM. It also gives an insight on common terrestrial application of AFM and describes different design options for building such an instrument.

1.5.1 AFM working principle

The AFM uses a sharp tip at the end of a soft cantilever to probe the topography of the surface [72]. In most cases, the scanning principle relies on piezo-electric deformation of a ceramic tube on which high voltages are applied. Generally, the tip is scanned forward and backward over the same line before stepping to the next. Figure 1-11 shows an alternative way of scanning where each line is either recorded in forward or backward motion.
When using a feedback loop to keep a constant interaction between the tip and the sample, an error signal, additionally to the topography signal, will be recorded. This error signal translates the ability of the closed loop system to keep a constant force on the sample. The feedback loop is in most cases regulated by a PI controller where the proportional and integral factors of the system can be adjusted [73].
Two different techniques can be distinguished to sense the topography: static and dynamic. Both rely on the modification of the cantilever position due to influence of the surface proximity:

Static mode
In static mode, the tip is in direct contact with the surface. This happens only when the distance between the surfaces is very small. Just outside the range at which repulsive interactions become dominant, the force between the tip and the surface is attractive, due to van der Waals interactions. Due to these interactions, the cantilever is bended in one direction or the other when scanned over the surface. In constant

force mode, this bending is kept at a constant value while scanning over the surface. This is done by the scanner, which in addition to performing the X and Y motion, controls and measures the Z deflection by a closed loop system. Figure 1-11 shows the working principle for static mode detection.

Dynamic mode

Alternately, to static mode, the cantilever is excited at its mechanical resonance. When approaching the sample surface, the resonance frequency as well as the amplitude of the cantilever is lowered due to the force gradient present above the sample surface. One of these two values (frequency, amplitude or phase) is kept constant by the scanner by varying the height of the tip over the sample.

Dynamic mode has the advantage that lateral forces between the tip and the sample are minimized. In constant frequency mode, the phase shift between the driving signal and the detected signal is detected and kept constant by a phase locked loop (PLL) [74].

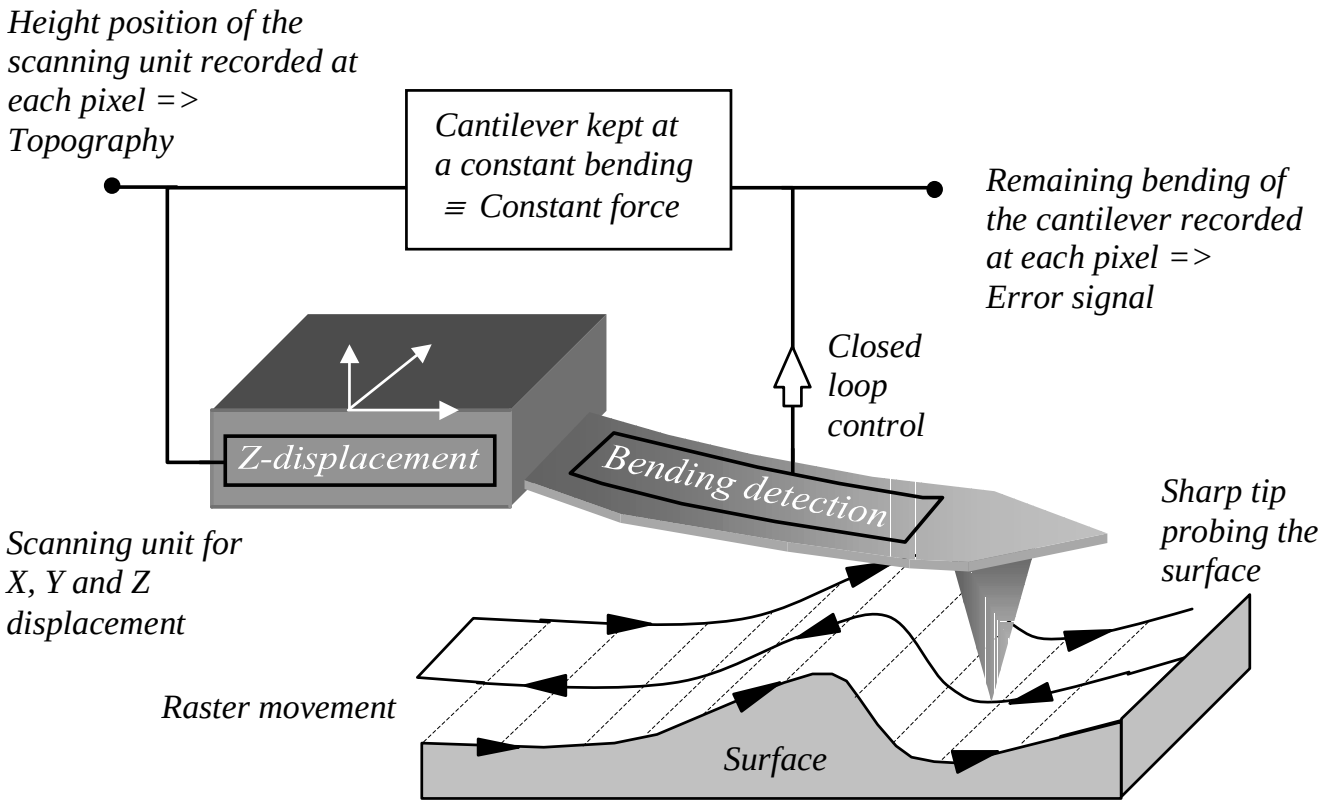

Figure 1-11
AFM working principle described for static mode with closed loop for constant force imaging.

1.5.2 Fields of application

The main application of AFM is imaging of structures on a sub-micrometer to nanometer scale, where optical microscopy is limited by light diffraction.
AFM is finding a variety of applications in semiconductor science and industry. For example, it is used to examine wafer-cleaning methods, profiles of etched surfaces or deposited films and for defect detection or failure analysis.
One of the advantages of AFM compared to STM is that it can image non-conducting surfaces and be used at atmospheric pressure and in water. Thus it was immediately applied to biological systems, such as analysing and manipulating DNA and RNA, chromosomes, cellular membranes, proteins and other biomaterials.
Another technological application is the mapping of magnetic fields by AFM. For this function, the AFM, also called the magnetic force microscope (MFM), uses a magnetic tip to sense the magnetic tip-sample force or its gradient. This technique can be used to create data storage devices.
Similarly, electrical fields can be mapped with the AFM. To this purpose, the tip is generally charged, and the tip senses an electrical force. Thus the AFM can be operated as a potentiometer that maps the voltage gradient on a surface on a scale of a few tens of nanometers.

1.5.3 AFM design concepts

Several methods can be used to detect the cantilever deflection. The detection technique has a major impact on the overall instrument architecture and on the possibility to operate the instrument autonomously.

Optical sensing concept:
In most cases, atomic force microscopes have a force detection system based on optical laser deflection, where the beam is trained on the back surface of the cantilever and the reflected beam is sent to a 4-quadrant photodiode. Due to the macroscopic length of the reflected light path, any deflection of the cantilever causes a magnified lateral displacement of the reflected laser spot on the photodiode.
For this technique, as this detection system is quite space taking and heavy, it is preferable to produce the scan movement on the sample side rather than moving the cantilever - detection system over the sample. Thus, the sample is mounted on the XYZ stage, while tip, cantilever and detection system stay in place. As this design necessitates alignment of the laser on the cantilever as well as on the alignment of the reflected beam on the photodiode, it is less suitable for automated operations.

Piezoresistive sensing concept:
Another way to sense the cantilever deflection is based on piezoresistive detection. This technique relies on the property of a crystalline material to change its resistivity when exposed to shear stress [75]. Thus, the cantilever deflection can be sensed electrically by measuring this resistivity change. Implementing such a piezoresistor on the cantilever enables the microscope to have both force detection and XYZ scanning on the instrument side, while the sample stays in place. Figure 1-12 illustrates the described differences.

Other detection concepts:
There are several other ways to sense the deflection of a cantilever. By implementing a second, more rigid cantilever on top of the first one, playing the role of a counter-electrode, one can sense a capacitive change between the two layers related to the cantilever movement [76]. Another method consists in implementing interdigitated combs on the cantilever edges. By using electrostatic effects between the moving combs, the cantilever deflection can be related to the changing electrical potential [77]. Both techniques (capacitive and electrostatic) can also be used to actuate the cantilever to produce the feedback control or excite the cantilever at its mechanical resonance.

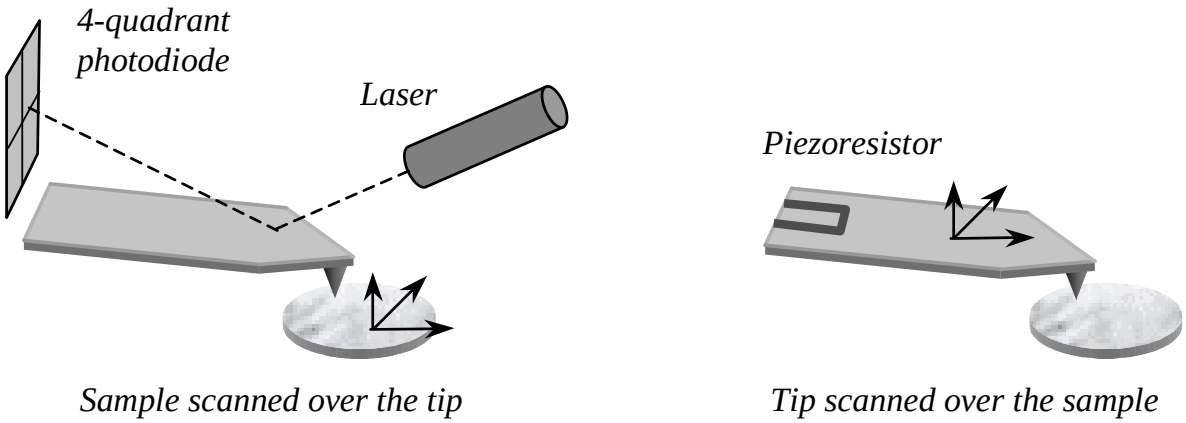

Figure 1-12
Architecture and scanning movement comparison between laser detection (left) and piezo-resistive detection (right).

1.6 MEMS for space

Micro-Electromechanical Systems (MEMS) is the integration of mechanical elements, sensors, actuators, and electronics on a common silicon substrate through the utilization of microfabrication technology. Manufacturing of MEMS has its origins in Integrated Circuit (IC) processing. It has progressed from that to more sophisticated processes driven by the need to create 3-D features.
In the past 20 years, the market for MEMS has increased drastically due to its small size, robust mechanical properties and sensitivity for measuring physical signals. The automotive, medical and communication industry has already implemented MEMS component successfully.
In the space industry, in particular for non-commercial applications, the implementation of new technologies always takes a longer time. The biggest issue for space engineers is to match the interfaces between existing macromechanical systems and the much smaller MEMS components.

1.6.1 MEMS for satellites

The use of MEMS to implement ultra-miniaturized spacecraft subsystems can potentially address the requirements for shock survivability, radiation tolerance, low-power consumption and mass and volume constraints. They will be the key for new commercial space activities since they enhance the payload / total mass ratio at launch for instance of telecommunication satellites. Today's commercial satellites have a total mass of several thousands of kilograms. Future satellites will focus on smaller mass by keeping or increasing its functionality. The following terminology relating the satellite to its mass is commonly used:

Small satellite: < 1000kg
Microsatellite: < 100kg
Nanosatellite: < 10kg
Picosatellite: < 1kg

Just as with the insertion of new technologies into the commercial sector, the development of technologies for space applications faces significant challenges in ultimately being inserted into space missions. This will be done in two steps: on a short term, by widely spreading MEMS components within state of the art satellites and its subsystems, in a longer term, by reconsidering the satellite itself and build fully integrated micro or nanosatellites. The ultimate goal is to batch process those satellites and have them communicate in a network. A cluster of many satellites will reduce the risk of mission failure and increase mission flexibility. The use of today's space telescopes with large mirrors might one day be replaced by a myriad of satellites collecting the same amount of light and producing even sharper images. The

use of pico-satellites for extremely agile, launch-on-demand and short-term missions for security and defence purpose will be another hot topic.
Some of the MEMS components necessary to realize this vision are already present in today's market. Navigation components like gyroscopes and accelerometers have been successfully implemented by the automotive industry. RF components and optical switches based on MEMS are used in the communication industry and can be a starting point for developing communication systems in space.
Other macroscopic components present on today's satellites will have to be completely re-invented on the micro scale. This is the case for power supplies, data storage and particularly propulsion systems. An additional challenge consists in realizing the interconnections between these small elements and to encapsulate them in a space compatible manner.

1.6.2 MEMS for Planetary exploration

Space exploration in the coming century will emphasize on cost effectiveness and highly focused mission objectives. MEMS will be one of the enabling technologies to create small cost, ultra-miniaturized, robust, and functionally focused spacecraft for both robotic and human exploration programs. MEMS sensors measuring physical values like pressure, temperature or displacements have proven to be reliable tools for earthbound applications. Due to their small size and weight, they are also ideal components for space instruments to be sent to foreign planets.
Today, every kilogram sent to Mars costs about $1 million. The potential of sending a fully integrated spacecraft weighing a few tens of kilograms instead of the thousands of kilos will offer significant monetary benefits.

1.7 References

1 : T. Akiyama, U. Staufer, N.F. de Rooij, D. Lange, C. Hagleitner, O. Brand, H. Baltes, A. Tonin H.R. Hidber, “Integrated Atomic Force Microscopy Array Probe with Metal-Oxide-Semiconductor Field Effect Transistor Stress Sensor, Thermal Bimorph Actuator, and On-chip Complementary Metal-Oxide-Semiconductor Electronics”, J. Vac. Sci. Technol. **B18**, 2669, (2000).

2 : “Towards mars! ”, OY Raud Publishing Ltd. Helsinki, ISBN 952-9689-11-X, (2000).

3 : L.J. Martin, R.W. Zurek, “An Analysis of the History of Dust Activity on Mars”, Journal of Geophysical Research, **98**(E2), 3221, (1993).

4 : S.M. Metger, “Recent Advances in Understanding Dust Devil Processes and Sediment Flux on Earth and Mars”, 32nd Annual Lunar and Planetary Science Conference, (2001).

5 : R.W. Zurek, L.J. Martin, “Interannual Variability of Planet-Encircling Dust Storms on Mars”, Journal of Geophysical research, **98**(E2), 3247, (1993).

6 : NASA press release, 01-193, “Scientists Track "Perfect Storm" on Mars”, (2001).

7 : MGS MOC Release No. MOC2-290.

8 : P. Toulmin, A.K. Baird, B.C. Clark, K. Keil, H.J. Rose, P.R. Christensen, P.H. Evans, W.C. Kelliher, “ Geo-chemical and Mineralogical Interpretation of the Viking Inorganic Chemical Results”, Journal of Geophysical Research, **82**, 4625, (1977).

9 : Based on the review by Dr J Floor Anthoni, http://www.seafriends.org.nz/enviro/soil/rocktbl.htm

10 : J.B. Pollack, O.W. Toon, B.N. Khare, “Optical Properties of Some Terrestrial Rocks and Glasses”, Icarus, **19**, 372, (1973).

11 : http://tes.asu.edu/webdata/3looks.html

12 : W. Sheehan, “The Planet Mars: A History of Observation and Discovery”, The University of Arizona Press, (1996).

13 : E. M. Antoniadi, "Mars Report, 1909", Memoirs of the British Astronomical Association, **20**, 37, (1915).

14 : Dean B. McLaughlin, "Volcanism and Aeolian Deposition on Mars," Geological Society of America Bulletin, **65**, 715, (1954).

15 : L. D. Kaplan, G. Münch, and H. Spinrad, "An Analysis of the Spectrum of Mars," Astrophysical Journal, **139**, 1, (1964).

16 : R. Greeley, M. Craft, R. Sullivan, G. Wilson, N. Bridges, K. Herkenhoff, R. Kuzmin, M. Malin, W. Ward, “Aeolian Features and Processes at the Mars Pathfinder Landing Site”, Journal of Geophysical Research, **104** (E4), 8573, (1999).

17 : R.A. Hanel, B.J. Conrath, W.A. Hovis, V.G. Kunde, P.D. Lowman, J.C. Pearl, C. Prabhakara, B. Schlachman, G.V. Levin, “Infrared Spectroscopy Experiment on the Mariner 9 Mission: Preliminary Results”, Science, **175**, 305, (1972).

18 : R.J. Curran, B.J. Conrad, R.A. Hanel, V.G. Kunde, K.C. Pearl, “Mars: Mariner 9 Spectroscopic Evidence for H_2O Ice Clouds”, Science, **182**, 381, (1973).

19 : O.B. Toon, J.B. Pollack, C. Sagan, “Physical Properties of the Particles Composing the Martian Dust Storm of 1971-1972”, Icarus, **30**, 663, (1977).

20 : R.T. Clancy, S.W. Lee, G.R. Gladstone, W.W. McMillan, T. Rouch, “A New Model for Mars Atmospheric Dust Based upon Analysis of Ultraviolet through Infrared Observations from Mariner 9, Viking, and Phobos”, Journal of Geophysical Research, **100**, 5251, (1995).

21 : N.A. Stroncik, H.-U. Schmincke, “Evolution of Palagonite: Crystallization, Chemical Changes, and Element Budget”, Geochemistry, Geophysics, Geosystems, **2**, (2001).

22 : T.L. Roush, J.B. Bell, “Thermal Emission Measurements 2000-400 cm-1 (5-25 μm) of Hawaiian Palagonitic Soils and their Implications for Mars”, Journal of Geophysical Research, **100**(E3), 5309, (1995).

23 : V. Formisano, D. Grassi, G. Piccioni, J. Pearl, R. Hanel, G. Bjoraker, B. Conrath, “IRIS Mariner 9 Data Revisited: An Instrumental Effect”, 31st Annual meeting of the DPS, (1999).

24 : D. Grassi, V. Formisano, " IRIS Mariner 9 Data Revisited: Aerosol Composition ", 31st Annual meeting of the DPS, (1999).
25 : "Scientific Results of the Viking Project", Journal of Geophysical Research, **82**(28), (1977).
26 : J. B. Pollack, D. S. Colburn, F. M. Flasar, R. Kahn, C. E. Carlston, and D. Pidek, "Properties and effects of dust particles suspended in the Martian atmosphere", Journal of Geophysical Research, **84**, 2929, (1979).
27 : J.B. Pollack, M.E. Ockertbell, M.K. Shepard, "Viking Lander Image-Analysis of Martian Athmospheric Dust, Journal of Geophysical Research Planets, **100** (E3), 5235, (1995).
28 : H.H. Kiefer, T.Z. Martin, A.R. Peterfreund, B.M. Jakosky, E.D. Minner, D.D. Palluconi, "Thermal and Albedo Mapping of Mars During the Viking Primary Mission", Journal of Geophysical Research, 82, 4249, (1977).
29 : R.T. Clancy, S.W. Lee, " A New Look at Dust and Clouds in the Mars Atmosphere: Analysis of Emission-Phase-Function Sequences from Global Viking IRTM Observations", Icarus, **93**, PP 135, (1991).
30 : J.B. Pollack, D.S. Coburn, R. Kahn, J. Hunter, W. Van Camp, C.E. Carlston, M.R. Wolfe, "Properties of Aerosols in the Martian Atmosphere, as Inferred from Viking Lander Imaging Data", Journal of Geophysical Research, **82**, 4479, (1977).
31 : D.V. Michelangeli, O.B. Toon, R.B. Haberle, J.B. Pollack, "Numerical Simulations of the Formation and Evolution of Water Ice Clouds in the Martian Atmosphere, Icarus, **100**, 261, (1993).
32 : F. Montmessin, P. Rannou, M. Cabane, "New Insights into Martian Dust Distribution and Water-Ice Cloud Microphysics", Journal of Geophysical Research, **107** (E6), (2002).
33 : G.A. D'Almeida, "On the Variability of Desert Aerolsols Radiative Characteristics", Journal of Geophysical Research, **92**, 3017, (1987).
34 : E. Chassefière, P. Drossart, O. Korablev, "Post-Phobos Model for the Altitude and Size distribution of the Dust in the Low Martian Atmosphere ", Journal of Geophysical Research, **100**(E3), 5525, (1995).
35 : S. Erard, J. Mustard, S. Murchie, J.-P. Bibring, P. Cerroni, A. Coradini, "Martian Aerosols: Near-Infrared Spectral Properties and Effects on the Observation of the Surface", Icarus, **111**, 317, (1994).
36 : M.G. Tomasko, L.R. Doose, M. Lemmon, P.H. Smith, E. Wegryn, "Properties of Dust in the Martian Atmosphere from the Imager on Mars Pathfinder", Journal of Geophysical Research, **104**(E4), 8987, (1999).
37 : J.R. Matijevic, J. Crisp, D.B. Bickler, R.S. Banes, B.K. Cooper, H.J. Eisen, J. Gensler, A. Haldemann, F. Hartman, K.A. Jewett, L.H. Matthies, S.L. Laubach, A.H. Mishkin, J.C. Morrison, T.T. Nguyen, A.R. Sirota, H.W. Stone, S. Stride, L.F. Sword, J.A. Tarsala, A.D. Thompson, M.T. Wallace, R. Welch, E. Wellman, B.H. Wilcox, D. Ferguson, P. Jenkins, J. Kolecki, G.A. Landis, D. Wilt, "Characterization of the Martian Surface Deposits by the Mars Pathfinder Rover, Sojourner", Science, **278**, 1765, (1997).
38 : M.P. Golombek, R.A. Cook, T. Economou, W.M. Folkner, A.F.C. Haldemann, P.H. Kallemeyn, J.M. Knudsen, R.M. Manning, H.J. Moore, T.J. Parker, R. Riedler, J.T. Schofield, P.H. Smith, R.M. Vaughan, " Overview of the Mars Pathfinder Mission and Assessment of Landing Site Predictions", Science, **278**, (1997).
39 : R. Rieder, T. Economou, H. Wänke, A. Turkevich, J. Crisp, J. Brückner, G. Dreibus, H.Y. McSween Jr, " The Chemical Composition of Martian Soil and Rocks Returned by the Mobile Proton X-Ray Spectrometer: Preliminary Results from the X-Ray Mode", Science, **278**, 1771, (1997).
40 : S.F. Hviid, M.B. Madsen, H.P. Gunnlaugsonn, W. Goetz, J.M. Knudsen, R.B. Hargraves, P. Smith, D. Britt, A.R. Dinesen, C.T. Morgensen, M. Olsen, C.T. Petersen, L. Vistisen, "Magnetic Properties Experiments on the Mars Pathfinder Lander: Preliminary Results", Science, **278**, 1768, (1997).
41 : G.A. Landis, P.P. Jenkins, "Dust on mars: Materials Adherence Experiment Results from Mars Pathfinder", Proc of the 26th IEEE Photovoltaic specialists conference, IEEE, NJ, 865, ISBN 0-7803-3767-0.
42 : G.A. Landis,"Dust Obscuration of Mars Solar Arrays", Acta Astronautica, **38**, 885, (1996).
43 : J. R. Aronson, A.G. Emslie, "Composition of the Martian Dust as Derived by Infrared Spectroscopy From Mariner 9", Journal of Geophysical research, **80** (35), 4925, (1975).

44 : K. Pang, J.M. Ajello, C.W. Hord, W.G. Egan, “Complex Refractive Index of Martian Dust: Mariner 9 ultraviolet observations”, Icarus, **27**, 55, (1976).
45 : P. Chylek, G.W. Grams “ Scattering by Nonspherical Particles and Optical Properties of Martian Dust”, Icarus, **36**, 198, (1978).
46 : V.I. Moroz, E.V. Petrova, L.V. Ksanformaliti, L.W. Esposito, J.-P, Bibring, M. Combes, A. Soufflot, O.F. Gantpantserova, N.V. Goroshkova, A.V. Zharkov, G.E. Nikitin, “Aerosol in the Atmosphere of Mars: KRFM data”, Soviet Astronomy Letters, **17**(3), 235, (1991).
47 : O.I. Korablev, V.A. Krasnopolsky, A.V. Rodin, “ Vertical Structure of Martian Dust Measured by Solar Infrared Occultation from the Phobos Spacecraft”, Icarus, **102**, 76, (1993).
48 : M. Santee, D. Crisp, “Thermal Structure and Dust Loading of the Martian Atmosphere During Late Southern Summer: Mariner 9 Revisited”, Journal of Geophysical Research, **98**(E2), 3261, (1993).
49 : P.H. Smith, J.F. Bell, N.T. Bridges, D.T. Britt, L. Gaddis, R. Greeley, H.U. Keller, K.E. Herkenhoff, R. Jaumann, J.R. Johnson, R.L. Kirk, M. Lemmon, J.N. Maki, M.C. Malin, S.L. Murchie, J. Oberst, T.J. Parker, R.J. Reid, R. Sablotny, L.A. Soderblom, C. Stoker, R. Sullivan, N. Thomas, M.G. Tomasko, W. Ward, E. Wegryn, “Results from the Mars Pathfinder Camera”, Science, **278**, 1758, (1997).
50 : W. J. Markiewicz, R. M. Sablotny, H. U. Keller, N. Thomas, D. Titiv, P. H. Smith, "Properties of Martian Aerosols Derived from Imager for Mars Pathfinder Midday Sky Brightness Data", Journal of Geophysical Research , **104**, 9009, (1999).
51 : P.R. Christensen, D.L. Anderson, S.C. Chase, R.N. Clark, H.H. Kiefer, M.C. Malin, J.C. Pearl, J.C. Carpenter, N. Bandiera, F.G. Brown, S. Silverman, “Thermal Emission Spectrometer Experiment: Mars Observer Mission”, Journal of Geophysical Research, **97**(E5), 7719, (1992).
52 J.C. Pearl, M.D. Smith, B.J. Conrath, J.L Bandfield, P.R. Christensen, “Observations of Martian Ice Clouds by the Mars Global Surveyor Thermal Emission Spectrometer: The First Martian Year”, Journal of Geophysical Research, **106**(E6), 12325, (2001).
53 : M.D. Smith, J.L Bandfield, P.R. Christensen, “ Separation of Atmospheric and Surface Spectral Features in Mars Global Surveyor Thermal Emission Spectrometer (TES) Spectra”, Journal of Geophysical Research, **105**(E4), PP 9589-9607, (2000).
54 : K.M. Pitman, M.J. Wolff, R.T. Clancy, C.C. Clayton, “On the Shape of Martian Dust and Water Ice Aerosols”, DPS meeting, Pasadena, (2000).
55: M.J. Wolff , K.M. Pitman, , R.T. Clancy, J.F. Bell, P.B. James, , “Constraints on Martian Aerosol Particles Using MGS/TES and HST Data: Shapes”, AGU meeting, San Francisco, (2001).
56 : M. Duke, “The Rationale for Exploring Mars”, NASA Johnson Space Flight Center, www.solarviews.com/eng/marswhy.htm.
57 : http://www.thinkmars.net/humanstomars/whymars.html.
58 : http://www.arctic-mars.org.
59 : M.H. Hecht, T.P. Meloy, J.R. Marshall, “The Mars Environmental Compatibility Assessment (MECA)”, Proc of the Concepts and Approaches for Mars Exploration conference, Houston Texas, (2000).
60 : B. G. Drake - Mars Reference Mission V 3.0, (1998), http://spaceflight.nasa.gov/mars/reference/hem/hem2.html
61 : National Research council, “Safe on Mars, Precursor Measurements Necessary to Support Human Operations on the Martian Surface”, National Academy Press, ISBN 0-309-08426-1, (2002).
62 : P. Kokh, ”Moon Miners' Manifesto, Dust Control”, #89, Section 6.9.3.2.089.of the Artemis Data Book, (1995).
63 : J.C. Kolecki, G.A. Landis, “Electrical Discharge on the Martian Surface”, http://powerweb.grc.nasa.gov/pvsee/publications/marslight.html, (1996).
64 : J. A. Mineo, American Insurance Service Group, Silicosis in Construction, http://www.osha-slc.gov/SLTC/silicacrystalline/mineoja/demolition.html.
65 : U.S departement of health, education and welfare - Criteria for a Recommended Standard, Occupational Exposure to Crystalline Silica, HEW Publication No. (NIOSH) 75-120, (1974).
66 : “Occupational exposure to free silica”, OSHA, (1974).

67 : S.J. West, M.S. Frant, X. Wen, R. Geis, J. Herdan, T. Gillette, M.H. Hecht, W. Schubert, S. Grannen, S.P. Kounaves, “Electrochemistry on mars”, Electrochemistry, American Laboratory, **20**, 48, (1999).
68 : S.P.Kounaves, M.G. Buehler, M.H. Hecht, S. West, “Determination of Geochemistry on Mars Using an Array of Electrochemical Sensors”, Environmental Chemistry, 306, ISBN: 0-8112-3774-3, (2002).
69 : K.R. Kuhlman, M.S. Anderson, B.D. Hinde, M.H. Hecht, W.T. Pike, J.R. Marshall, T.P meloy, “The Mars Envrironmental Compatibility Assessment Project (MECA) Abrasion tool”, Fifth International Conference on Mars, Pasadena, (1999).
70 : “History of the Mars Lander”, http:/www.savethemarslander.org.
71 : G. Binnig, H. Rohrer, Ch. Gerber, E. Weibel, “Surface Studies by Scanning Tunneling Microscopy”, Physical Review Letters, **49**, 57, (1982).
72 : G. Binnig, C. F. Quate, Ch. Gerber, “Atomic Force Microscope”, Physical Review Letters, **56**, 930, (1986).
73 : H. Bühler, Electronique de réglage et de commande, Traité d'Electricité, vol XVI, Lausanne 1987, ISBN: 2-88074-056-8
74 : U. Dürig, H.R. Steinauer, N. Blanc, “Dynamic Force Microscopy by Means of the Phase-controlled Oscillator Method”, Journal of Applied Physics, **82**, 3641, (1997).
75 : M. Tortonese, R.C. Barrett, C.F. Quate, “Atomic Resolution with an Atomic Force Microscope Using Piezoresistive Detection”, Applied Physics Letters, **62**, 834, (1992).
76 : N. Blanc, J. Brugger, N.F. de Rooij, ”Scanning Force Microscopy in the Dynamic Mode Using Microfabricated Capacitive Sensors”, J. Vac. Sci. Technol. **B 14**(2), 901, (1996).
77: T. Akiyama, U. Staufer, N.F. De Rooij, “Atomic Force Microscopy Using an Integrated Comb-shape Electrostatic Actuator for High-Speed Feedback Motion”, Applied Physics Letters, **76**, 3139, (2000).

2. FAMARS DESIGN

The realization of the AFM instrument has been the result of a very close collaboration between three different partners: The company Nanosurf AG (NS), The Institute of Physics of the University of Basel (IFP) and the institute of Microtechnology of the University of Neuchâtel (IMT). The task distribution between the partners was the following:
The electronics design, assembly and characterization has been realized by IFP in collaboration with NS. The scanner design and parts fabrication has been performed by NS. The assembly, optimisation and characterization of the scanner have been done by myself at IMT. The design of the first generation sensor array has been the task of Terunobu Akiyama from IMT. The microfabrication of this first generation, as well as the redesign and FE analysis has been performed by myself in collaboration with T. Akiyama. The implementation of the instrument into the payload MECA has been performed by myself in collaboration with Tom Pike from JPL.
The first section of this chapter describes the different limitations to render the instrument space compatible. Section 2, 3 and 4 describe the critical design steps and the architecture for each sub-component of the microscope.
The software that drives the instrument is based on autonomous operation schemes that were developed to face the communication delay between Earth and Mars. Section 5 of this chapter highlights basic sequences of autonomous operation.
Finally, the instrument characterization and environmental testing as well as the mission plan on Mars are described in section 6. [1, 2, 3, 4, 5, 6, 7, 8].

2.1 Space qualification requirements

2.1.1 Weight, mass and power

Launch-costs for space missions are proportional to weight and volume. Each payload has a certain mass and space allocate on the lander platform. The initial mass allocation for the AFM is 250g for instrument and electronics. As the AFM will sit right in front of the optical microscope of MECA (see § 1.4.3) to allow overlapping of optical and AFM images, its volume was very limited (3 x 5 x 1.5 cm). By keeping the total mass of the FAMARS instrument as low as possible, constraints could be relaxed for other components of MECA. The total mass allocated for MECA is 8.5 Kg. During daytime operations, MECA will not exceed 15 W, which will allow simultaneous operation with other payloads.

2.1.2 Shock and vibration

The instrument will be exposed to random vibrations during the launch of the Delta 2 rocket and to high shocks during the separation of the launcher from the cruise stage, and during the separation of the back shell before entering the atmosphere of Mars [9]. In its cruise configuration, the lander is divided into different zones like the bottom cover, the instrument and component deck, the cruise stage and the aero shell environment. Each zone will behave differently under random vibration and shock. Thus, protoflight and acceptance levels are specified for each zone separately.

2.1.3 Temperature and pressure

The temperature range to which the instrument will be exposed is very large. Storage temperatures on Earth before launch go up to 50°C to account for heating effects during functionality tests in launch configuration. On the other extreme, the night temperatures on Mars will go down to –120°C. Thus, the instrument will be exposed to repeated temperatures cycles with high amplitude (typically 100°C). The temperatures for operation during Martian daytimes will range from +20°C to –40°C [9].
During cruise, certain materials will outgas due to the vacuum that reigns in space. Molecules will come-out of some polymers because of the low molecular weight and their higher vapour pressure. Thus, only space-qualified materials with low outgassing coefficients could be used to build the FAMARS instrument.
The pressure on Mars is hundred times smaller than on Earth. This characteristic is important when considering electrostatic discharge and arcing due to the generation of high voltages. The AFM power requirement was therefore limited to low voltages.

2.1.4 Radiation

The radiation coming from space is composed of solar flare radiation and cosmic rays. Most of a solar flare's energy is in alpha and beta particles, which can be stopped with a few centimeters of shielding. Cosmic rays consist of heavy, slow-moving atomic nuclei that can do far more damage than alpha and beta particles. This radiation requires several meters of shielding for complete blockage. Heavy ions come from all directions at all times, unlike the brief solar flares that last only a few hours or days.
Although the Martian atmosphere does not have a magnetic field like Earth, its atmosphere provides significant shielding from the solar flare radiation. For a shielding thickness of 570 μm of aluminum, the total dose radiation is reduced by a factor of almost 200 compared to outer space. In outer space, the total dose behind a 2.54 mm thick aluminum shielding is 1.43 kRads per year of cruise. Radiation hard

components with specifications up to 1000 kRads can therefore be used to shield the electronic circuitry during cruise and on Mars.
The single event radiation levels on the surface of Mars produced by heavy ions depend on the linear energy transfer in the matter (LET) expressed in MeV/(mg/cm^2). For radiation hard components with a typical LET threshold of 35, the number of single event upsets per cm^2 and per day is 2 E^{-5}, whereas the number of single event latch-ups is considered to be zero.

2.1.5 Autonomy

Another limitation is due to the relative position of the lander, the communication satellite around Mars, and Earth. Commands to the Mars Lander can be sent only twice every day. No direct interaction with the payloads is possible since the communication delay will range from 8 to 20 minutes. This restriction significantly influences the measuring protocol and the software that runs the instrument. Autonomous operation concepts had to be developed to meet these requirements.

2.1.6 Planetary protection

During assembly of the AFM, special means had to be used to meet the planetary protection requirements [10]. These requirements provide a biological contamination control for planetary spacecrafts. It is specifically directed to the control of terrestrial contamination associated with robotic missions intended to land on a foreign planet. Protection of the planetary environment facilitates also exobiological investigations of Mars by minimizing the possibility that an exobiological finding would have originated on Earth.

2.2 AFM chip design

The principal function of the AFM chip is the precise sensing of the topography of the surface. To do so, it requires a sharp tip and a cantilever with a small spring constant. A high resonance frequency of the cantilever will allow a faster scanning speed and make the probe less sensitive to parasitic vibrations, which are often in the low frequency range. Additionally, the deflection read-out technique must be as less space taking as possible. Finally, the design of a whole array of cantilevers is necessary to give the instrument some redundancy in case of a broken cantilever or a dull tip.
These challenges led to the conclusion that only micro-fabrication techniques for shaping mono-crystalline silicon could meet those requirements. The following points highlight the advantages of microfabrication:

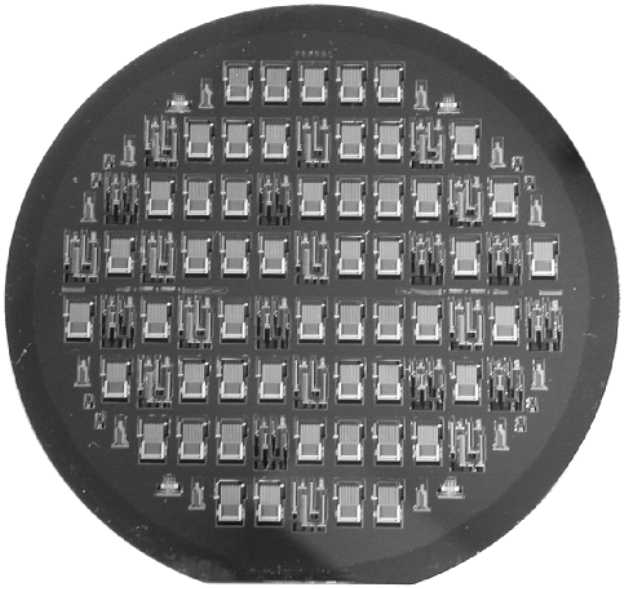

Figure 2-1
4-inch SOI wafer with processed AFM chips.

- Anisotropic wet etching [15] is a well-known technique for fabricating sharp silicon tips. The small structures that can be achieved by silicon micro-machining help to reduce the spring- constant of the cantilever to act with a very low force on the sample by keeping a high resonance frequency.
- The implantation of piezo-resistors into the cantilevers [11] to electrically read the surface stress created by the deflected cantilever is a much less space taking technique than optical read-out (see § 1.5.3).
- Deep reactive ion etching of silicon enabled the creation an array of 8 thick beams on a narrow space to support the cantilevers. These balks will enable the removal of a cantilever by simple cleavage.

In addition, microfabrication allow batch processing, and therefore the creation of several chips in one run. Figure 2-1 shows a photograph of processed silicon wafer with 60 FAMARS chips. Figure 2-2 shows a SEM image of a single AFM chip.

2.2.1 Silicon and diamond tips

The cantilevers are alternately equipped with monolithic silicon tips and CVD moulded diamond tips. Both types of tips have their advantages and drawbacks for producing good images during the mission.

Diamond tips
The diamond tips were incorporated as a low-wear material since its hardness exceed by far those made out of silicon. Since in most cases quartz particles much harder than silicon are expected to be present on the sample, the use of diamond tips will avoid fast wear of the tip apex and deterioration of the image quality by tip convolution (see the chapter 3). These diamond tips are fabricated by chemical vapour

deposition (CVD) into pyramidal pits in silicon[1] [12]. Due to the etching angle in {100} orientated silicon, the tip opening angle is quite large and the tip aspect ratio is quite low. When imaging 3 dimensional structures like particles or piles of particles, the image will have to be post-processed to extract the actual substrate topography.
Mounting of the diamond tips on the odd numbered cantilevers is performed at the end of the fabrication process described in § 2.2.3. This is performed on a chip-by-chip basis using a micromanipulator to accurately place the tips at the edge of the cantilevers[1] [13]. Finally, parts of the diamond tip that jut the border of the cantilever are trimmed by a focused ion beam[2] [14]. Figure 2-3 a) shows a mounted diamond tip with trimmed edges.

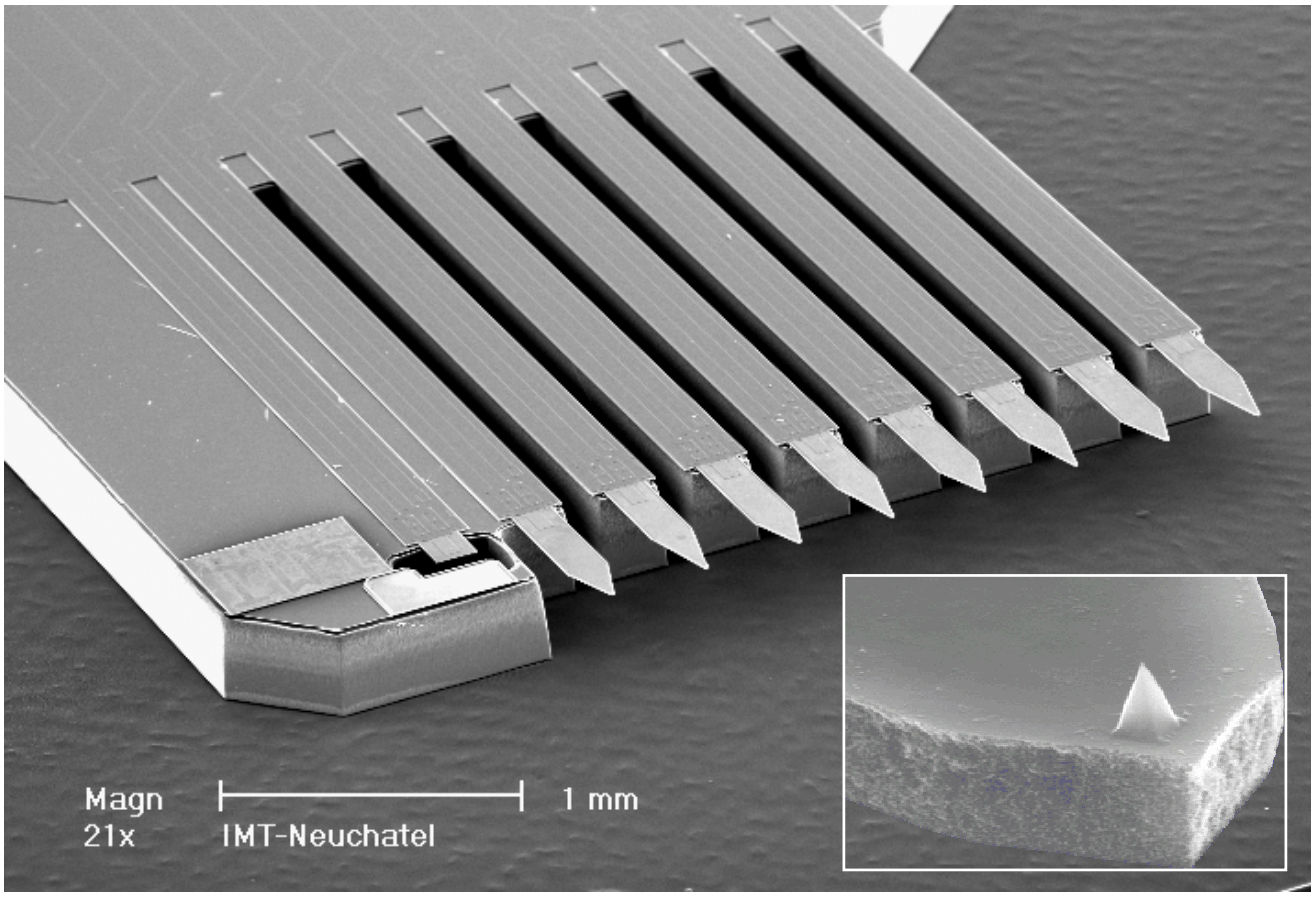

Figure 2-2
SEM image of the AFM chip. 8 cantilevers are located at the end of thick support beams. A sharp tip is located at the edge of each cantilever (see inset). A reference sensor is implemented on the far left to compensate for thermal drifts.

[1] Performed by CSEM, Neuchâtel.
[2] Performed PSI, Villigen.

Silicon tips
Silicon tips are monolithically shaped on the cantilever by anisotropic etching in KOH [15] (see Figure 2-5 step a). This technique creates tips with a smaller opening angle (35°) and a higher aspect ratio, which is more suited for imaging large features with an aspect ratio of 1 like micron-sized particles. Figure 2-3 b) shows an SEM image of a silicon tip at the edge of a cantilever.

a) *b)*

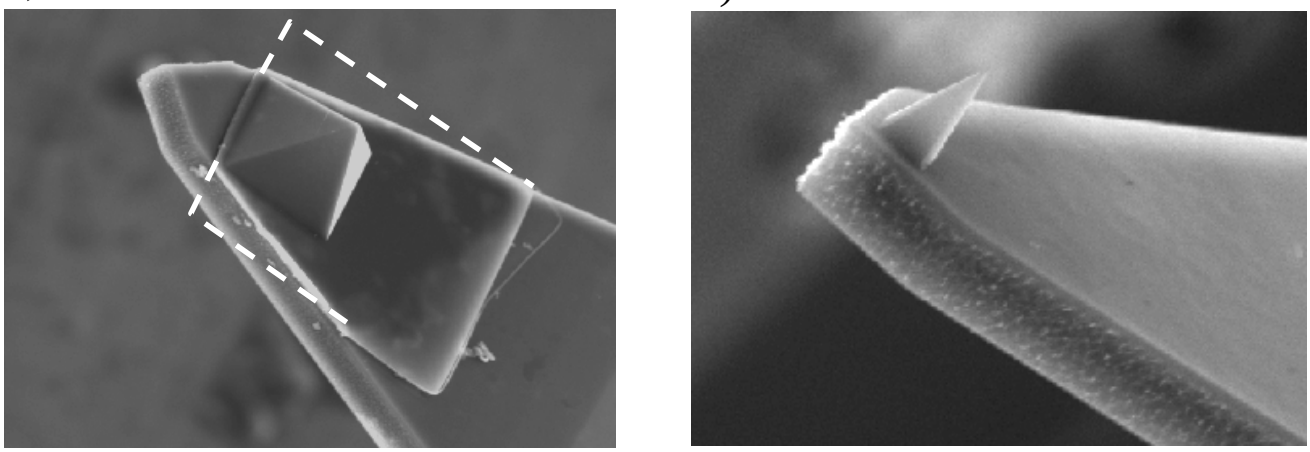

Figure 2-3

a) SEM image of moulded diamond tip mounted on a cantilever. The previously trimmed edges of the diamond mould are highlighted in dashed lines.
b) SEM image of a silicon tip at the edge of a cantilever.

2.2.2 Piezo-resistive detection

The cantilever deflection is measured by means of implanted piezoresistors [11]. Each sensor will be contacted separately to the electronics to allow multiplexing. A reference resistor is incorporated on an ultra-short cantilever for compensating thermal variations. This reference cantilever is protected against mechanical damage by a surrounding, rigid safety bar (see Figure 2-2).
Electrical isolation between the piezo-resistors and the cantilevers is achieved by reverse biasing the pn-junction formed between the p-type resistors and the n-type bulk of the cantilever.
A buried contact path enables the modification of the potential of the cantilevers. It is expected that in the dry Martian atmosphere, electrostatic forces between the sample and the tip will be present. The ability to change the tip potential is therefore important to, at least partially, compensate for these forces. Figure 2-4 shows a SEM image of the AFM chip with its electrical contact paths to the cantilever and to the piezoresistors.

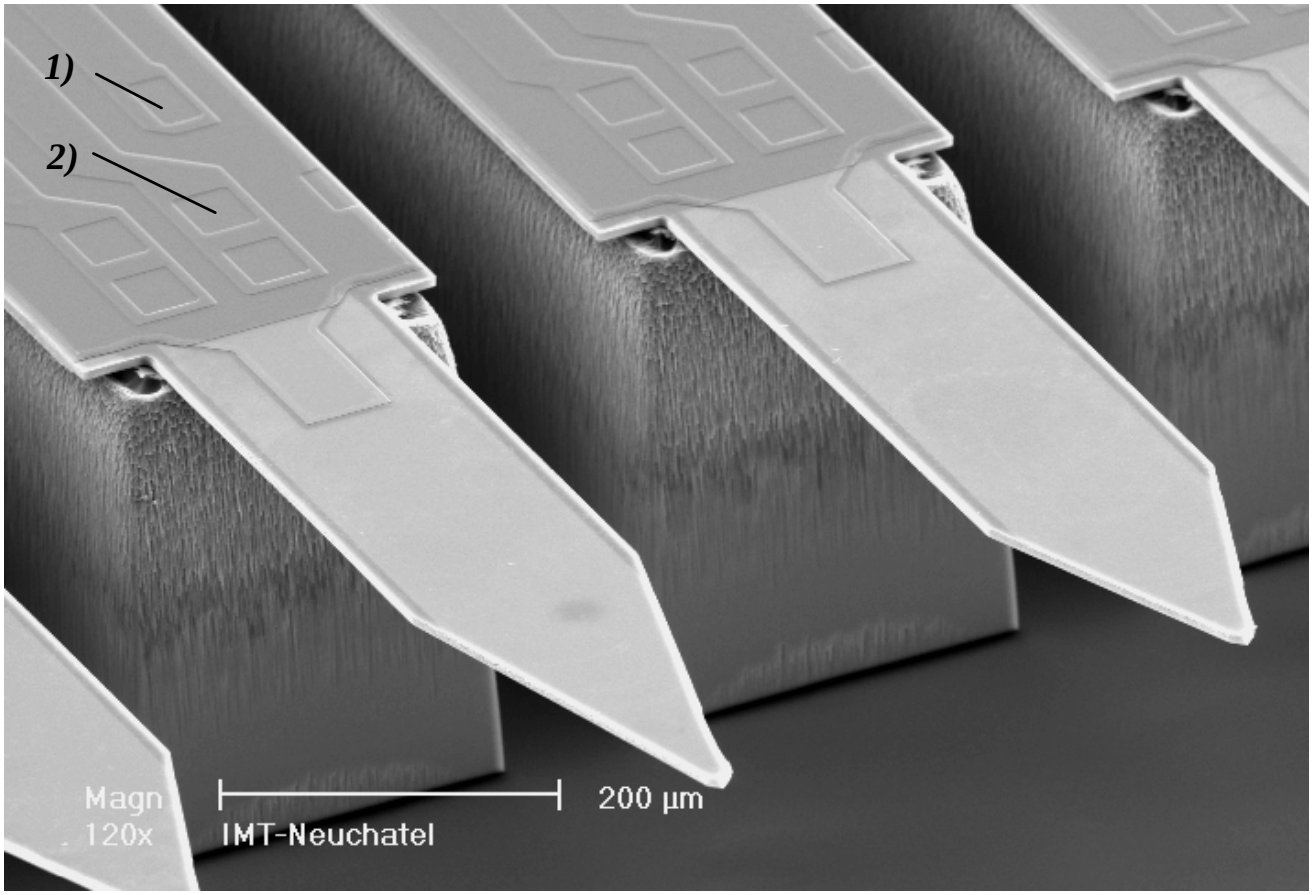

Figure 2-4
Close-up SEM image of the sensor array with contact paths to set the cantilever potential (1) and to contact the piezoresistors implanted on the cantilevers (2).

2.2.3 Fabrication steps

The following section describes in detail the fabrication steps of the AFM chip. A n-type silicon-on-oxide wafer (SOI) is used to define the top layer for the cantilevers and the bottom layer for the thick support beams. The wafer has a device layer of 21 µm and a bulk thickness of 380 µm.
In a first step (step a), 8µm high silicon tips are fabricated for every second cantilever by wet etching the device layer in KOH and using square thermal-oxide masks. The other four cantilevers will be equipped with diamond tips in a post-process step. Then phosphor-silicate glass (PSG) and silicon-oxide films are deposited in a chemical-vapour deposition (CVD) process. These films are then structured by photolithography and wet etching. The photoresist and the oxide are used as mask during boron ion-implantation for creating the piezoresistors on the cantilevers (step b). After stripping the mask, CVD oxide is again deposited, followed by a thermal treatment at 950 C for 30 minutes to activate the dopant. The oxide is replaced by a fresh layer for passivation and protection during subsequent processing (steps c and d respectively). A third lithography structures a resist layer used as mask to wet etch the contact holes into the oxide to the piezoresistors. A layer of aluminium is deposited

and wet etched after the next lithography to define the contact paths and pads (step e). Step f depicts the passivation process of the chip through deposition of plasma nitride and a fifth lithography to structure it. This nitride structuring is used to open the contact pads. The oxide layer remaining on the silicon is structured by lithography and wet etching and used as a mask to define the top shape of the cantilevers (step g). Step h shows the last top lithography for removing the remaining oxide on the cantilevers. The top resist is also used as a protection layer for the backside deep reactive ion etching (DRIE) which defines the support beams and the final chip shape. For this backside etching, lithography on the back of the wafer is performed. The oxide layer underneath the cantilever is used as an etch stop. As a final step, the oxide remaining underneath the cantilever is removed by wet etching (step i). At the end of the process, the individual AFM chips are still connected to a silicon frame via thin bridges. They are easily broken for removing the chips. Figure 2-1 shows a picture a 4-inch wafer with processed AFM chips.

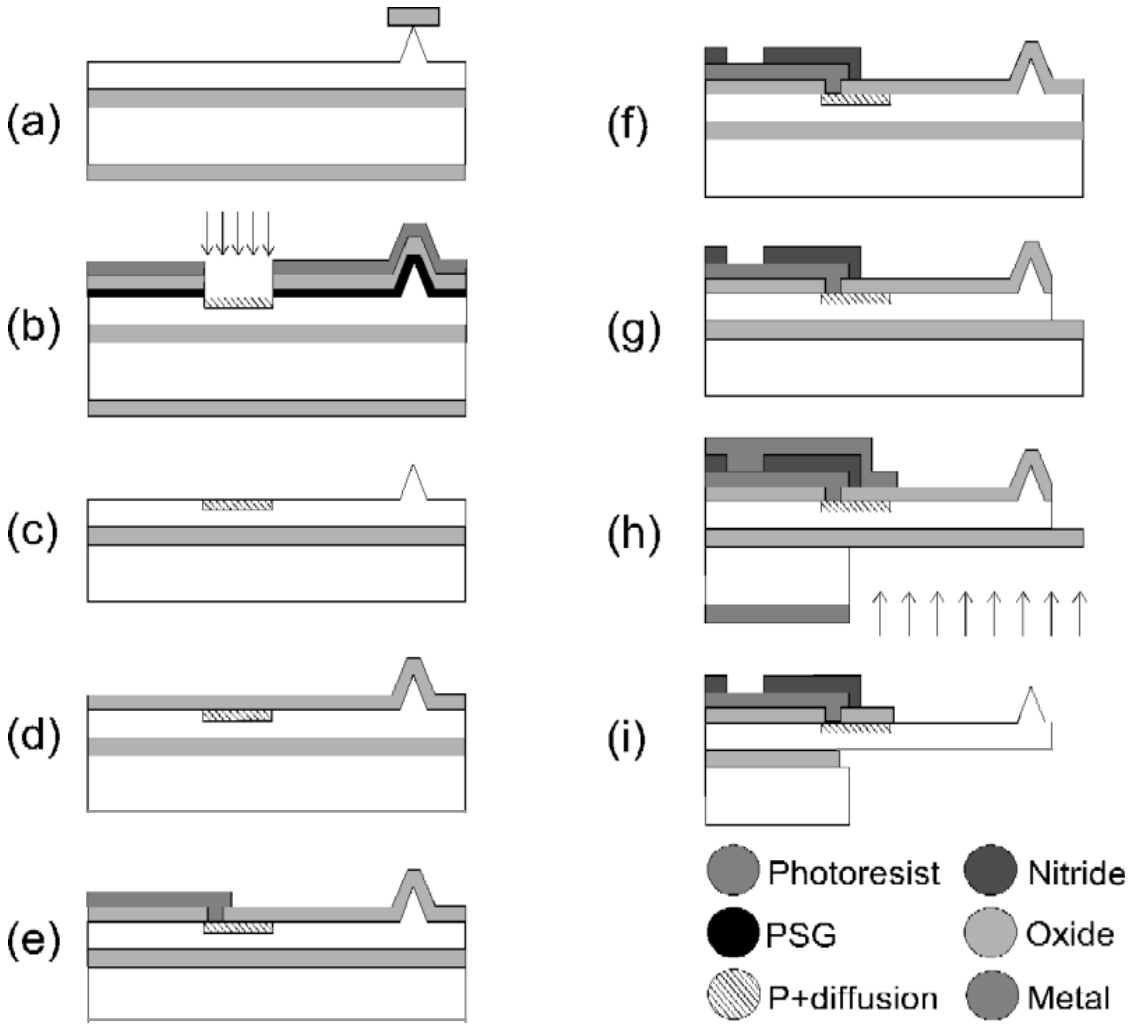

Figure 2-5
Process-flow chart of AFM chip:

a) Thermal oxide, lithography, oxide etching, KOH etching.
b) CVD PSG deposition, CVD oxide deposition, Lithography, Oxide etching, Implantation, removing resist, CVD oxide deposition, thermal treatment (950°C, 30 min.).
c) Oxide etching.
d) CVD oxide deposition.
e) Lithography, Contact hole opening, Al evaporation, Lithography, Al etching.
f) Plasma SiN deposition, Lithography, SiN Plasma etching.
g) Lithography, Oxide etching, Topside Si etching.
h) Front side lithography, backside lithography, backside DRIE etching.
i) Oxide etching.

2.3 AFM scanner design

2.3.1 Initial requirements

The key properties for the AFM scanner have to be, as for the silicon chip, small size, low power consumption and shock resistance. The instrument will measure airborne and soil particles with sizes up to 3 micrometers. Thus, the scanner will require an X-Y range of 30 to 40 μm to be able to image several particles on a single image or, in case of a low particle density on the substrate, to increase the chance of hitting a particle.
Since the exact chemical composition and surface properties of the particles are not known, their behaviour on the different substrates of the sample wheel of MECA might change. As the Martian atmosphere is very dry, the particles are unlikely to coagulate due to water molecules at their interface. However, dust particles might pile up on each other due to electrostatic charging. Therefore, the scanner will require a large stroke perpendicular to the sample plane to account for such 3 dimensional piles. If the stroke in Z-direction is too small, the scanner will not be able to keep a constant bending on the cantilever and the tip would be scraped over the particles. A minimum stroke of 10 μm has been specified as an initial requirement.
Earth-bound AFM designs commonly utilize piezo-ceramic actuators for scanning areas of several tens of micrometers. These piezo-ceramic tubes are rather bulky and brittle and necessitate driving voltages of over 100V to produce these large strokes. This type of actuation could therefore not be used to produce the specified scan size since voltages higher than 50V would ionise the Martian carbon dioxide atmosphere and create electrical discharge on the electronic circuits. A different technique based

on electromagnetic actuation has therefore been proposed by our project partner[1] to reduce the supply voltage to 12V. The assembly and testing and optimisation of the device have been performed at IMT.

2.3.2 Scanning technique

The FAMARS scanner is based on three electromagnetic actuators fixed on a platform in a triangular configuration. This platform, employed to move the sensor array in three dimensions, has been jointly developed with our project partner[1]. Each actuator consists of an electromagnetic coil and a leaf spring suspended permanent magnet. The coils are driven by current sources on the electronic board. Passing a current through a coil will attract or repel the magnet and move the platform around an axe defined by the 2 opposite coils. By supplying the correct currents to the coils, one can describe a motion in spherical coordinates at the AFM tip position. In a first approximation, by considering small displacements, the curved x-y-z motion produced by the platform is linear and orthogonal. Figure 2-6 shows a schematic of the scanning principle. Figure 2-7 a) shows the shape of the actuated platform and the leaf-spring suspension.

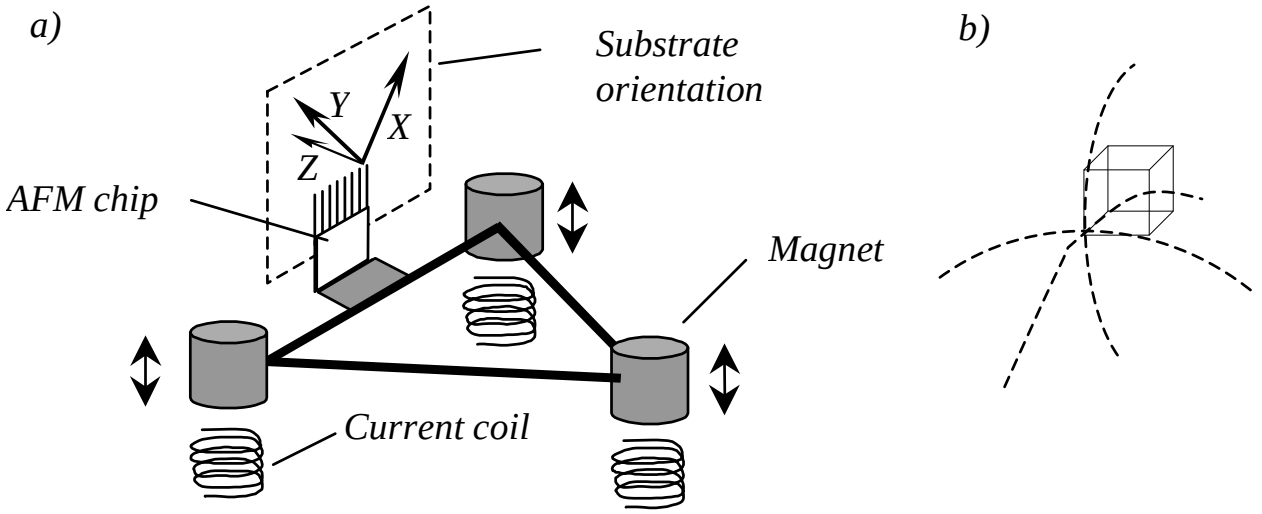

Figure 2-6

a) Schematic view of the scanning principle. 3 magnets are placed in a triangular configuration and attached to a spring-loaded platform. A coil is placed under each magnet to actuate the platform.

b) In a first approximation, by considering small displacements, the curved x-y-z motion produced by the platform at the AFM tip location is linear.

[1] Nanosurf AG, Liestal, Switzerland.

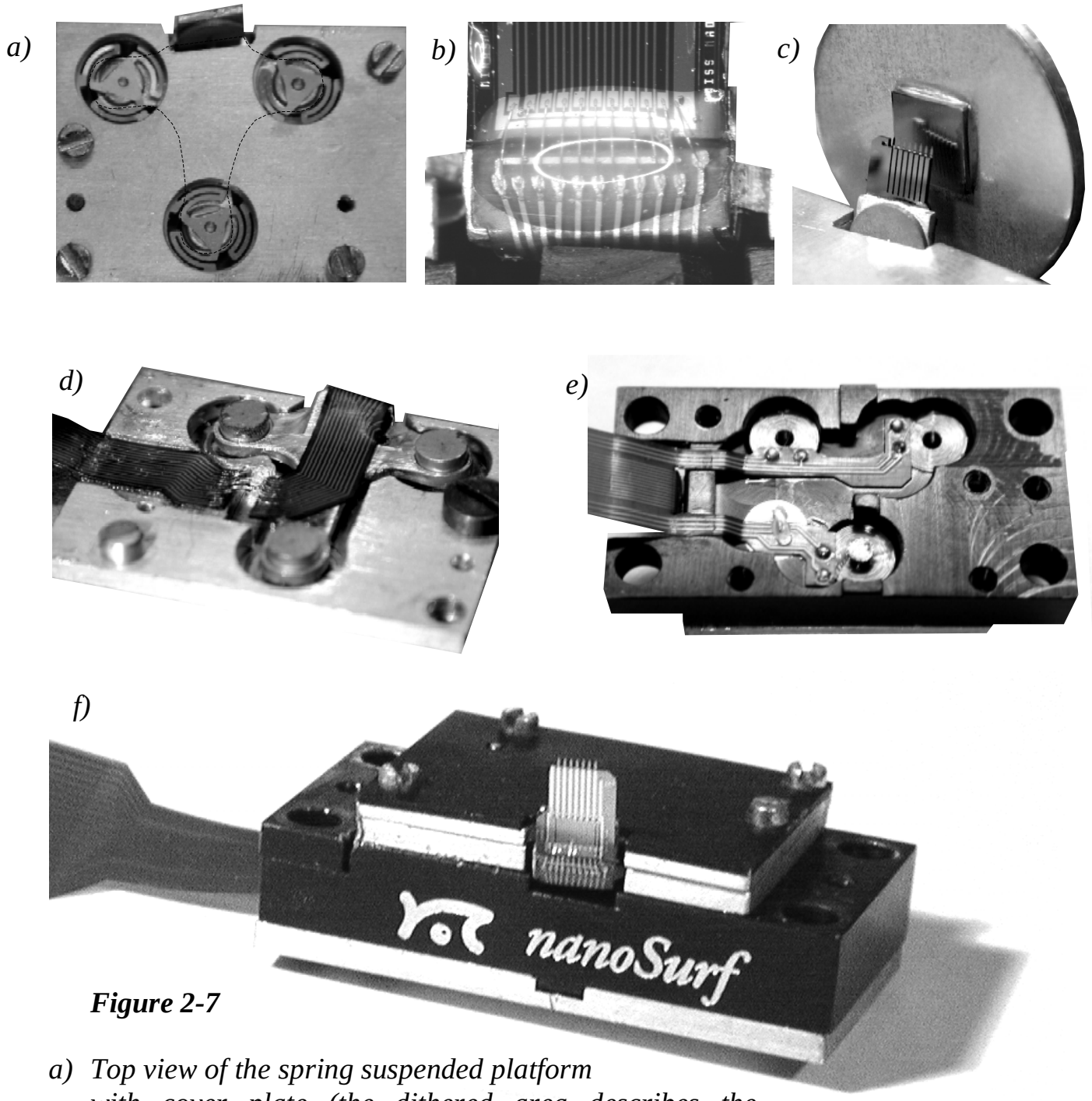

Figure 2-7

a) *Top view of the spring suspended platform with cover plate (the dithered area describes the platform shape under the cover plate). The tilt angle at the chip location is visible.*
b) *Encapsulated wire bonding between the kapton flex-print and the AFM chip.*
c) *Back view of the AFM chip mounted on the scanner. The piezo-electric disc for dynamic mode operation is placed behind the chip. The tilt angle relative to the substrate can be guessed by looking at the reflection of the chip in the sample.*
d) *Back view of the actuated platform. Ultra thin soldered wires bridge the gap between the flex-print and the leads on the actuated platform.*
e) *Back view of the scanner with flex-print connections to the coils and to ground the scanner box.*
f) *Front view of the scanner with mounted AFM chip.*

The AFM chip is glued vertically in front of the scanner with the AFM tips facing the substrate. It is mounted with two tilt angles relative to the substrate so that only the far right tip is in contact with the surface (see Figure 2-7 c). For vibrating the cantilevers in dynamic mode operation, a small piezo-electric disk has been mounted on the backside of the chip holder.

2.3.2.1 Damping of the platform

Passive damping is provided by a film of viscous grease[1] applied on the top of the leaf-springs. The grease had to fit certain criteria to be space compatible. In particular, outgassing factors had to be very low and the viscosity change with temperature had to be kept as small as possible.
The grease viscosity influences significantly the scanning behaviour of the AFM. If the viscosity is too high, the scanning speed needs to be decreased to prevent creep effects and distortion of the scan area. The feedback loop regulating the height of the cantilever is influenced by a too high viscosity as well.
If the viscosity is too low, the damping effect of the platform is reduced. Small vibrations detected by the AFM sensor will be fed back to the coil controlling the out-of-plane motion and will amplify the noise produced by the vibrations. Thus, the stability of the feedback loop for constant force measurements is disturbed.

2.3.3 Scanner assembly

Assembly of the scanner parts has been done in a clean environment to meet the planetary protection requirements specified in [10].
Connections from the electronic board to the AFM chip, the coils and the piezo-electric disk are provided by a capton flex-print. It is glued to the different aluminium layers constituting the scanner. To prevent stiffening of the suspended platform by the capton connections, the flex-print is cut at the interface and replaced by thin soldered wires (see Figure 2-7 d). Other electrical paths present on the flex-print are connected to the coils and the scanner box for grounding (Figure 2-7 e).
Before mounting the AFM chip, the scanner is connected to the electronics to check for orthogonal scanning movements. The platform movement is characterized under a microscope. Further testing of the scanning behaviour is described in §2.6.2.
Traditional wire bonding and encapsulation is used to connect the AFM chip to the flex-print (see Figure 2-7 b). The electrical connections to the AFM chip and the current coils were characterized with resistivity measurements. The scanner has an overall size of only 12mm x 18mm x 24mm and weights 15g. Figure 2-7 f) shows a front view of the scanner with mounted AFM chip.

[1] Apiezon N, Apiezon products M&I materials LTD, Manchester, UK.

2.4 AFM electronics

The electronics consist of distinctive modules to address the different functional tasks of the AFM. An amplifying circuit in a Wheatstone bridge configuration is used to measure the resistivity change of the piezoresistor integrated on the cantilever. A multiplexer is implemented on the electronic board to allow for switching from one cantilever to the next when performing a tip exchange. The design and fabrication of the electronics has been performed by our project partner[1]. Figure 2-8 shows the schematic of the circuit.
In static mode operation, the amplified deflection signal is converted to numeric information by means of an ADC circuit. It is used in the digital feedback circuit for constant force operation. In dynamic mode operation, a direct digital synthesizer (DDS) is used as a frequency generator to vibrate the cantilever. A phase locked loop circuit (PLL) is used to detect the resonance frequency of a cantilever [16].
The scanner motion is also digitally controlled in order to easily adjust the scan-size and orientation via simple numerical commands. Three DAC circuits convert the signals to drive the current sources for the scan-coils. Additionally to the scanning signals, the feedback signal is added on the coil that drives the Z direction of the scanner. Figure 2-9 illustrates the described modules.
All logic circuits are realized in two field programmable gate arrays (FPGA). The heart of the electronics is a dedicated microcomputer system. On power-up, the measurement software is automatically downloaded from the lander computer. All communication between the controller and the lander computer is done through a serial interface. This architecture simplifies interaction with the lander and assures a great autonomy of the AFM as the lander sends simple commands to request the AFM to take an image. The electronic circuit has a maximum power consumption of 3.3 watts.

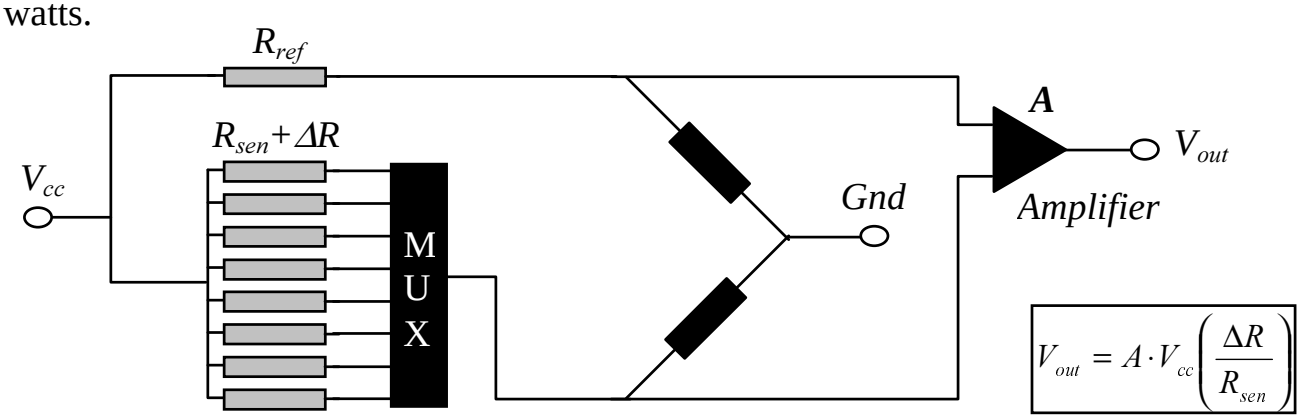

Figure 2-8

Wheatstone bridge circuit to convert the resistivity-change of the senor array into DC-voltage. The grey components are implemented on the AFM chip whereas the black components are implemented on the electronics.

[1] Electronics department, University of Basel, Switzerland.

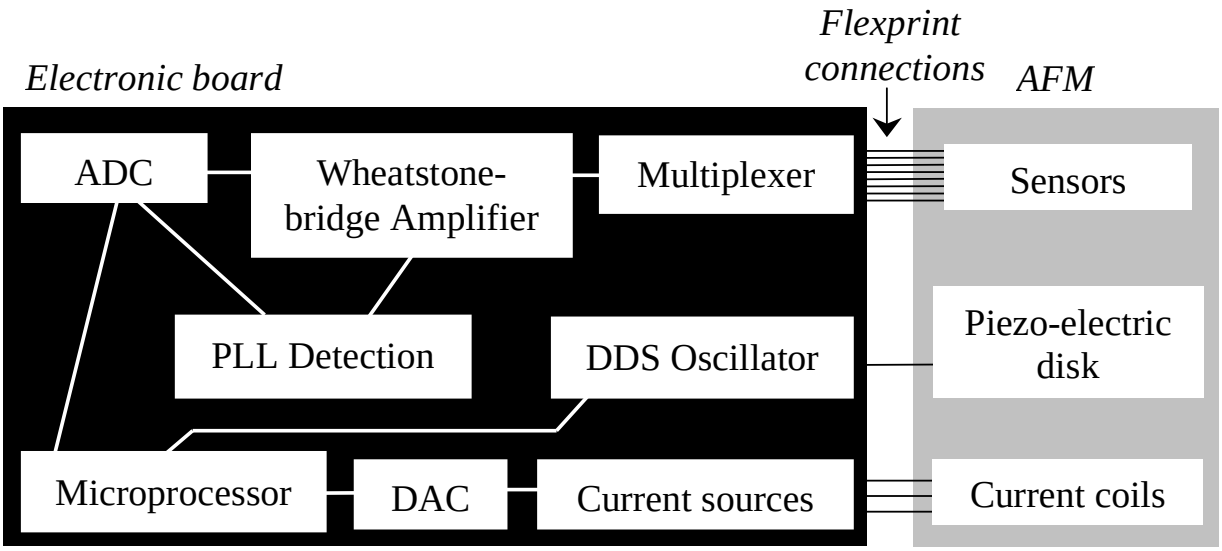

Figure 2-9
Schematic view of the electronic modules necessary to drive the AFM.

2.4.1 Single Event Upset (SEU) protection circuit

On Mars, the solar radiation and bombardment with heavy ions is much less shielded than on Earth, as no magnetic field is present to shield the planet's surface. Different damages can be induced by single event upsets (SEU). If a heavy ion hits a register cell, the stored information can be falsified. To secure the data, a triple voting circuit has been implemented. Each data bit is stored in 3 independent registers and checked by a voting cell. The output of the voting cell always reflects the majority of its inputs. All important register cells in the programmable logic chips are implemented in this way. With such a design rule the failure rate can be reduced by a factor of 1,000 to 10,000. Figure 2-10 a) illustrates the described protection circuit.

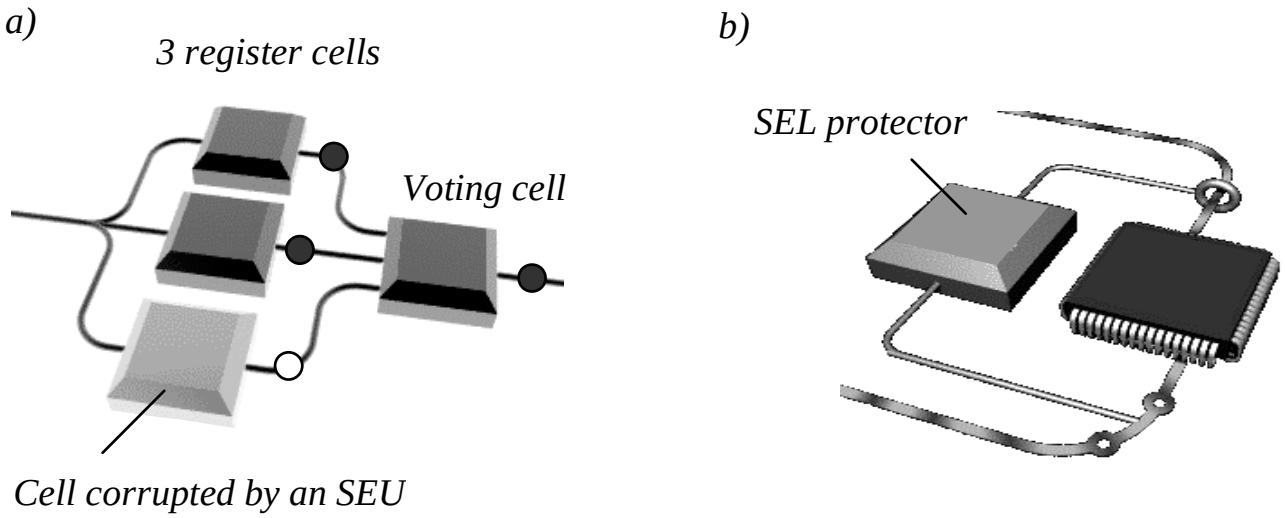

Figure 2-10
a) Principle of the SEU protection circuit.
b) Principle of the SEL protection circuit.

2.4.2 Single Event Latch-up (SEL) protection circuit

A more severe hardware failure called single event latch-up (SEL) can occur in certain CMOS chips. If a conducting path is opened between a power line and ground by a sudden ionisation due to heavy ion impact, a high current will flow through this path and destroy the CMOS chip by overheating. As not all electronic components are radiation hard, a protection circuit has been implemented to prevent these SEL from harming the electronic components. This module measures the current consumption on all power lines of the card, and immediately shuts down the power if a too high current surge is detected. A short time later, the power is switched on again and the board returns to its normal function after having again downloaded the microprocessor program. Figure 2-10 b) illustrates the described protection circuit.

2.5 AFM Software

The following operation concepts have been developed for the flight software that will be implemented on the lander computer. As the AFM electronics already has its own processor to drive the instrument, a higher communication level based on serial protocol will link the lander computer to the AFM. The command dictionary to drive the AFM can be found in [17]. The connection with the electronics of MECA limits itself to a single wire, which tells the sample wheel to stop its approach when the AFM is in contact.

2.5.1 Operation schemes

The command dictionary of the flight software for the AFM consists of block level and high level commands. Block level command will permit a flexible operation sequence by putting together operation blocks. These commands will be very useful when quick decisions need to be taken to react on the actual instrument status and the first measurements will be sent back during the mission. High-level commands consist mainly of a fixed sequence of block levels and will be implemented to permit a safer imaging and to increase the scientific relevance of the images.
Both types of commands use arguments and parameters to specify certain operational variables. Arguments are directly specified with the command itself for quick adjustment of frequently changing variables. Parameters are values considered to stay sufficiently constant to be stored in look-up tables. The following sections give an overview of the different types of block level commands and the high level command called AFM_Autoimage.

2.5.1.1 Block level commands

The block level commands comprehend basic initialising sequences and health checks for static and dynamic mode, which set up the instrument for an approach. Several images with different sizes can then be taken subsequently on the same substrate. Figure 2-11 illustrates the possible operation schemes using block level commands.

AFM_Boot:
This command downloads the software code for the AFM electronics. This is done every time the power of the AFM is switched on. It comprises parameters that specify the X, Y and Z offset relative to the center position of the scanner to eventually avoid a previously detected distorted scan area.

Stage_Move:
Not part of the AFM command dictionary but mentioned here for completeness. This command rotates the sample wheel to the selected substrate and moves it to a defined position relative to the AFM, i.e. to the focus position of the optical microscope. It has 3 arguments for substrate number, number of steps relative to the AFM and direction.

AFM_Test_Tips:
This health check performs an initialisation of the Wheatstone bridge (see § 2.4) for every piezoresistor and compares the returned voltages to nominal values stored in look-up tables. It then analyses the thermal drifts and noise-level of each sensor. A message characterizing the status of each sensor is then generated. It is then decided if the cantilever is ready to perform an approach and measure an image. If not, depending on the specified operation, either the AFM_break_tip command or the AFM_abort subroutine is executed.

AFM_Freq_Test:
This health check performs a dynamic initialisation of the current cantilever using specified values stored in look-up tables. It measures the cantilever's resonance frequency and amplitude. It then decides if the resonance amplitude is high enough to perform an approach and measure an image. Different messages will be generated that will describe the status of the current cantilever. If no dynamic mode imaging is possible due to a too low signal, it will either jump to the static mode initialisation or execute the AFM_abort sequence.

AFM_Approach:
This command approaches the stage to the AFM. The approach is stopped as soon as the active cantilever detects a deflection.
If, for non-deterministic reasons, the cantilever does not detect the approaching sample, the wheel needs to be stopped before crashing into the remaining tips of the AFM. Therefore, a maximum number of overshoot steps will be performed by the sample wheel. Since the distance between the optical microscope and the AFM tips is

constant, optical calibration based on the focus position of the optical microscope will be performed on earth to define the exact distance of each sample relative to the cantilevers. This optical focus position is also used as a starting point for the AFM approach since it is the closest distance to the AFM defined by a limit switch.

AFM_Image:
This command takes an AFM image. It is very flexible due to numerous arguments that can be specified:

- *Measurement mode:* static or dynamic
- *Scan range:* size of the image
- *Resolution:* number of pixels
- *Scan speed:* time for performing each scan line
- *P, I gain:* feedback parameters of the closed loop system
- *Setpoint:* specifies the force of the cantilever in static or the phase shift relative to the driving signal in dynamic mode operation
- *Samplemask:* specifies the number of channels that will be measured
- *Fwdbk:* specifies which scan direction should be recorded (forward, backward or both)
- *Compression:* specifies an image compression factor for all returned images

AFM_Abort:
This sub-routine aborts AFM operations in case of a failure mode. To be able to leave the AFM in a safe position after this command, it performs a check of the stage position and moves the stage to safe position for rotations of the sample wheel.

AFM_End:
This command ends AFM operations after a successful block sequence. It retracts the scanner before moving the stage to its safe to rotate position.

AFM_Break_Tip:
This command will break a cantilever specified as argument by accurately positioning and approaching the cleaving tool of the sample wheel.

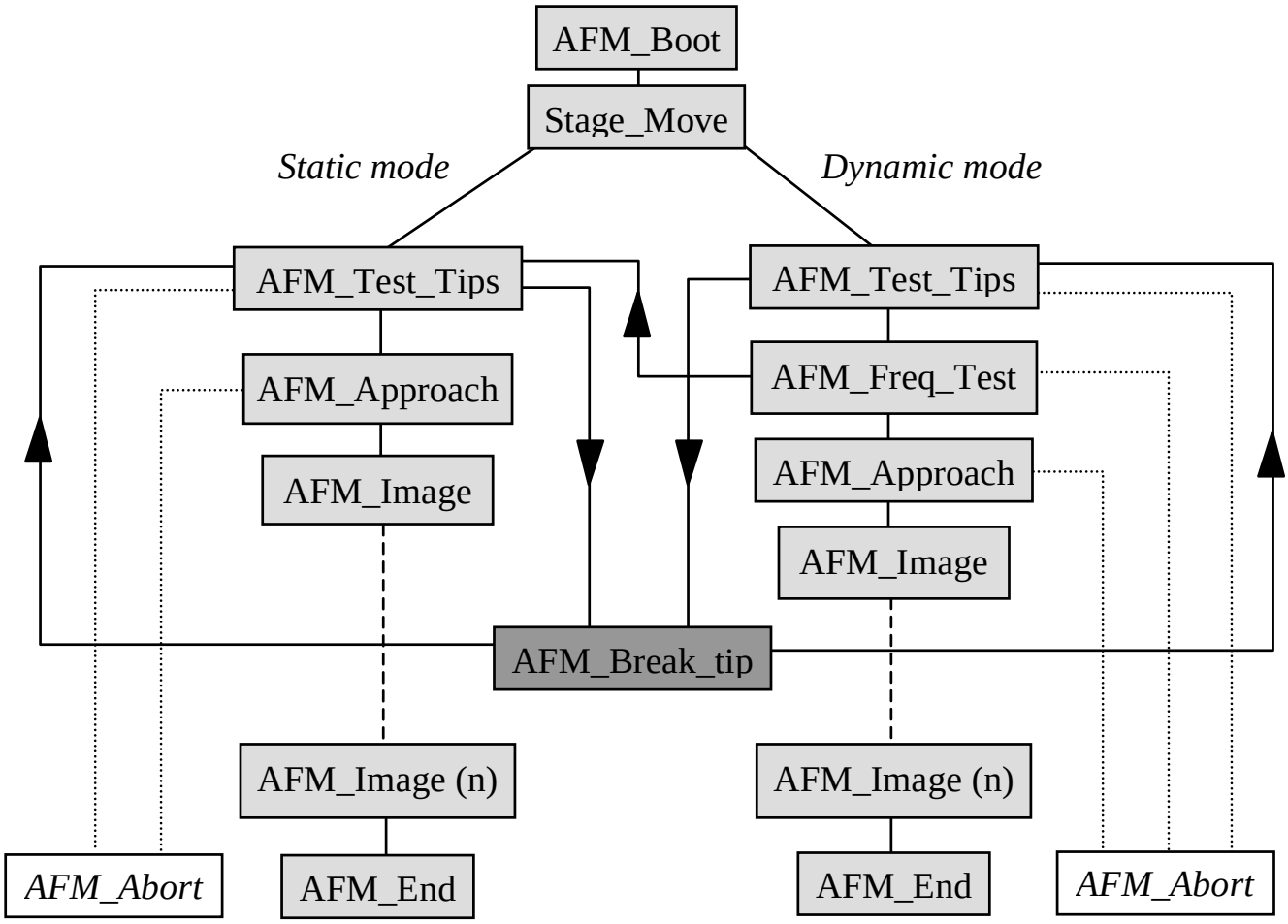

Figure 2-11
Arrangements of block level commands and possible recovery (dark grey) and failure modes (white squares).

2.5.1.2 High level command: AFM_Autoimage

To be able to execute the high level command AFM_Autoimage, only 2 block level commands need to be used (see Figure 2-12). It can be executed several times and generate a set of 4 subsequent images on the same substrate at each time. It is composed of several subroutines that will ensure safe imaging and increase the scientific relevance of the AFM measurements. The following paragraphs describe each subroutine in detail. Figure 2-13 shows the operation scheme of AFM_Autoimage.

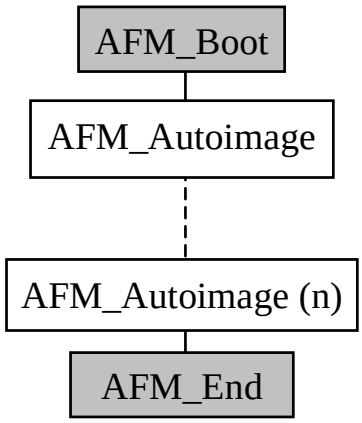

Figure 2-12
Arrangement of block level commands with the high level command AFM_Autoimage.

AFM_Health:
This subroutine is a combination of the 2 block level commands AFM_Test_tips and AFM_Freq_test (see 2.5.1.1). Several parameters stored in tables specify the settings to be used for static and dynamic health checks. These values have been determined under Mars equivalent conditions on Earth. A message characterizing the status of each sensor is then generated. Different operation modes are possible depending on the status of the AFM. As dynamic mode measurements are preferable for most measurements, the argument *Mode* will insure that the best possible mode is chosen:

- *Mode* = static: the subroutine Stat_Init will be executed and measurement will be done in static mode. If the status of the AFM doesn't allow this type of measurement, it will abort AFM operation.
- *Mode* = dynamic: the subroutine Dyn_Init will be executed and measurement will be done in dynamic mode. If the status of the AFM doesn't allow this type of measurement, it will abort AFM operations.
- *Mode* = Autochoose: If dynamic mode measurement is possible, it will execute the subroutine Dyn_Init and measure the following image in dynamic mode. If dynamic mode measurement is not possible but static mode is, it will execute the subroutine stat_Init and measure the following images in static mode. IF static mode is not possible, it will execute abort AFM operations.

Stat_Init:
This command follows the sub routine AFM_HEALTH and overwrites the dynamic initialisation if no dynamic measurements are possible. Other settings that depend on the size of the image will be set later in the subroutine AFM_IMAGE.

Dyn_Init:
This command follows the sub routine AFM_HEALTH, which has already initialised the AFM tip for dynamic mode. Other settings that depend on the size of the image will be set later in the subroutine AFM_IMAGE.

AFM_Approach:
This command approaches the stage to the AFM. The approach is stopped as soon as the active cantilever detects a deflection. It is based on the same algorithm as the block level command described under § 2.5.1.1.

AFM_Prescan:
This subroutine sets the optimum scan parameter for measuring the first image. First, it determines the maximum scan range that the scanner is able to perform on a substrate within its dynamic Z range. This value will never exceed the value of the argument *Maxrange*. As the topography of the sample is not known, this will prevent the tip from crashing into particles when scanning an area with a larger Z range than

the scanner can produce. To do so, the scanner performs a cross (2 scan lines with 90 rotation centered in the middle of the Image). It starts with a cross size of 3um and doubles its dimensions until the height of the cross reaches half of the maximum dynamic Z range (maximum XY range: 53 µm, maximum Z range: 14 µm). As this cross does not describe the complete topography of the sample, this insures some threshold to anticipate the height of the un-scanned regions.
It also determines the substrate orientation relative to the X-Y plane defined by the scanner and corrects the slopes in both directions. The argument *Prescan_Flag*, specifies if this subroutine will be executed or not. If it is not executed, the argument *Maxrange* specifies the scan size of the first image.

AFM_Image:
This subroutine generates an image every time it is executed. An internal counter keeps track of the number of times (up to 4) this command is executed (See Figure 2-13).
The scan range for the first image is either determined by the subroutine AFM_Prescan or, if not executed, by the argument *Maxrange.* The sizes of the following images will be determined by the subroutine AFM_Autozoom.
The following arguments describe how the image data can be processed:

- *Samplemask (0-3)* specifies the number of channels to be measured and is specified separately for each subsequent image. 2 channels can be recorded: the lever signal (error signal remaining with closed feedback loop), and the Z feedback signal (height information).
- *Compress (0-3)* specifies the compression ratio for each image.
- *FwdBk* specifies which scan direction should be recorded. (Forward, Backward, or Forward and backward).

Several parameters stored in tables specify the image and measurement settings like the number of pixels in X and Y (resolution), setpoint values for static and dynamic mode, scanning times as well as feedback loop setting. These values strongly depend on the image size, as larger images will require slower scanning speeds and more sensitive feedback loop settings. These values have been determined under Mars equivalent conditions on Earth.

AFM_Autozoom:
If the argument *Smartzoom_Flag* is set to 1, this subroutine will analyse the information of the previously measured image by using the JPEG compression algorithm implemented on the lander computer. It will then choose the least compressible sub-area as target for the next image by adjusting the parameters *Xoffset* and *YOffset* of the scanner and calculate the size of the subsequent image by using the argument *Nestratio*. For example, a *maxrange* value of 48 µm and a *Nestratio* value of 4 will generate a set of 4 images with the following dimensions: 48µm, 12µm, 3

µm and 750 nm Executing this subroutine will prevent zooming into a sub-area with no information.
If the argument *Smartzoom_Flag* is set to 0, subsequent images will simply be generated by zooming in the center of the previous image.

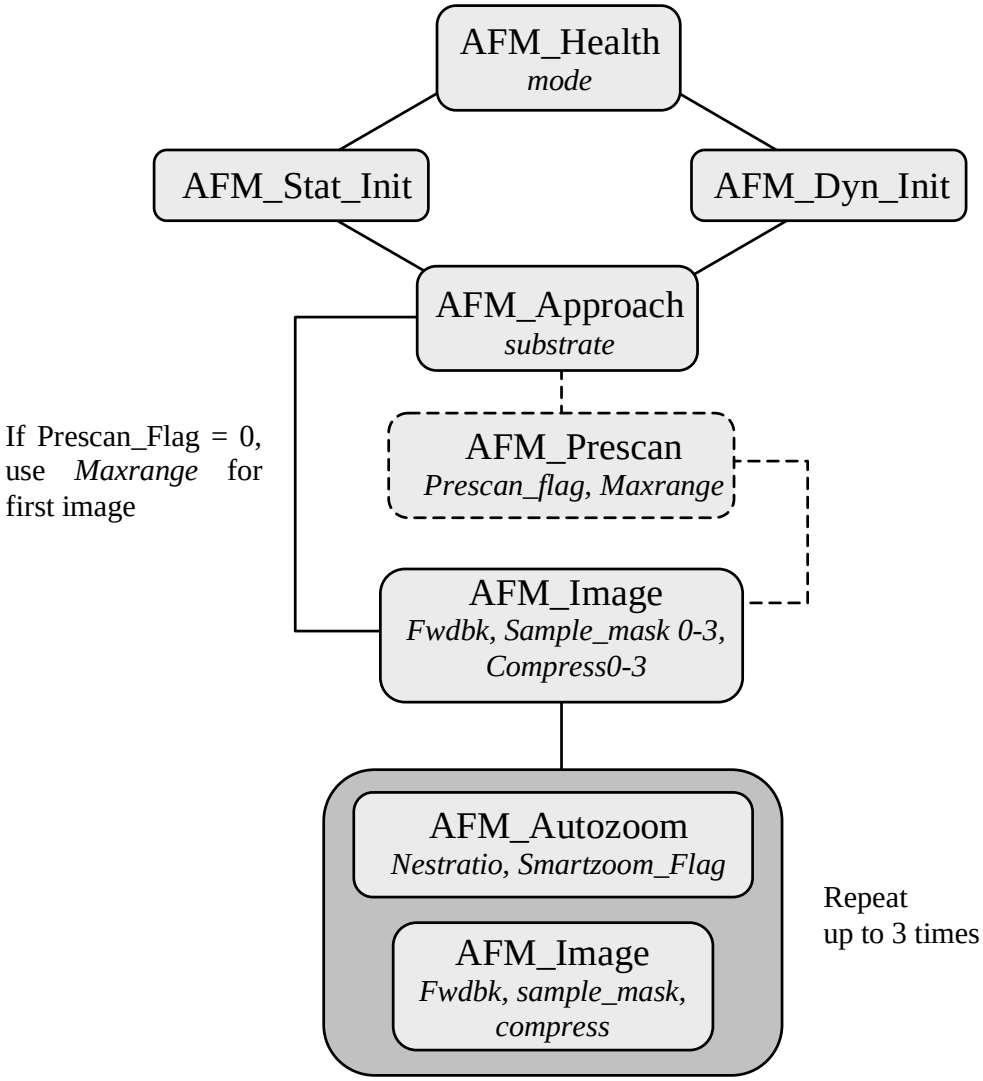

Figure 2-13
Subroutines of the high level command AFM_Autoimage.

2.5.2 Flight software development

The routines for autonomous operation described in this section have not been programmed to this date. Due to the cancellation of the 2001 opportunity for MECA, software developments were stopped before completion. Thus, most of these sequences have not been tested in practice.

2.6 Instrument characterization

2.6.1 Chip characterization

Optical microscopy and scanning electron microscopy (SEM) is used to characterize the different fabrication steps of the silicon chips.
Basic electrical test with a prober were performed before mounting the chip on the scanner to assure the functionality of all piezo-resistors. The sensitivity of each sensor was determined by measuring the resistance change while actuating the cantilevers with a bimorph piezo-electric element with known amplitude.
Both tips (silicon and diamond) present on the chip can present knife-edges at their apex [18]. Since this will deteriorate the image quality and resolution due to tip convolution, individual selection of the best AFM chips for the flight models were required. The diamond tip selection was done before gluing them onto the cantilevers. The chips with the silicon tips already present were selected before mounting them onto the scanner. Both tip inspections (silicon and diamond) were done by scanning electron microscopy (SEM).
Due to the dynamic behaviour of the cantilevers is dynamic mode to be described in § 2.6.1.2, a second generation of AFM chips had to be designed and fabricated. Table 2-1 shows the physical characteristics of the first and second generation AFM chips.

Table 2-1
Physical dimensions and characteristics of the AFM chip.

			Cantilever dimensions (L x W x T)	Resonance frequencies	Force constant *
1st generation		Odd levers	610 x 160 x 9 μm	33.4 KHz	21.7 N/m
		Even levers	580 x 160 x 9 μm	36.9 KHz	25.5 N/m
2nd generation	1	Beam: 2625 μm	568 x 160 x 10 μm	42.7 KHz	36.8 N/m
	2	Beam: 2592 μm	603 x 160 x 10 μm	37.9 KHz	30.8 N/m
	3	Beam: 2618 μm	575 x 160 x 10 μm	41.8 KHz	35.7 N/m
	4	Beam: 2580 μm	613 x 160 x 10 μm	36.7 KHz	31.6 N/m
	5	Beam: 2509 μm	584 x 160 x 10 μm	40.4 KHz	33.9 N/m
	6	Beam: 2569 μm	624 x 160 x 10 μm	35.4 KHz	27.8 N/m
	7	Beam: 2599 μm	594x 160 x 10 μm	39.1 KHz	32.3 N/m
	8	Beam: 2560 μm	633 x 160 x 10 μm	34.4 KHz	26.6 N/m

Height spacing between tips when mounted at 10 ° tilt angle on the scanner: 60 µm
Cantilever thickness: 8-12 µm
Height of silicon tips: 9-13 µm
Height of diamond tips: 15 µm
Lateral spacing between tips: 350 µm
Gap between support beams: 90 µm
Chip size (L x W x T): 6.5 x 4.5 x 0.4 mm
Resistor resistivity: 2.0 kΩ
Resistor sensitivity to vertical bending: ~2Ω/µm

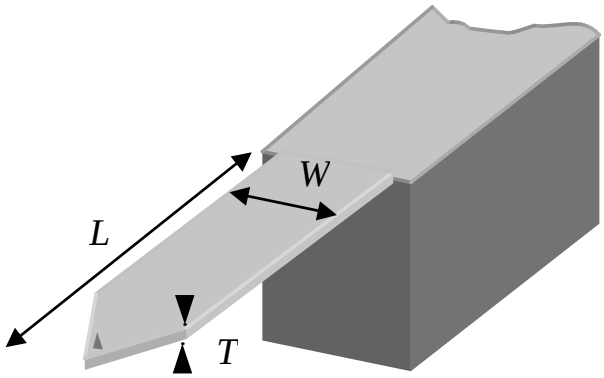

* $$C = \frac{E}{4}\frac{W \cdot T^3}{L^3}$$ [19]

E: modulus of elasticity (for silicon: 1.69 *10^{11} N/m^2)

2.6.1.1 Tip exchange

An important feature of the AFM chip design is the ability to change the tip and cantilever that is located on the far right of the array (seen from behind). Since the chip is mounted with 2 tilt angles of 10° relative to the sample surface (see § 2.3.2), this sensor (cantilever + tip) will always be the closest to the sample. By removing it, the following sensor will become the closest. This is guaranteed by the thick beams that support each cantilever. Their role is to provide a cleaving edge precisely located at the beam attachment with the rest of the chip (see Figure 2-14). This insures that the tip is still the closest point to the surface, even when using the last sensor of the array. The following reasons can be evocated for an exchange related to a tip or cantilever failure:

- One or several cantilever might have been physically damaged or broken during the launch, cruise and landing sequences. As the first cantilevers will be in the field of view of the optical microscope, their shape will be characterized optically. To be able to perform valuable measurements, the damaged cantilever(s) located on the right side of the first intact cantilevers would have to be removed.
- The electrical contacts to the piezoresistor might be damaged due to electrical discharge, preventing correct sensing of the stress induced by the bending of the cantilever.
- Due to higher hardness of surface features relative to the tip hardness, the tip apex might be worn due to frequent scanning, altering the quality of the image by tip convolution.
- To be able to characterize the same topography with 2 different tips (silicon and diamond), a cantilever exchange is necessary.

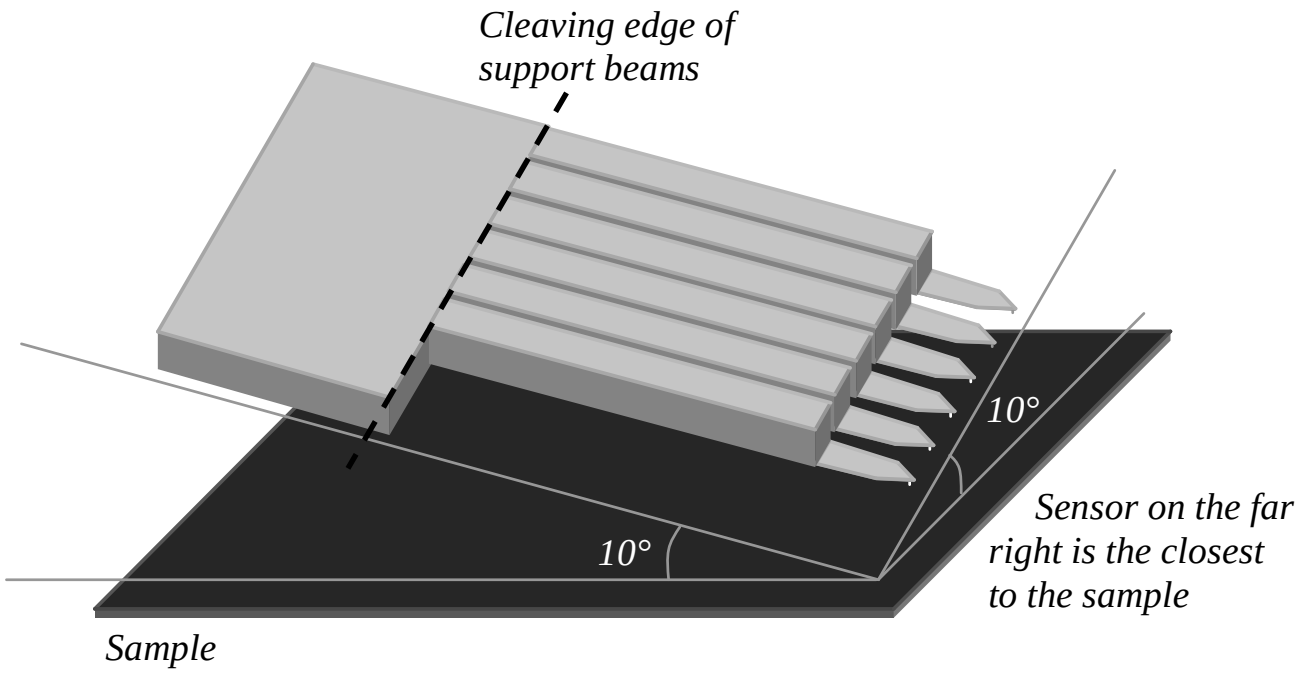

Figure 2-14
Schematic of the position of the sensor array relative to the sample. Two support beams have been removed.

To break the support beams, a protruding edge is used. It is pushed against the tip, cantilever and support beam from the substrate side. As this edge will have free space on its left side (seen from the back of the chip), it will enable the removal of a single beam without harming the other cantilevers. In flight configuration, the cleaving tool is mounted on one of the substrate locations on the sample wheel.
The testing of the cantilever exchange has been performed using the approach stage shown in Figure 2-21,and a polished wafer edge as cleaving tool.
At the beginning of the cantilever exchange procedure, the cleaving edge bends the soft cantilever and rips it off once it has touched the beam-cantilever interface (see Figure 2-15 b). As the AFM chip is fixed on the spring-suspended platform, the whole chip is then pushed back by about 100 micrometer until the platform hits the solid scanner enclosing. If the approach stage continues to push against the support beam, it will break it after an additional displacement of a few tens of micrometers.
As no constraint acts on the platform anymore, it returns to its equilibrium position. If this returning back is straight, the remaining cantilevers will not be broken by the cleaving too (see Figure 2-15 c, d, and e). Figure 2-16 shows an SEM image of the cleaving edge produced by the broken beams.

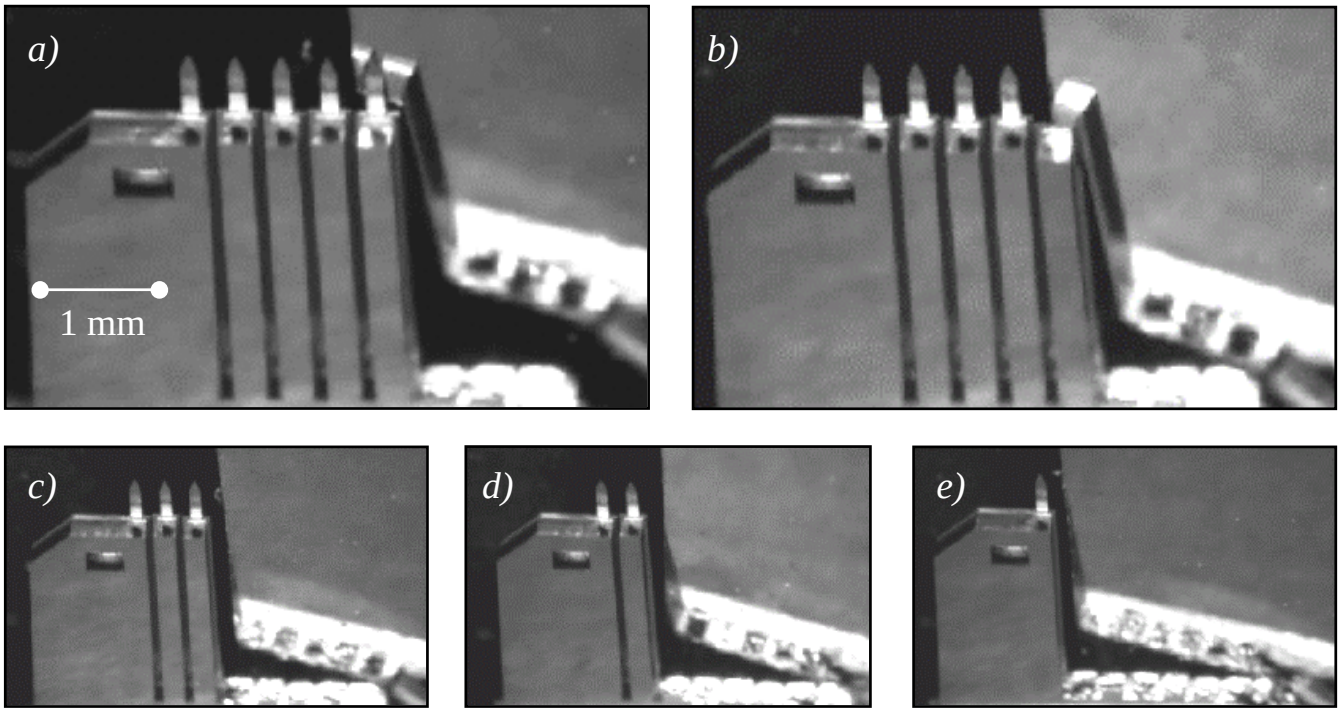

Figure 2-15

Chronological pictures of cantilever exchange procedure repeated for cantilever number 4 (figure a and b), 5 (figure c), 6 (figure d) and 7 (figure e). The reflection of the support beam in the cleaving edge is visible in figures a) and b).

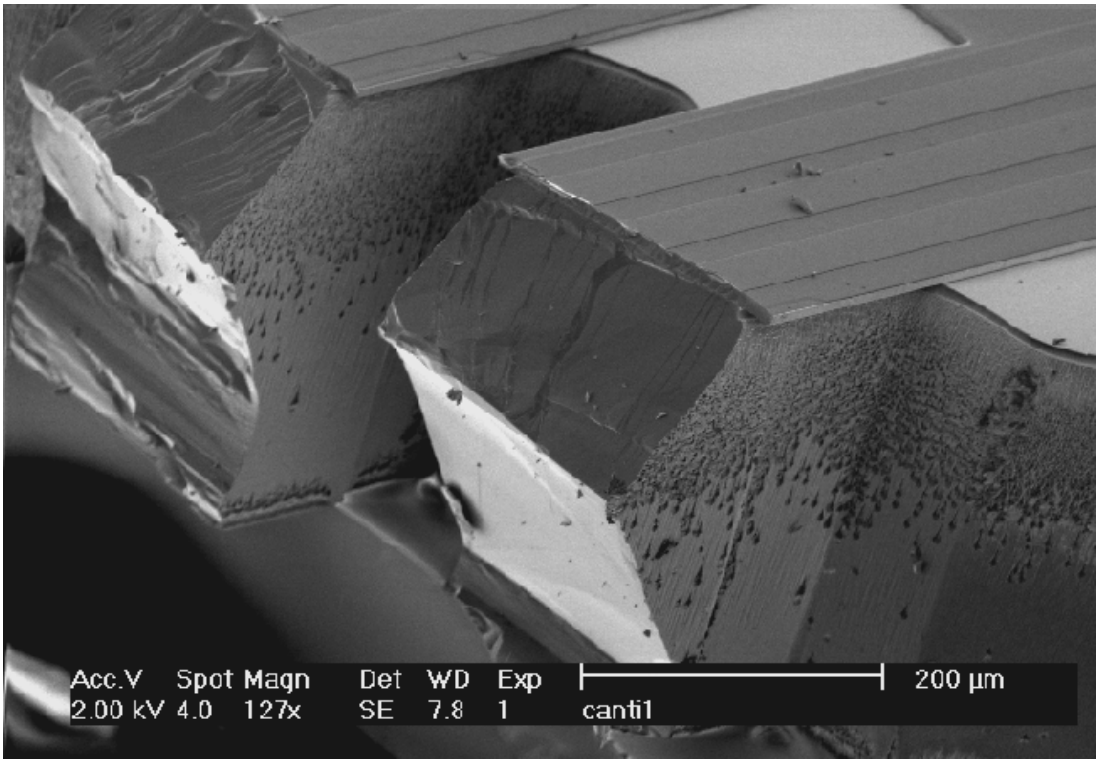

Figure 2-16

SEM image of the cleaving edge produced by the broken support beams.

2.6.1.2 Dynamic behaviour of the AFM cantilevers

AFM measurements in dynamic mode require an excitation of the resonance frequency of the cantilevers. As no individual actuation of the cantilevers is implemented, the whole silicon chip is vibrated to excite the individual resonance frequencies using a small piezo-electric disk mounted on the back of the AFM chip (see Figure 2-7 c).
The individual resonance modes of the AFM chip propagate the vibration produced by the piezoelectric disk. These vibrations are carried through the bulk and the support beams to end up at the cantilever location.
If the correct frequency is chosen, the target cantilever will vibrate at high amplitude due to its resonance state. This amplitude peak will produce other propagation modes across the chip that will be detected by the piezoresistors of the other cantilevers. This phenomenon is generally known as cross talk. Figure 2-17 shows the amplitude and phase response of the first cantilever influenced by the cross talk of the other cantilevers.
In a first generation chip design, as significant cross talk was expected only between neighbouring cantilevers, therefore, two different cantilever dimensions were implemented alternately on the chip (see Table 2-1). The resonance-peak separation between the odd and even cantilevers was 6 KHz. However, the resonance frequencies among the odd and even numbered cantilevers respectively were very close to each other (within a frequency range of 200 Hz).

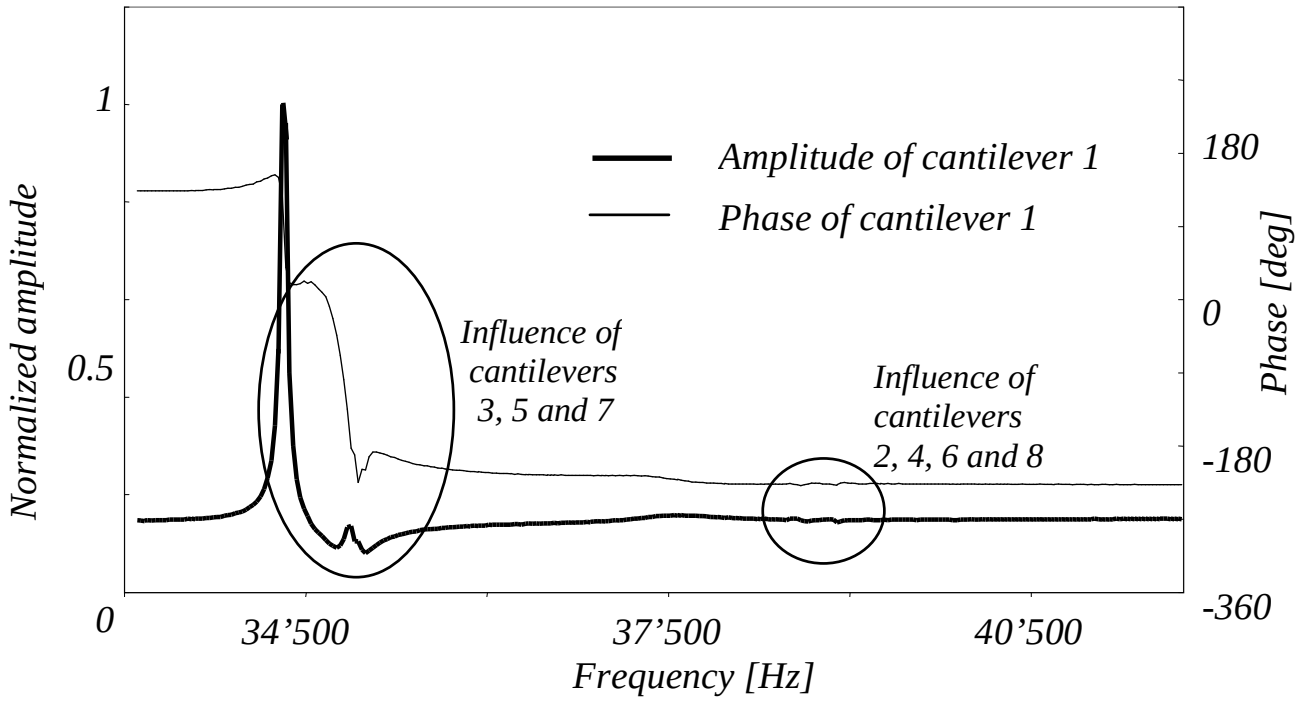

Figure 2-17
Amplitude and phase response of the first cantilever. The main peak and phase shift is produced by its own resonance frequency whereas the other peaks and phase shifts are produced by cross-talk coming from the other cantilevers.

A resonance peak of a cantilever produces a phase shift between the excitation signal and the signal detected on the piezoresistors. This phase shift is used by the AFM electronics to detect the resonance peak of the cantilever and to close its phase locked loop (PLL) regulation during measurements [16]. The phase value of this shift is a parameter that needs to be specified in 20-degrees steps so that the electronics can detect the amplitude peak.

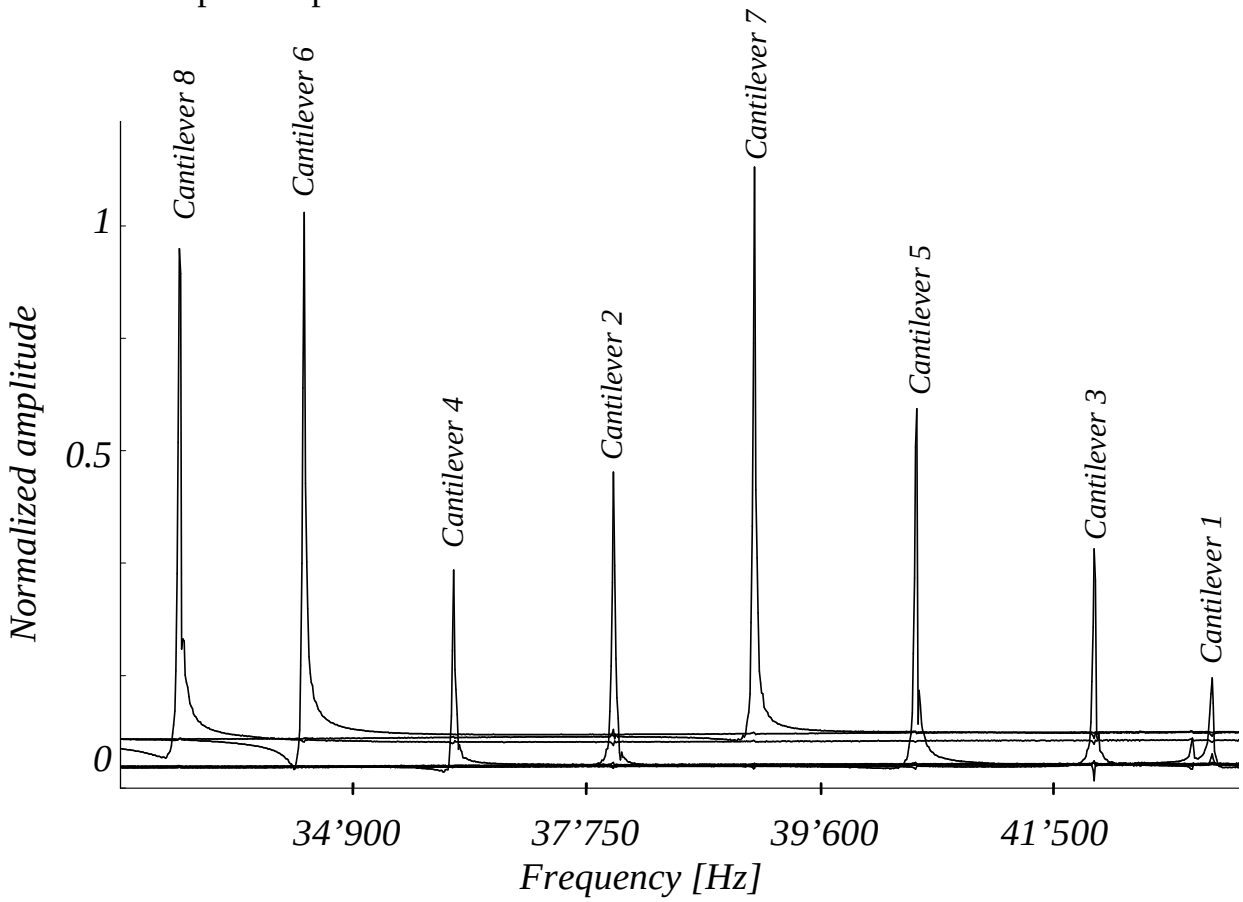

Figure 2-18
Amplitude response of all cantilevers of the 2nd generation AFM chip.

A characterisation of the dynamic behaviour of each cantilever is necessary to be able to perform autonomous initialisation of the instrument on Mars. The described cross-talk between cantilevers is of concern since it is not deterministic and the values of the phase shifts can vary for the following reasons:

- Pressure: Experiments in vacuum showed that the amount of cross talk is influenced by pressure, i.e. that the contribution of the neighbouring cantilevers to the amplitude and phase response of the measuring cantilever is less significant when the pressure decreases.
- Cantilever exchange: When breaking a specific cantilever, the amplitude and phase response of the remaining cantilever change, as the removed cantilever does not influence the cross-talk pattern anymore.

Calibration of the dynamic behaviour at Mars pressure was performed to determine the correct parameters for dynamic mode initialisation. Unfortunately, the second reason that influences the cross talk, i.e. cantilever exchange, could not be done for obvious reasons.
A second-generation AFM chip was designed to reduce the effect of cross talk. Based on the results of finite element simulation described in the following paragraph, the cantilever length for each sensor was modified. Thus, the resonance frequencies were separated by about 1 KHz (see Table 2-1). In addition, instead of just prolonging the cantilevers, the support-beam length was adapted for each cantilever to keep a constant beam-cantilever length. By doing so, the symmetry of the AFM chip was disturbed and the propagation of the cantilever resonance could be reduced significantly (see Figure 2-18).

2.6.1.3 Finite element simulation of dynamic behaviour

The encountered problems when operating the AFM chip in dynamic mode described in the previous section led to the conclusion that the chip architecture had to be modified. Finite element simulation of the vibration modes and the frequency response of the cantilevers were performed using ANSYS to optimise the dimensions of the second generation AFM chip. The alternative architectures had to be compatible with the cantilever-exchange procedure: the support beams required to keep the far right tip in contact with the surface had to be present and easily breakable by the cleaving tool.

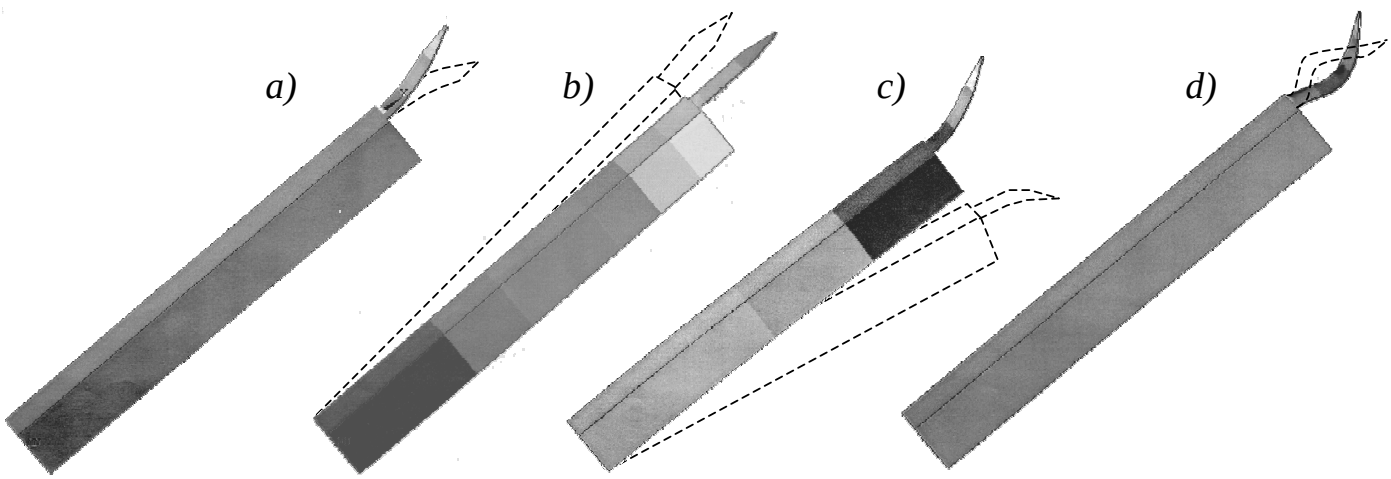

Figure 2-19
Modal analysis of the support beam-cantilever system:
Figure a) shows the first out of plane mode of the cantilever (33.7 KHz).
Figure b) shows the first transverse mode of the support beam (51.1 KHz).
Figure c) shows the first out of plane mode of the support beam (60.2 KHz).
Figure d) shows the second out of plane mode of the cantilever (192.2 KHz).

In a first step, a modal analysis of a single support beam with cantilever was performed. As the beam will propagate the vibrations produced by the piezoelectric disk mounted on the back of the chip, its first-mode resonance frequencies will have to differ from the resonance frequency of the cantilever to avoid cross-talk between the two elements (see Figure 2-19). The dimensions of the first generation support beam were already optimised in that sense. Its first mode resonance frequencies were about 20 KHz higher than that of the cantilever.
In a second step, the cross-talk behaviour of the whole chip was simulated. The experimental behaviour described previously could be reproduced by the spectral response of the cantilevers. New chip architectures were simulated to analyse the effect on the amount of cross talk. Symmetries produced by support beams with equal length (Figure 2-20 a) and direct attachment of the cantilevers to a block (Figure 2-20b) showed that the cross talk is increased.
On the other hand, different beam lengths for each sensor (Figure 2-20 c) showed a smaller cross talk. An alternative design using a stabilisation layer across the support beams was simulated as well (Figure 2-20 d). This membrane having the same thickness as the cantilevers could be easily fabricated during the shaping process of the cantilevers.
Both alternatives tended to reduce the cross talk and improve the dynamic behaviour of the chip. Finally, the architecture based on 8 different support beam lengths combined with 8 different cantilever lengths (not shown here) was chosen for the second-generation AFM chip (see Table 2-1).

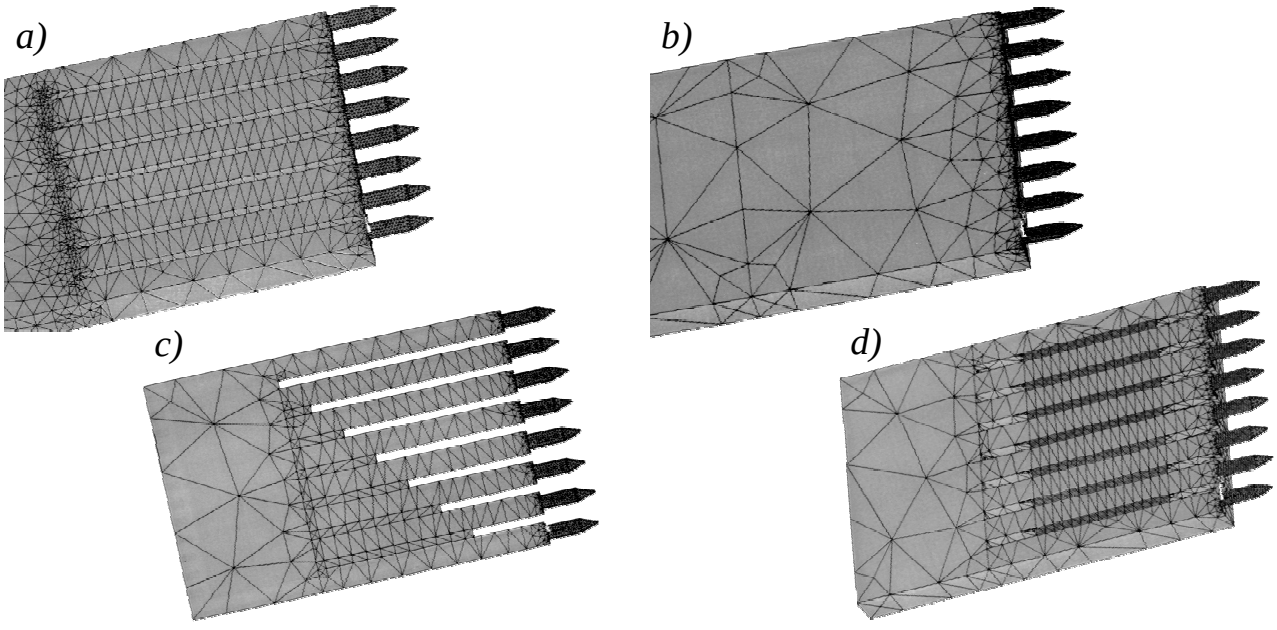

Figure 2-20
Meshed view of simulated AFM chip architectures:
a) First generation design with constant beam length.
b) Solid block with attached cantilevers.
c) Distributed support beam length still enabling cantilever exchange.
d) Cross-fixation across the support beams having the cantilever thickness.

2.6.2 Scanner characterization

The scanner has an overall size of 12mm x 18 mm x 24 mm and weights 15 g. Once the AFM sensor array is mounted and bonded on the scanner, a more accurate characterisation of the scanning motion can be performed by recording the first AFM images. The measurements are performed with a setup close to flight configuration. However, the sample wheel used to deliver the dust particles in front of the AFM on Mars was not available. An approach stage driven by a stepper motor is used to bring the samples in contact with the AFM tip (see Figure 2-21).
Images are recorded using dedicated software derived from a commercial version. The modifications allow to address each cantilever and to tune it individually for dynamic mode operation. The approach can be performed autonomously since the stepper motor is driven by the AFM software.

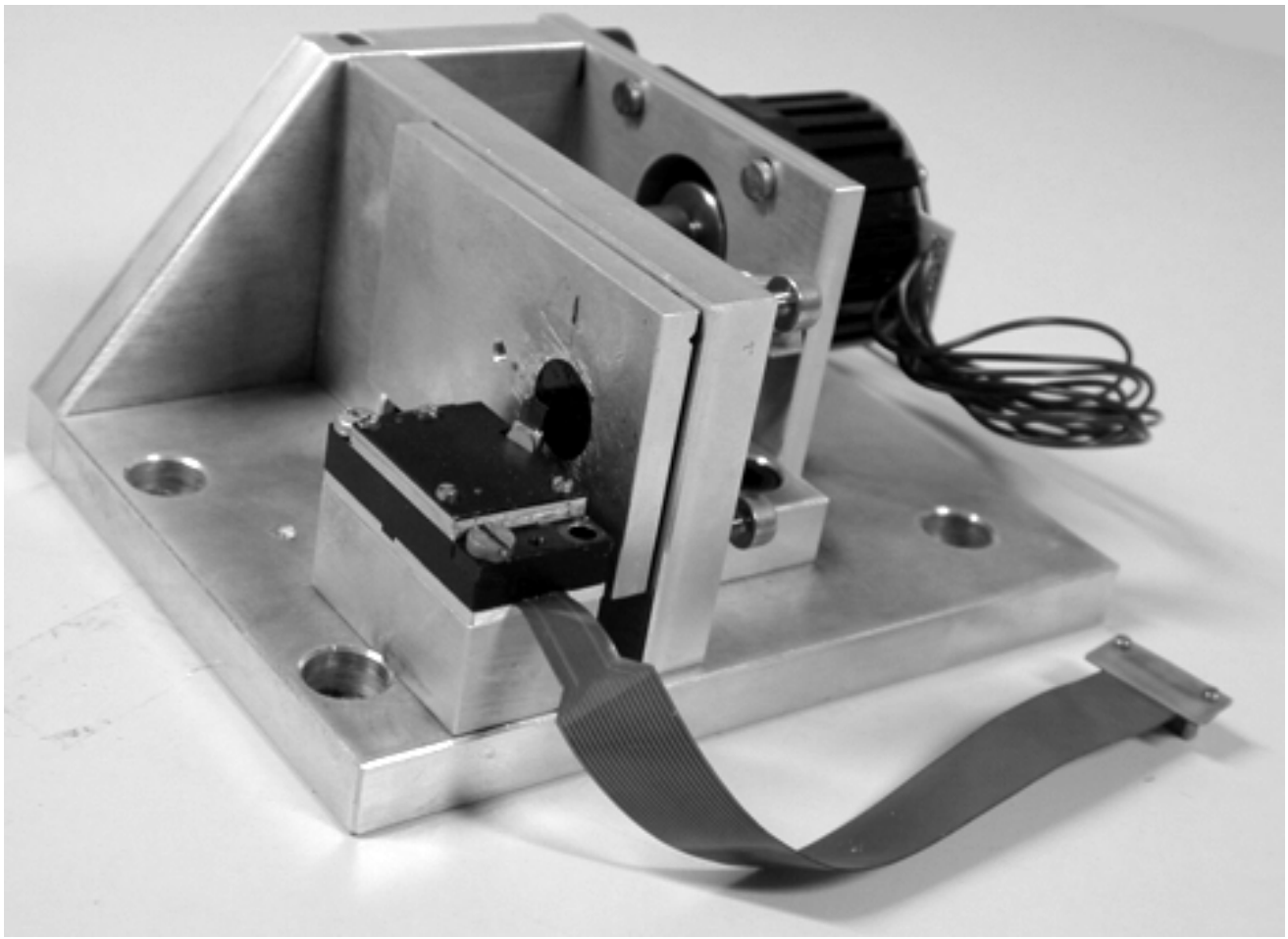

Figure 2-21
Approach stage driven by a stepper motor. The sample platform is suspended on three points to allow the surface to be brought into contact with the AFM tip.

2.6.2.1 Scanner stroke and orthogonality

An important characteristic of the scanner is the maximum area it can scan. It can be evaluated by measuring an orthogonal grid with known height and period. The calibration sample used to characterize the scanner has a step height of 200 nm and a pitch of 10 µm. Several parameters concerning the orthogonality and the orientation of the scanning field produced by the scanner relative to the surface can be adjusted by the software. A maximum area of 53 µm laterally and 14 µm could be produced.
Due to the applied scanning principle, the produced scanning field is never perfectly planar but describe a "saddle" like shape occupying a maximum height of 1.7µm when scanning the maximum X,Y dimensions (see Figure 2-26 a1). This inherent distortion can be corrected by using a planar fit algorithm, which applies a first order slope correction to each scan line. Figure 2-22 a2) shows a top view of the flattened image. By reducing the currents fed through the coils, the scan area can be reduced substantially while keeping the same accuracy. This enables to zoom-in into a sub-area. Figure 2-22 b) shows a sub-area of figure a).

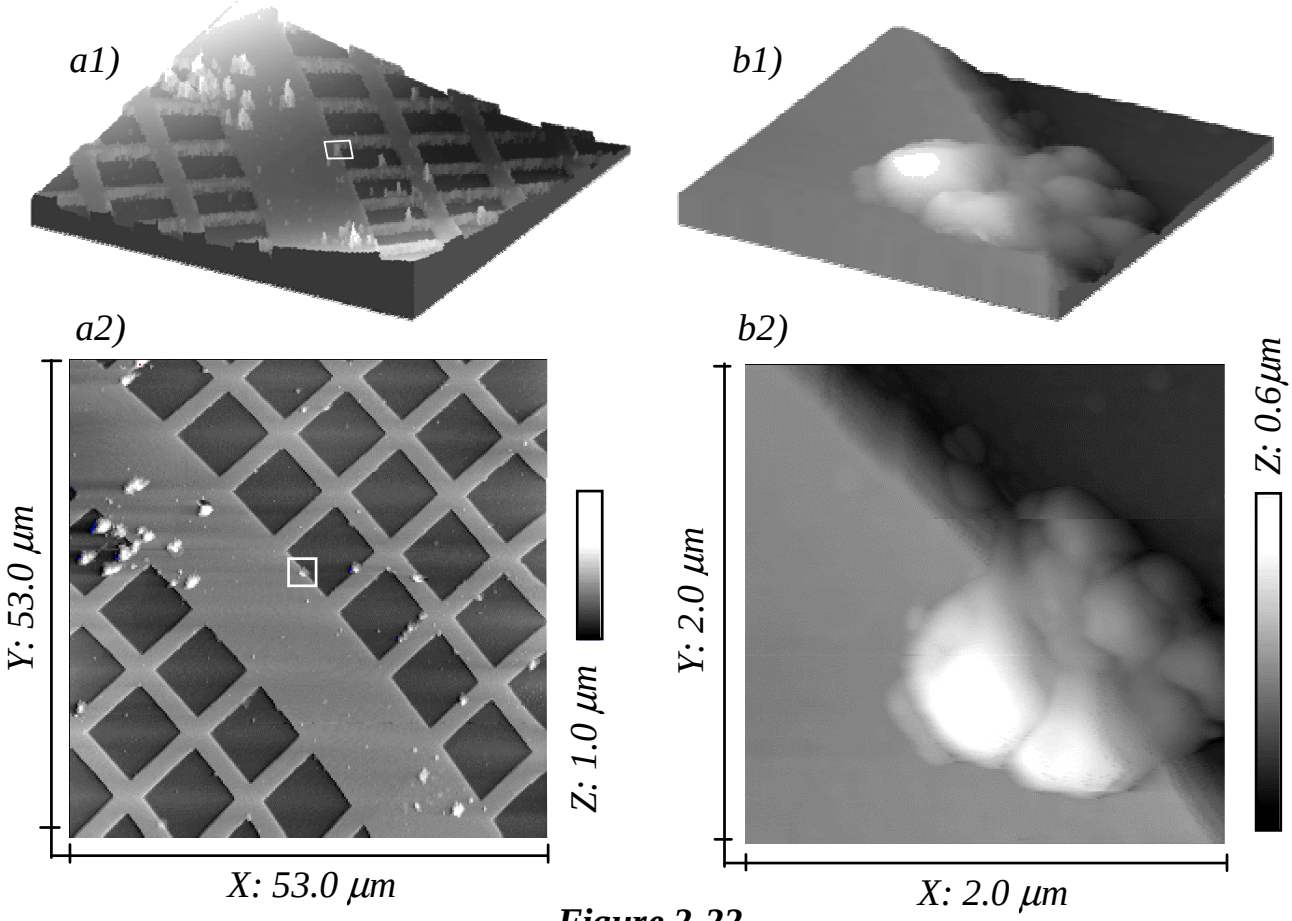

Figure 2-22

Two AFM images taken on the same area of a calibration grid. Figure a1) shows a 3-dimensional representation of raw data and highlights the inherent distortion produced by the scanner. Figure b1) shows a top view representation of the flattened data. Figure b1 and b2 show 2 different representation of a sub-area of figure a) highlighted by a white square.

2.6.2.2 Thermal and vacuum behaviour

The characterisation of the AFM under Mars equivalent conditions has been performed in a dedicated vacuum chamber (see Figure 2-23). The approach stage described in Figure 2-21 is mounted on a liquid cooling system with Pelletier elements. The cooling system is fixed on one of the flanges of the vacuum system together with the AFM electronics. This enables easy placing of the instrument into the vacuum chamber. A view port has been installed to observe the AFM approach. A constant flow of nitrogen is provided to create a dry environment. Using the described setup, the temperature at the AFM location could be cooled down to –10 °C.

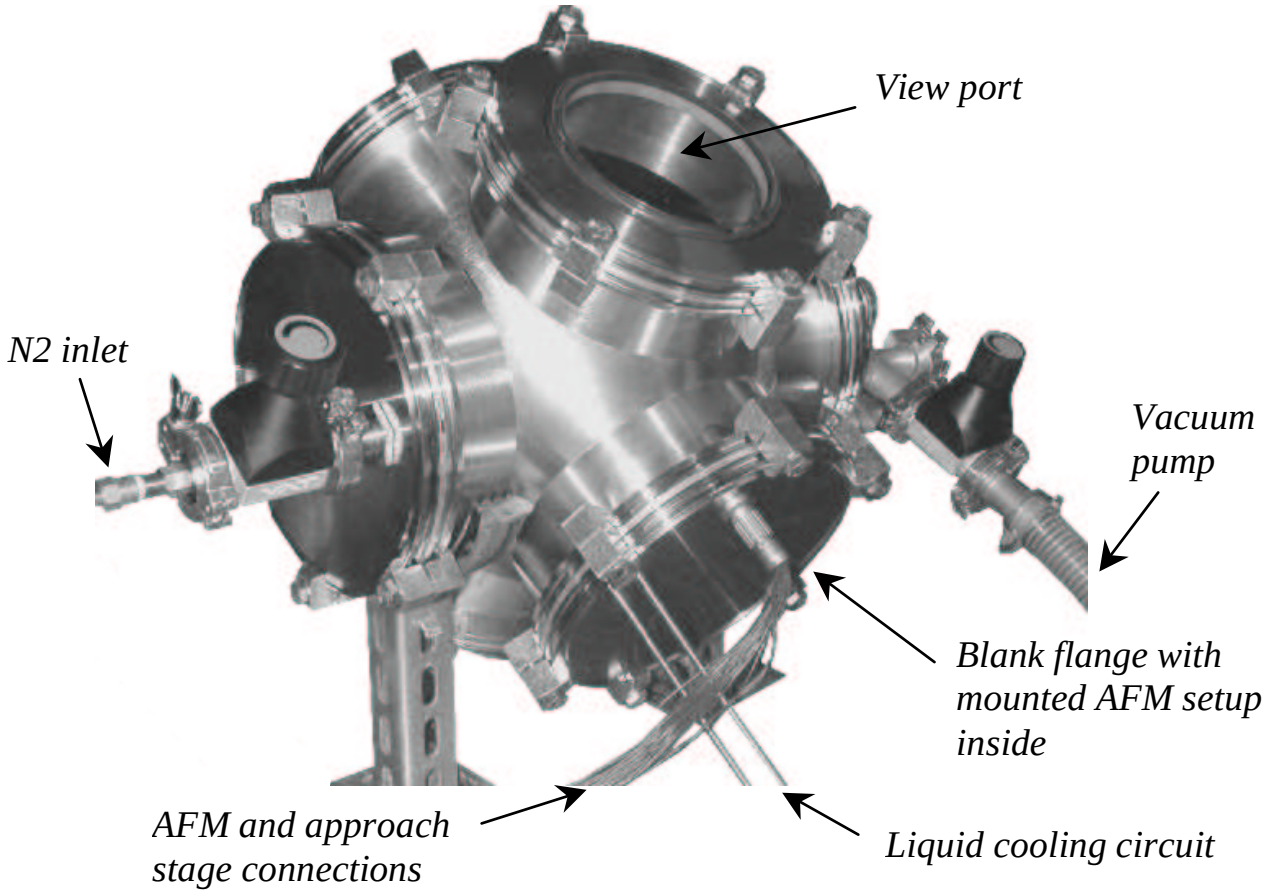

Figure 2-23
Vacuum chamber to simulate the Martian environment.

As mentioned in 2.3.2.1, the scanning behaviour of the AFM is influenced by temperature due to the viscosity change of the grease applied to the leaf springs of the scanner. By taking AFM measurements on a calibration grid, the distortions induced at low temperature operation can be highlighted. These distortions are particularly pronounced at the beginning of each scan line since the grease has a certain inertia (see Figure 2-24 a). The height information retrieved from the Z-motion of the scanner is distorted as well. In the displayed image, the height of the calibration grid is increased by a factor of 3. To prevent these distortions, the scanning speed needs to

be decreased significantly. At room temperature, a full scan images would take about 10 minutes whereas at –10 °C, a similar image takes about 25 minutes.
The scanner has bee characterized without damping grease as well. The vibrations produced by the leaf-springs are transmitted to the cantilever and detected by the feedback loop. At the beginning of each scan line, their contribution to the measured topography is increased (see Figure 2-24 b). It corresponds to a vibration amplitude of 7nm. When measuring in vacuum (Mars equivalent pressure of 7 mbar), these vibrations are again increased since less damping of the leaf springs is provided by the surrounding air. To prevent these vibrations to be present on the topography information, the sensitivity of the feedback loop can be decreased by adjusting the proportional (P) and integral (I) parameters. However, this reduces the height sensitivity of the AFM and the induced vibration will still be recorded on the error signal of the cantilevers.

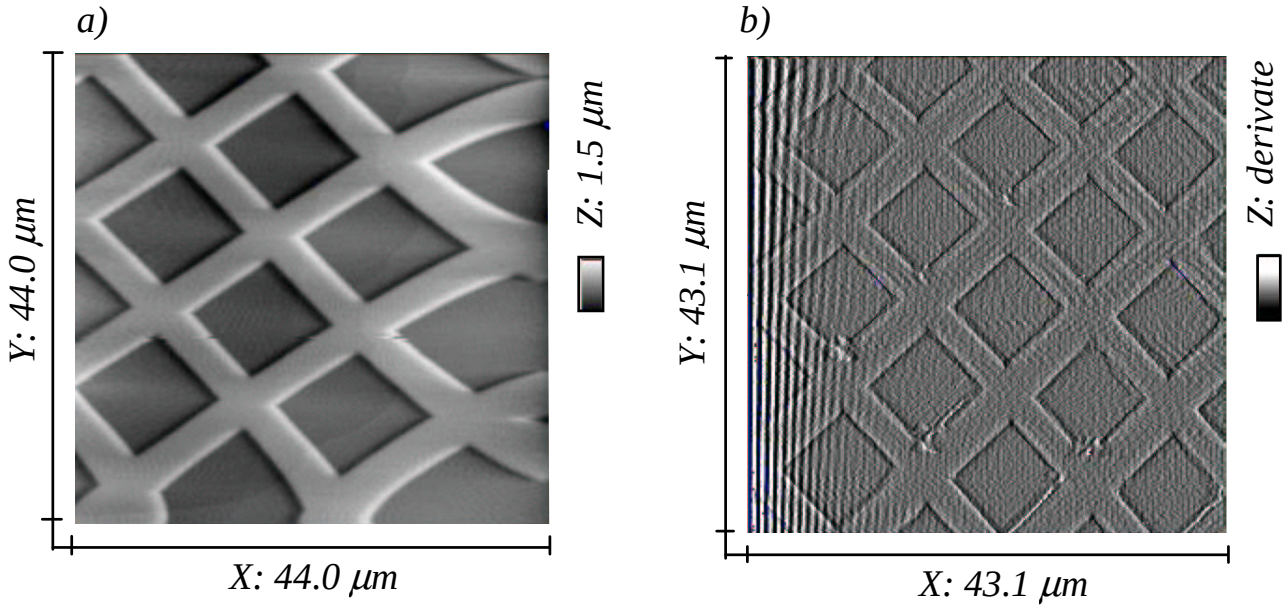

Figure 2-24
Characterisation of the scanner behaviour at low temperatures (0 °C).
Figure a) shows an image of a calibration grid with applied damping grease taken in backward scan (scan motion from right to left). The distortion due to creep effects of the damping grease is visible at the beginning of each scan line.
Figure b) shows the same calibration grid without damping grease taken in forward scan (scan motion from left to right). The image is shown in derivative mode to highlight the edges of the grid and the vibrations generated at the beginning of each scan line.

2.6.3 Vibration and shock tests

To prepare the AFM to its interplanetary journey where it will encounter extremes of vibration, pressure, temperature, radiation and shock, the instrument is put through a series of tests called environmental testing. These tests help to determine if the instrument components will be robust enough to handle the extremes of space. Most of these tests have been performed with the full MECA payload assembled. In this section the shock behaviour of the AFM is described. As these tests have been performed prior to implementation of the instrument into MECA, a separate vibration and shock platform has been used. The specified protoflight and acceptance spectra with could be closely reproduced.
Spectra of realized random vibration and shock compared to protoflight and acceptance curves are shown in Figure 2-25 and Figure 2-26. All vibration and shock exposures have been performed in all 3 axes with the same intensities.
During the shock tests, the exact protoflight spectra could not be reproduced for technical reasons. Thus, the instrument was exposed to a shock of 9000 g's at 2 KHz, exceeding by far the specified acceptance of 2500 g's. During this shock exposure in Z direction (relative to the scanner axes), cantilever number 8 was broken. This can be explained by the fact that the shock wave propagated better across the larger part of the silicon chip (where the reference piezoresistor is attached) compared to the narrower support beams (see Figure 2-2).

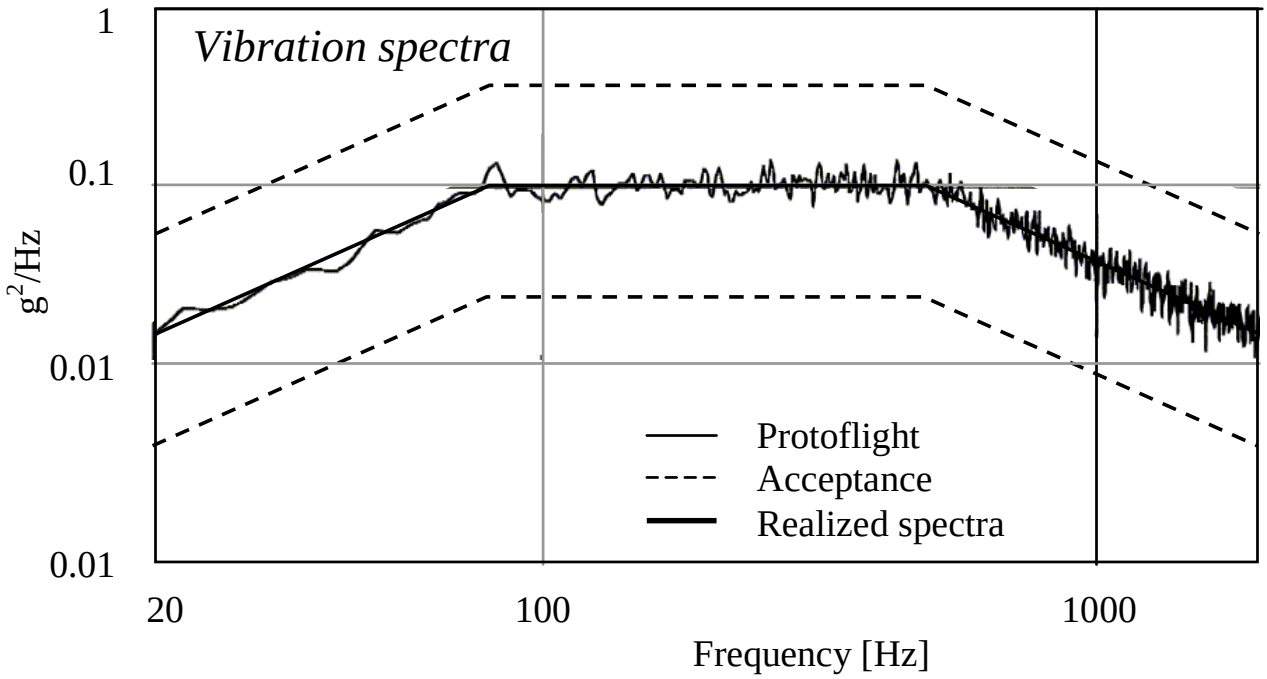

Figure 2-25
Random vibration spectra specified for protoflight. The bold line shows the spectrum that has been realized by the platform. The dashed lines describe the acceptance curves.

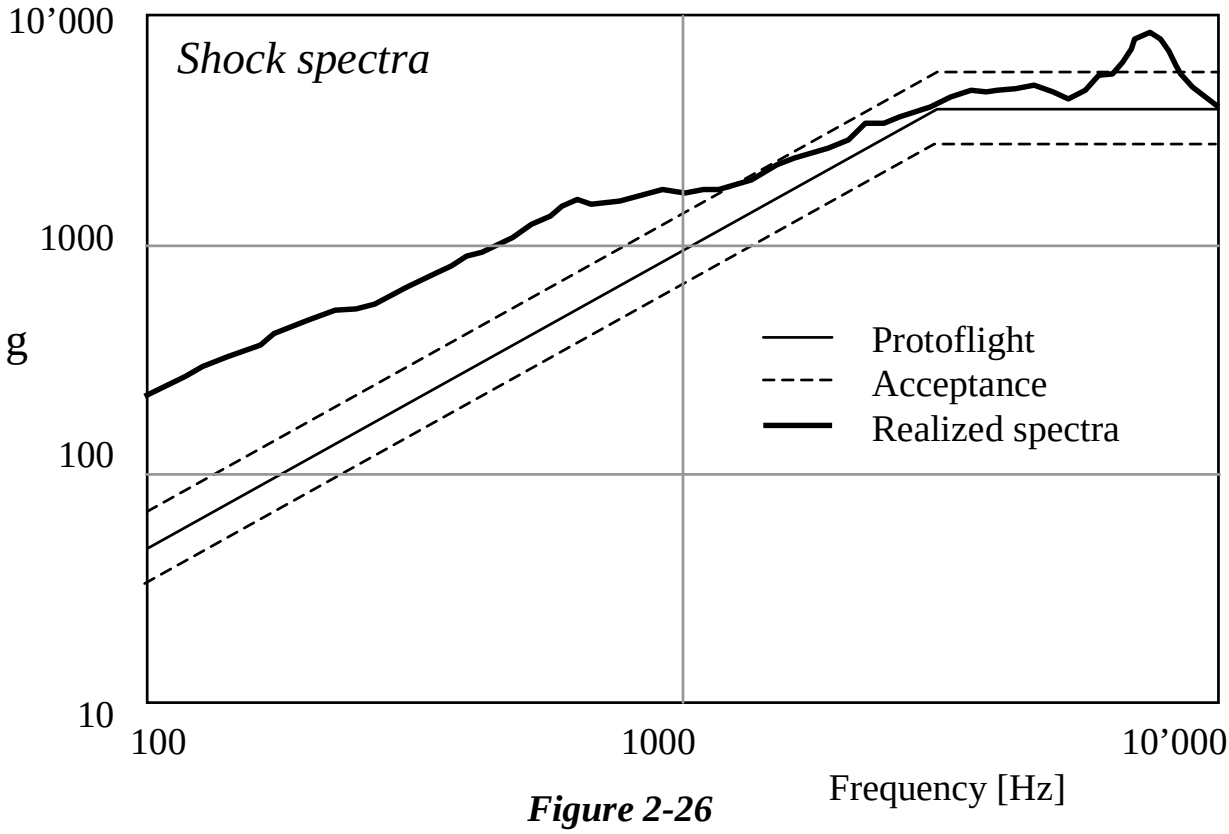

Figure 2-26

Shock spectra specified for protoflight. The bold line shows the spectrum that has been realized by the shock. The dashed lines describe the acceptance curves.

2.6.4 Operations on Mars

The mission plan for the 2001 lander was split into a 21 sols (Martian days) nominal operation and a 90 sols extended mission operation. For the first 21 sols, each payload gets a certain time allocated to perform its scientific investigations. This plan depends on the power requirements, the use of shared equipment and the compatibly with other payload experiments.
The basic operation is almost identical each payload: after receiving the first instrument status report, a short analysis of the data will guide the decisions on the following actions. A sequence of operation is then set up, submitted to a committee for validation and before being sent to Mars. The sequence is then executed and the results sent back to Earth. The 21 sols plan of MECA has the following operation related to AFM:

- Sol 0: MECA health checks
- Sol 1: Calibration of optical microscope and AFM using 4 different calibration targets
- Sol 8: Full analysis of surface soil sample by wet chemistry, electrometer, patch plates and both microscopes
- Sol 17: Full analysis of surface soil sample by wet chemistry, electrometer, patch plates and both microscopes

2.6.4.1 Telemetry and timing

Each experiment onboard the Lander will have a certain amount of data volume allocated. As the data transmission to Earth will be executed with limited bandwidth, the amount of data generated by each experiment needs to be known.
The number of AFM images taken during the mission strongly depends on the operational capabilities of the AFM, the scientific relevance of the first results and the allocated experiment time during extended mission. These parameters can only be determined after the first set of AFM images will be sent back from Mars. However, a prediction of the data volume generated by the AFM can be made by considering the following factors:
The image resolution contributes to the amount of data. Normally, an image resolution of 256 pixels will be sufficient to obtain a minimum resolution of 3 nm per pixel when scanning an area of 750 nm. For reducing the number of recorded images, the resolution can be increased to 512 and the nest-ratio-value of the AFM_Autozoom subroutine decreased (see § 2.5.1.2).
The height information of each pixel is encoded with 8 bits, which divides the specified Z range into 256 segments. When encoding the full dynamic Z range of the scanner (14 μm), a resolution of 54 nm is obtained. This dynamic range can then be decreased by factors of 2, 4, 8 and 16.
When scanning a surface, the AFM transmits both forward and backward records to the lander computer. This can increase the confidence of the measurement when comparing both measurement lines. In a first approach, only one direction will be transmitted to earth to reduce the amount of data. If any doubts arise on measured features, the second image can be transmitted as well.
Two different channels are measured at each point. The Z feedback channel translates the vertical motion of the scanner when the feedback loop is closed. The error channel translates the remaining deflection (in static mode) or phase shift (in dynamic mode) of the cantilever with closed feedback loop. To be able to precisely characterize the behaviour of the AFM and increase the reliability of the shape of the features, the analysis of both channels is necessary.
The number of images per area can be estimated by a fully executed AFM_Autoimage routine where a set of 4 subsequent images will be generated. Table 2-2 resumes the described values.

The time necessary to take an AFM image depends on the following parameters:

- Image size
- Image height
- Image quality
- Temperature (see § 2.6.2.2)
- Sample (calibration sample or loose particles)

Considering all these factors, the average time to take an image is 25 minutes. Thus, a set of 4 images generated by a single and fully executed AFM_Autoimage command would take at least 2 hours of AFM operation.
The total data volume per area is therefore 8.4 Mbits. If a nominal JPEG compression is performed, this amount is reduced to 2.1 Mbits.
The communication data rate between the lander and the Mars '01 orbiter will be of 128 Kbits per second, whereas the data rate between the orbiter and Earth is limited to 86 Kbits per second. Therefore, the transmission of this set of 4 images will take about 30 seconds of communication.

Table 2-2
AFM data volume.

	Nominal	Maximum
Number of pixels per line:	256	512
Number of lines per image	256	512
Number of bits per pixel for height information	8	8
Number of measurements (Forward and backward)	1	2
Number of channels (height and error signal)	2	2
Number of images per area	4	4
Number of images on substrate	2	4
Data volume per area (uncompressed)	8.4 Mbits	134.2 Mbits
Data volume per area with 4x JPEG compression	2.1 Mbits	33.6 Mbits
Data volume for a set of 9 substrates (compressed)	18.9 Mbits	302 Mbits

2.7 References

1 : S. Gautsch, T. Akiyama, N.F. de Rooij, U. Staufer, Ph. Niedermann, L. Howald, D. Müller, A. Tonin, H.-R. Hidber, W.T. Pike, "Development of an AFM Microsystem for Nanoscience in Interplantary Research", Proc: 3rd Round table on Micro/Nano-technologies for space – Scientific Payloads, 173, Noordwijk, NL, (2000).

2 : S. Gautsch, U. Staufer, "Un microscope sonde les poussières martiennes", Journal des Ingénieurs et Architectes Suisses, **11**, 228, (2000).

3 : L. Howald, T.Akiyama, S. Gautsch, H.-R. Hidber, D. Müller, Ph. Niedermann, T. Pike, A. Tonin, U. Staufer, "Development of the space SFM for interplanetary missions", Proc. 4th Seminar on Quantitative Microscopy QM 2000, 209, Semmering, A, (2000).

4 : S. Gautsch, T.Akiyama, N.F. de Rooij, U. Staufer, Ph. Niedermann, L. Howald, D. Müller, A. Tonin, H.-R. Hidber, W.T. Pike, M.H. Hecht**,"** Atomic Force Microscope for Planetary Applications**",** Proc. Solid-State Sensor and Actuator Workshop, 267, Hilton Head Island, USA, (2000).

5 : W.T. Pike, M. H. Hecht, M.S. Anderson, S. Gautsch, T. Akiyama, N.F. de Rooij, U. Staufer, Ph. Niedermann, L. Howald, D. Müller, A. Tonin, H.-R. Hidber, "Atomic Force microscope for imaging and spectroscopy", Proc. Concepts and approaches for Mars exploration, 6186.pdf, Lunar and Planetary Institute, TX, USA, (2000).

6 : W.T. Pike, M.H. Hecht, P.H. Smith, U. Staufer, "A Microscopy Station for Mars", Inst. Phy. Conf. Ser. No **168**: section 4, 163, (2001).

7 : S. Gautsch, T Akiyama, N.F. de Rooij, U. Staufer, Ph. Niedermann, L. Howald, D. Müller, A. Tonin, H.-R. Hidber, W.T. Pike, M.H. Hecht**, "**Atomic Force Microscope for Planetary Applications**",** Sensor and Actuators, **A 91**, 321, (2001).

8 : S. Gautsch, T.Akiyama, N.F. de Rooij, U. Staufer, Ph. Niedermann, L. Howald, D. Müller, A. Tonin, H.-R. Hidber**, "**Miniaturized Atomic Force Microscope for Planetary Applications", Proc. 9th European Space Mechanisms & Tribology Symposium, ESA SP-480, 11, Liège, Be, (2001).

9 : R.M.Payton, "Mars Surveyor program: Environmental Requirements Document", MSP01-98-0029, (1998).

10 : Office of space science, "Nasa Procedure and Guidelines (NPG)", 8020.12B, (1999).

11 : M. Tortonese, R.C. Barrett, C.F. Quate, "Atomic Resolution with an Atomic Force Microscope Using Piezoresistive Detection", Applied Physics Letters, **62**, 834, (1992).

12 : P. Niedermann, W. Hänni, D. Morel, A. Perret, N. Skinner, P.-F. Indermühle, P.-A. Buffat, N. F. DeRooij, "CVD Diamond Probes for Nanotechnology", Applied Physics, **A66**, 31, (1998).

13 : P. Niedermann, W. Hänni, S. Thurre, M. Gjoni, A. Perret, P.-F. Indermühle, U. Staufer, N. F. DeRooij, "Mounting of Micromechanical Diamond Tips and Cantilevers", Surface and Interface Analysis, **27**, 296, (1999).

14 : J. Melngailis, "Focused ion beam technology and applications" J. Vac. Sci. Tech. **B5**, 469, (1987).

15 : H.L. Offereins, K. Kühl, H. Sandmaier, "Methods for the Fabrication of Convey Corners in Anisotropic Etching of (100) Silicon in Aqueous KOH", Sensors and Actuators, **A25**, 9, (1991).

16 : U. Dürig, H.R. Steinauer,"Dynamic Force Microscopy by Means of the Phase-controlled Oscillator Method", Journal of Applied Physics, **82**, 3641, (1997).

17 : Nanosurf AG, Switzerland , "Easyscan Serial Protocol Information", v1.1, (1999).

18 : C. Beuret, "Development of a Double Moulding Technique for the Microfabrication of Diamond Scanning Probe Tips", Dissertation submitted to the Faculty of Science of the University of Neuchâtel, (1999).

19 : W.C.Young , "Roark's formulas for stress and strain 6th edition", McGraw Hill International Editions, ISBN 0-07-100373-8, (1989).

3. PARTICLE MEASUREMENTS

The scientific measurements that have been performed within this work pursued two distinctive goals. A technical goal where particle imaging techniques under Mars equivalent conditions are studied, and a second, scientific goal to create a database of particle images using a setup close to the flight system. This database will be a precious reference to give the results arriving from Mars a stronger scientific relevance. Based on the results of previous experiments on Mars regarding dust properties, our interest focuses particularly on the characterization of α-quartz in the respirable particle size range (between 100 nm and 3 μm in diameter).
AFM is rarely used to characterize dust particle properties like shape, size distribution, hardness or mass. The first section of this chapter gives the reader an overview of commonly used dust characterization methods.
In the second section, particle measurement techniques by AFM are explained and results on the α-quartz particles are shown. The last section discusses the obtained results and the further developments necessary to improve the scientific impact of AFM particle measurements.

3.1 Dust analysis techniques

Depending on the environment, the collection capabilities and the required sample preparation before the analysis, different methods for inferring dust properties can be distinguished. Several of these analytical techniques, that are often taken for granted on Earth, are extremely difficult to implement on remote missions on Mars. To highlight the technological differences between terrestrial instrumentation and experiments designed for space, this section is divided into Earth-bound and in-situ methods.

3.1.1 Methods for Earth-bound dust analysis

Most of the described characterization methods require a sample collection system to be able to analyze the particles. An impinger is frequently used to collect airborne particles. It is based on a glass bubble tube designed for the collection of aerosols into a liquid medium. When a known volume of air bubbles is pumped through the glass tube, the liquid inside the tube can be analyzed to determine the airborne dust

concentrations. Other dust collection techniques rely on electrostatic and thermal precipitation [1].

- Scanning electron microscopy (SEM) for size distribution and shape [2]:
  The particles placed on a conductive substrate are non-destructively bombarded by a finely focused beam of electrons. As the particles are irradiated by this stream of primary electrons a variety of interactions occur with the atoms of the particles. As a result, various forms of radiation are released from the sample which, when detected and processed, can be used to determine its constituent components. The secondary electrons produced by the sample are used routinely to characterize the particle morphology. These sample electrons are used to create unique, large depth of field, secondary electron images. They provide information on the size, shape, and surface topography of individual particles ranging in size from 100 nm to 1mm. Figure 3-1 shows an SEM image of accumulated quartz particles.

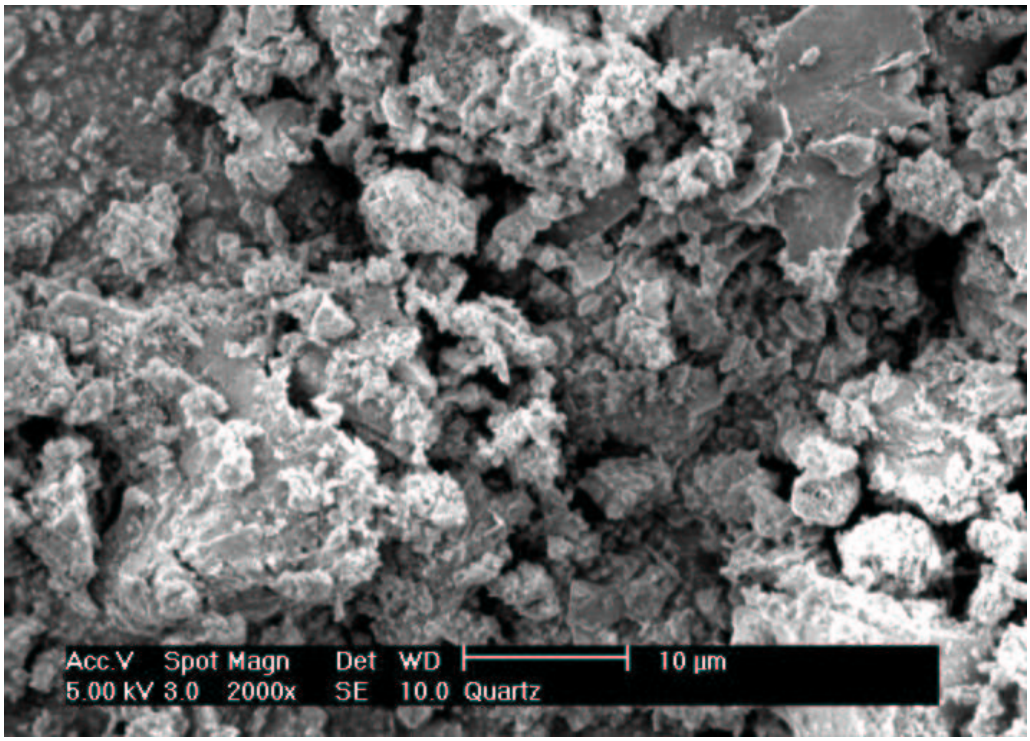

Figure 3-1
SEM image of quartz particles deposited on a flat substrate.

- Energy dispersive x-ray (EDX) for dust composition [2]:
  Determining the actual composition of an individual particle requires an analysis of the energies of the x-rays generated when an electron beam interacts with the sample atoms. The characteristic x-rays have energies that are specific to each element present in the sample. Such a system is often implemented with an SEM.

http://www.upstate.edu/pathenvi/art/xray.gifA visual representation of particle composition can be created by mapping the occurrence of characteristic x-rays to their point of origin on the particles imaged in the SEM. http://www.upstate.edu/pathenvi/art/kev.gifAn alternative way of expressing information on particle chemistry is to quantify the proportions of each element present in the individual particles. Element concentrations can be determined from the heights of the peaks in the x-ray spectrum.

- Optical microscopy for dust concentration and shape [3,4]:
  Microscopic counting of dust collected by impingement can be used to determine dust concentrations. Depending on the resolution of the microscope, individual shapes of particles can be observed. The usual lower limit of diameter of particles seen is approximately 1.0 µm. Optical microscopy suffers from narrow depths of focus at high magnifications. Confocal systems can increase this depth of focus. Other optical microscopes use dark-field illumination with which it is possible to see particles as small as 100 nm in diameter. Figure 3-2 shows an optical image of red Aeolian sand [5] taken with the optical microscope onboard the payload MECA (see § 1.4).

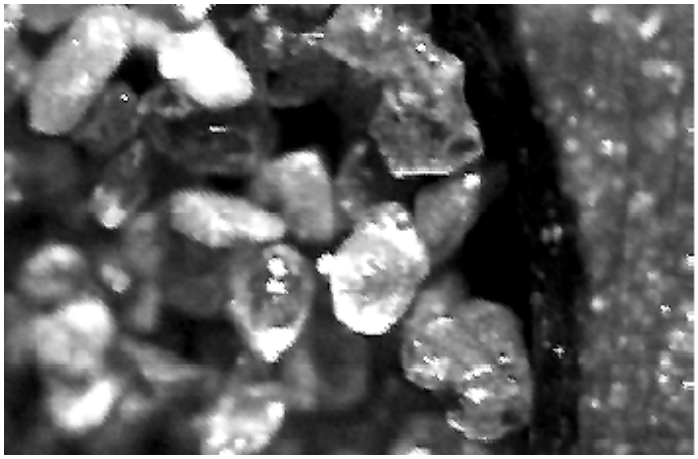

Figure 3-2
Optical image taken with the microscope onboard the payload MECA. The image width is 1.5 mm.

- Laser particle size analyzer [6]
  Laser Particle Size Analysis consists in measuring the size of particles using the diffraction and diffusion of a laser beam. Two theories are used depending on the size of the particles: the Fraunhofer theory is applicable for particles with large size compared to the wavelength λ (diffusion and absorption are not considered).
  For smaller particles, it is appropriate to use Mie theory. It takes into account both diffraction and diffusion of the light around the particle in its medium. To use the Mie model, it is necessary to know the complex refractive index of both the sample and the medium. This complex index has a real part, which is the standard refractive index, and an imaginary part, which represents absorption.

- Triboelectric discharge for airborne dust concentration [7]:
  When airborne particles collide with one another, they acquire an electrical charge. If these electrically charged particles strike a measuring probe, the charge is transferred to this electrode. The collected current flowing through the probe is thus proportional to the number of particles colliding with it. The result will accurately correspond to dust emissions, since it depends not only on dust concentration, but also accounts for the velocity of the particle flow.

- Optical obscuration measurement for airborne dust concentration [8]:
  In this method, a laser beam or LED source crosses the air section containing the airborne dust. On the other side of the section, a receiver unit measures the laser beam's weakening caused by dust content. Additionally, the laser unit sends a reference signal around the section via an optical fiber.

- Total mass method for dust concentration:
  The simplest method of measuring dust concentrations is to determine the total weight of dust collected in a given volume of air. The total mass, however, is determined to a considerable extent by the large dust particles. Thus, the filtering method applied when collecting the sample becomes predominant.

3.1.2 Methods for in-situ dust analysis

Development of in-situ versions of Earth-bound dust characterization instruments is difficult due to limitations in power, mass, volume and human interaction. Several experiments have been proposed for future robotic missions. While some of them have already been performed on Mars, others have yet to be selected for future missions.

3.1.2.1 Performed experiments:

- Infrared spectroscopy
  Airborne dust characteristics like size distribution, shape and composition could be evaluated by infrared spectroscopy from orbiting spacecrafts and landers. The results of these experiments are described in detail in § 1.3.2.

- Dust obscuration of solar arrays [9,10]
  For the Pathfinder mission in 1997, two instruments have been developed to measure the dust accumulation during the course of the rover experiments. A solar cell coverglass transmission experiment to measure the change in optical opacity of a transparent coverlass as dust settles on the surface, and a quartz crystal monitor to measure the mass of dust deposited on an

oscillating quartz crystal as dust settles on the surface. The results of this experiment gave information on the dust concentration near the surface. In addition, a CCD microscope to observe the settled dust has been proposed but was not flown on the Pathfinder mission. The microscope had a resolution of 500 nm per pixel covering a surface of 20 x 20 μm [11]. A follow-on experiment was proposed on the cancelled Mars-2001 Surveyor lander as part of the MIP experiment (Mars In-Situ Propellant Production Precursor).

- Magnetic properties of dust [12]
  Pathfinder investigated the dust in the atmosphere of Mars by observing its deposition on a series of magnetic targets on the spacecraft. It involved an array of permanent magnets on the lander. The magnets have then been imaged by the lander camera.

3.1.2.2 Proposed experiments for future Mars and cometary missions:

- Optical microscopy and dust accumulation
  Two instruments were developed to fly as part of the MIP (Mars In-situ Propellant Precursor) experiment on the now postponed Mars 2001 Surveyor Lander. The first instrument MATE (Mars Array Technology Experiment) characterizes the solar energy reaching the surface of Mars, and measures the performance and degradation of solar cells under Martian conditions. The second experiment is called DART (Dust Accumulation and Removal Test) and characterizes the dust environment of Mars, measures the effect of settled dust on solar arrays, and investigates methods to mitigate power loss due to dust accumulation. Optical characterization of the settled dust is performed with an optical microscope having 0.5 μm resolution [13,14].

- Optical microscopy and Raman Spectroscopy
  A confocal imaging system incorporating a Raman spectrometer has been developed for NASA's Mars Instrument Development Program. The instrument incorporates a Silicon micromachined two-dimensional scan mirror, enabling video-rate confocal microscopy with the added feature of spectroscopic analysis of a point in question on the sample. Both imaging and Raman spectroscopy are performed with approximately 1 μm resolution [15].

- Dynamic properties
  The MAGO (Martian Atmospheric Grain Observer) experiment provides direct quantitative measurements of mass, size and shape distributions, as well as dynamic behavior of atmospheric dust. The instrument combines

three types of sensors to monitor simultaneously the dust cumulative flux (Micro Balance System, MBS) and the single grain dynamic parameters (Grain Detection System, GDS, + Impact Sensor, IS) [16].

- Atomic force microscopy on cometary dust grains
  The Rosetta mission will be launched by the European Space Agency (ESA) in the year 2003 to rendezvous with comet Wirtanen. It includes a large number of experiments to explore the cometary nucleus and its environment. MIDAS (Micro-Imaging Dust Analysis System) has been selected as scientific payload on the Rosetta orbiter. The MIDAS instrument is based on an AFM who's main scientific objectives concern the microtopographic and statistical analysis of cometary dust grains [17,18]. Interplanetary dust particles (IDP) collected in Earth's stratosphere have been measured by MIDAS as pre-mission experiment [19].

3.2 Dust characterization by AFM

The following sections resume the results obtained by measuring particles with the FAMARS AFM. After having introduced the reader to artifacts arising from AFM investigations and described the measurement setup, the obtained results are shown. Since 2 distinct measurement techniques have been used (direct and reverse imaging), the results have been separated into separate sections [20].

3.2.1 Tip artefacts

The main uncertainty of AFM images is due to the finite size and shape of the tip itself when the features to be imaged have high aspect ratios. A tip that has a large opening angle can measure very flat surfaces without much loss of information, but will not be able to trace the true profile of a feature with high aspect ratios sharper than the probe tip. The tip curvature plays an important role for accurately measuring flat topographies as the recorded topography is always a convolution of the local surface curvature and the AFM tip curvature. Tip artifacts have been well documented in the literature [21,22,23,24]. Figure 3-3 shows the effect of the tip shape on the recorded profile in a 2-dimensional example. Figure a) shows a calibration grid measured with a sharp tip whereas Figure 3-4 b) the same grid measured with a blunt tip.
To be able to characterize the actual tip shape, a calibration sample[1] composed of a matrix of very sharp tips can be used (see Figure 3-5 a). As the curvature of the tips present on the sample is very small (typically 10 nm), an AFM measurement of such a sample will show repeatedly the topography of the AFM tip (see Figure 3-5 b).

[1] Silicon calibration grating TGT01 by μ-mash: www.siliconmdt.com.

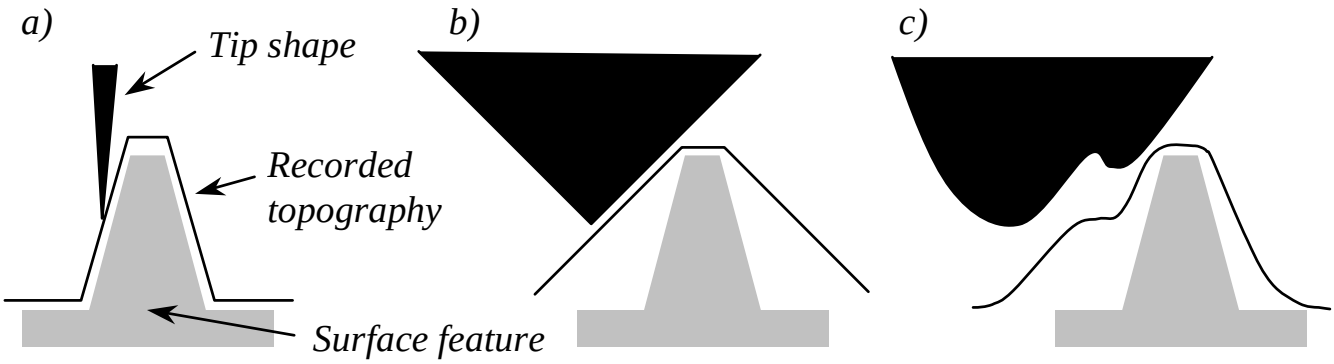

Figure 3-3

3 examples of tip convolution effects. If the tip has a smaller opening angle and a smaller curvature than the surface feature, the recorded topography is not altered (case a). If the tip opening angle (case b) or the tip curvature (case c) is higher than the sample feature, the recorded topography is significantly different from the real surface topography.

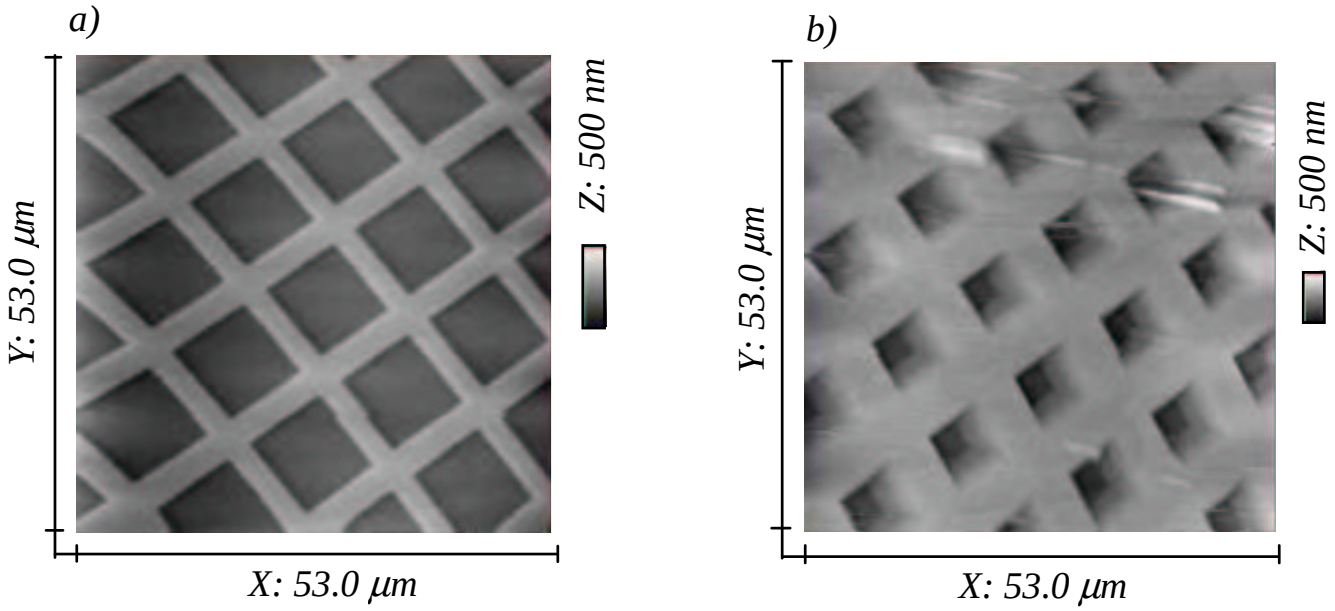

Figure 3-4

a) AFM image of a calibration grid measured with a sharp tip.
b) AFM image of the same sample recorded with a blunt tip.

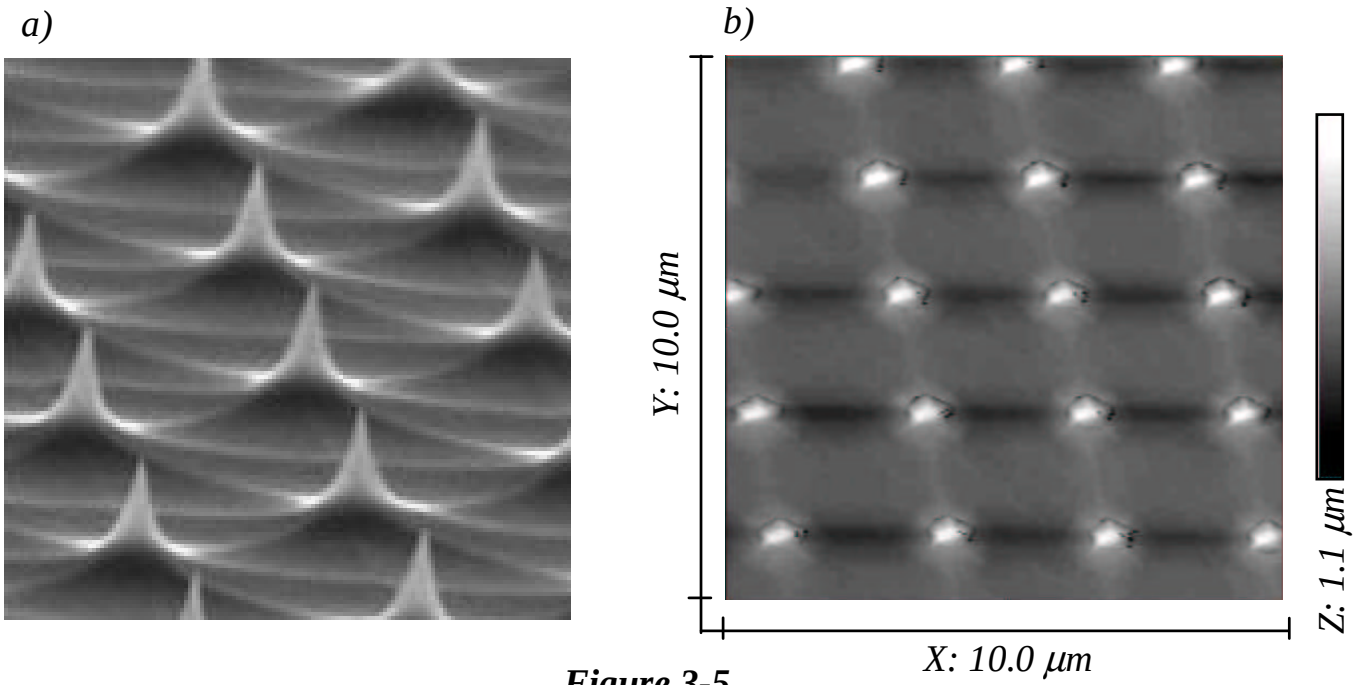

Figure 3-5

a) SEM image of the tip calibration sampleTGT01 showing a matrix of tips (courtesy of Silicon mdt).

b) AFM image of the tip calibration sample TGT01 to characterize the AFM tip shape. The image distortion in X-Y proportions and in orthogonality can be easily detected since the tips are arranged in orthogonal and equidistant manner.

3.2.2 Experimental setup

The AFM measurements have been performed with a setup close to flight configuration. However, the dust sampling system used to deliver the dust particles in front of the AFM (see § 1.4.3) was not available. Manual deposition of the particles on the substrates has been performed and an autonomous approach procedure has been used to drive a stepper-motor stage. The setup is either enclosed in a glove box or the vacuum system described in § 2.6.2.2 to avoid inhaling of the quartz particles and for humidity control.

3.2.2.1 α-quartz samples

A standard reference material (SRM) for quantitative analysis by x-ray powder diffraction has been used to perform the preliminary AFM measurements on particles. These α-quartz particles delivered by the American National Institute of Standards Technology (NIST) were prepared of single crystal nodules of Brazilian quartz, which was crushed and jet-milled to a median particle size of 1.6 µm. The resulting powder was then washed in hydrofluoric and hydrochloric acid, rinsed, ignited at 500°C and bottled. The certified purity of the material expressed in mass fraction is 100% $^{+}$-0.21% crystalline α-quartz. The particle size distribution has been determined by laser scattering. The typical distribution is shown in Figure 3-12.

3.2.3 Direct imaging

3.2.3.1 Substrate characterization

Additionally to the scanner and tip calibration substrates shown in Figure 3-4 and Figure 3-5, several substrates for fixing and scratching the particles have been characterized by AFM before being exposed to the particles.
In particular, a nickel plate coated with a 200 nm thick layer of PMMA (Polymethyl methacrylate) was used to immobilize the particles. The relatively high roughness of the nickel surface is clearly visible in Figure 3-6 a). To use this substrate with particles, PMMA is deposited onto the plate with a spin-coater. The particles are then placed on the fresh PMMA and baked to harden the substrate.

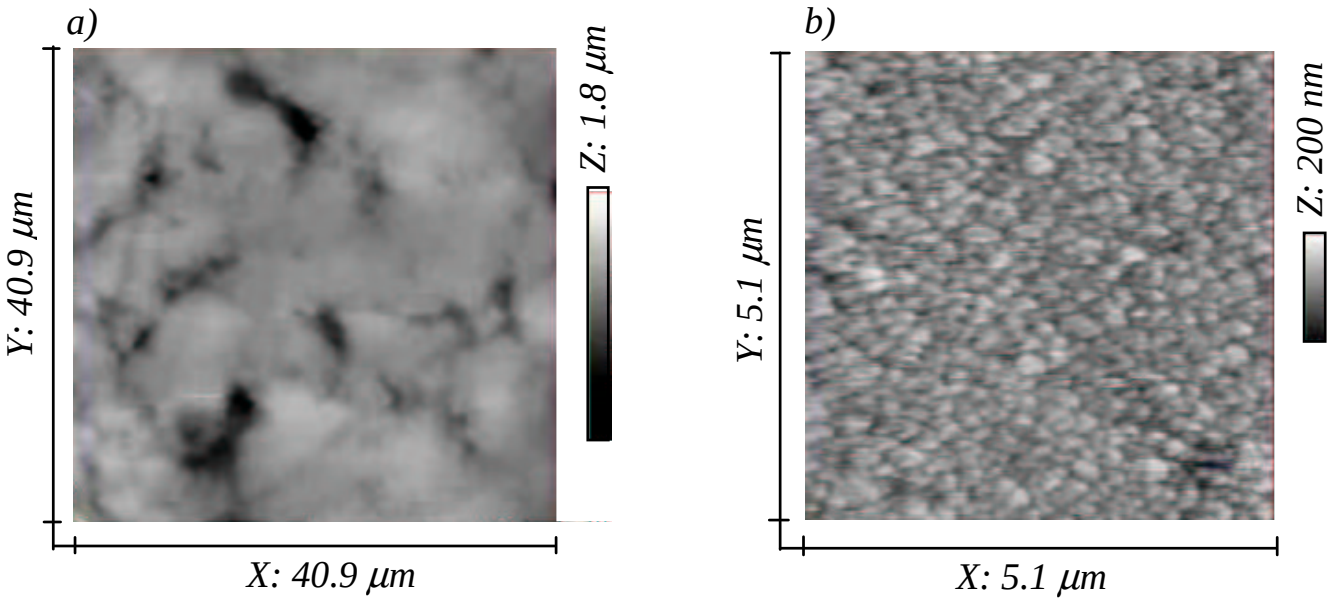

Figure 3-6
Static mode AFM images of the substrates before particle deposition:
a) PMMA coated nickel plate for particle immobilization. The relatively high roughness stems from the topography of the nickel surface.
b) Polished silicon wafer with aluminium layer used for scratch tests. The roughness of the surface is 50 nm RMS.

The scratch tests to determine the particle hardness have been performed on a polished silicon wafer coated with a 200 nm thick aluminum layer. Aluminum has a hardness of 2.9 on the Moh's scale. As quartz is much harder (7 on the Moh's scale), the relatively soft aluminum surface is expected to exhibit well-defined scratches in the substrate. To verify that the surface is scratch free before placing the particles, it has been characterized by AFM. Figure 3-6 b) shows the surface roughness of the polished and Al-coated wafer.

AFM measurements on a clean substrate can be performed either in static or dynamic mode. Since no loose objects are present on the sample, the static mode technique produces satisfying results.

3.2.3.2 Particle measurements

Static mode

The measurements using static mode detection showed the expected results. The lateral tip to sample interaction is too high to keep the loose particles in place. Figure 3-7 shows an image of a nickel substrate coated with PMMA with loose α-quartz particles on it. For most of the scan-lines, only the substrate is imaged correctly. On some distinctive lines, the tip jumps over a particle, before pushing it out of the scan-field during the next scan-line. A subsequent dynamic mode image of the same area supports this interpretation since no particles are present in the previously scanned area.

The vertical force acting on the sample is estimated to be 1 μN, which corresponds to a vertical bending of the cantilever of 50 nm. The minimum scan speed that has been tested was 1 μm/s. Even with such low values, no particles could be successfully imaged in static mode.

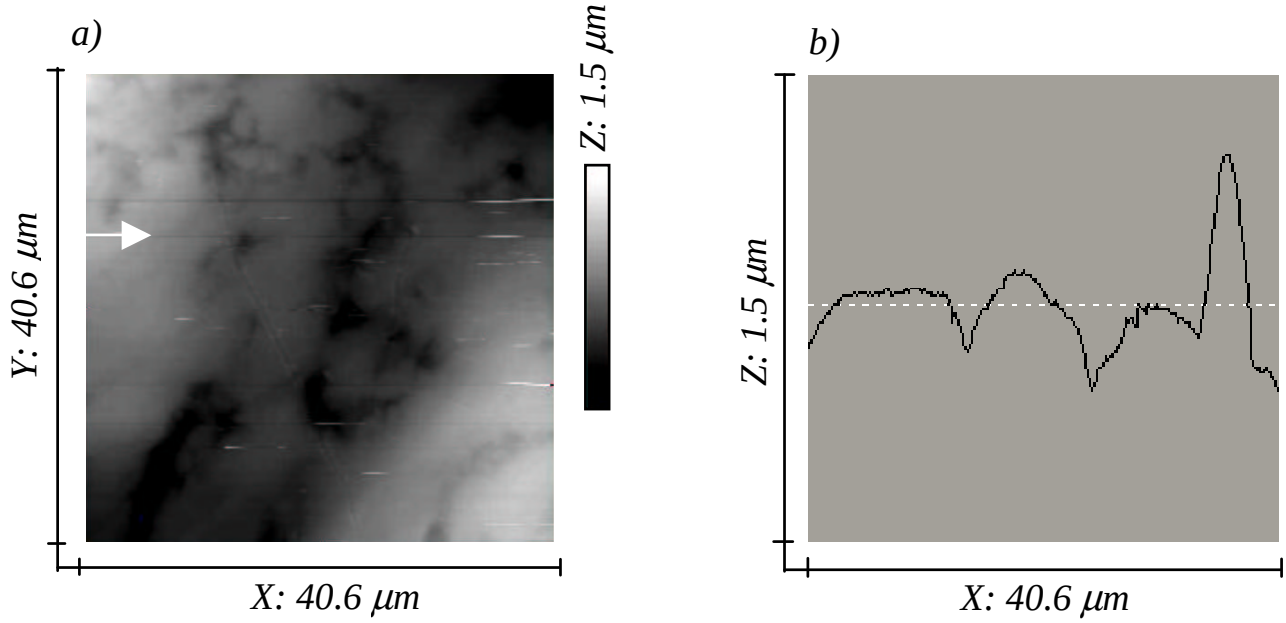

Figure 3-7

AFM image of Nickel-PMMA substrate with loose particles taken in static mode. Figure a) shows the substrate topography and white lines produced by the displaced particles. Figure b) shows the cross section located at the white arrow in figure a). On the left part of figure b), the particle shape has been measured for one scan line before being displaced by the tip.

Dynamic mode

As the substrate is in a vertical position, gravity could be of concern since unstable particles might fall off the substrate when touched by the AFM tip. However, it has been observed that most particles displaced by the tip stay on the substrate and can be re-imaged afterwards. The success of imaging particles in dynamic mode strongly depends on the effective scan-speed for a given response time of the feedback loop.

In general, a given scan speed leaves some particles in place while others are displaced. Stable particles are considered to be embedded in the polymer whereas unstable particles are immobilized only by surface adhesion. This assumption is supported by the fact that the particles, which have been moved, leave no groove or trace in the cured polymer. This difference in particle stability among the non-embedded particles is believed to depend on the following factors:

- Size of contact area of the particle with the substrate
- Aspect ratio of the particle and orientation relative to the surface
- Proximity to embedded particles

This assumption is motivated by the fact that some particles can be partially imaged before being flipped or moved out of the scan field. As the tip to particle interaction is kept constant by the feedback mechanism, this partial imaging can be explained by the mentioned reasons.

Typically, a scan-speed of 2 μm/s will leave every particle in place (see the two images of Figure 3-8) while a speed of 7 μm/s will displace most of the particles. The area of Figure 3-9 measured at different scan speeds illustrates this observation.

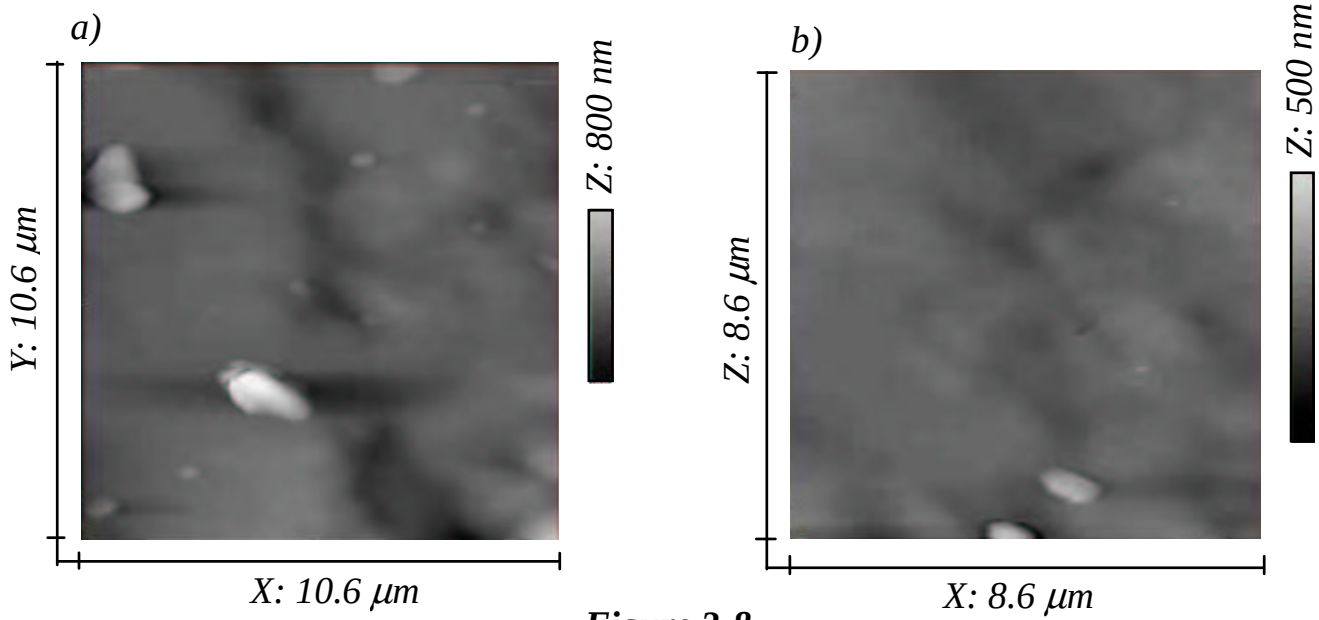

Figure 3-8

Two AFM images taken at 2 μm /s of quartz particles on nickel-PMMA substrate. Figure a) shows several particles with different sizes going from 350 nm to 1.55 μm. Figure b) shows only 2 off-centred particles.

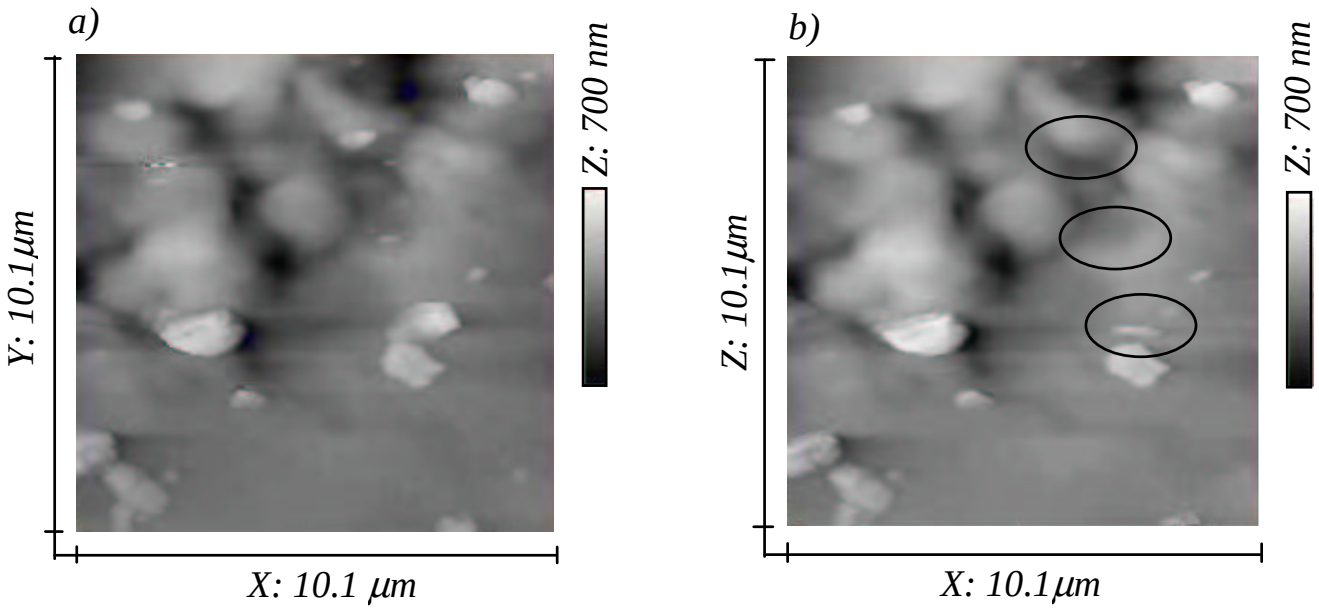

Figure 3-9

Two AFM mages taken on the same area. Figure a) has been scanned from top to bottom with a slow scan speed (1.7 µm/s). Figure b) has been taken from bottom to top with a faster scan speed (6.8 µm/s). In figure b), three of the particles present if figure a) have been moved out of the scan area after being scanned for a few lines.

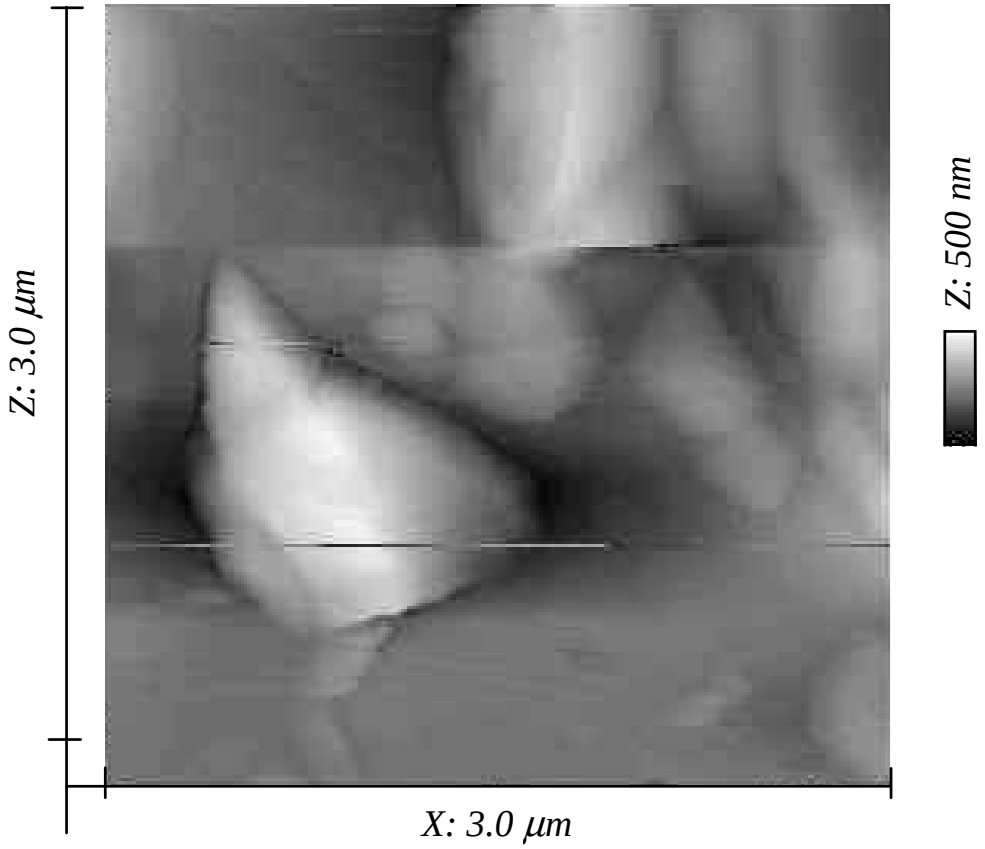

Figure 3-10

High resolution image (11 nm per pixel) of a single quartz particle.

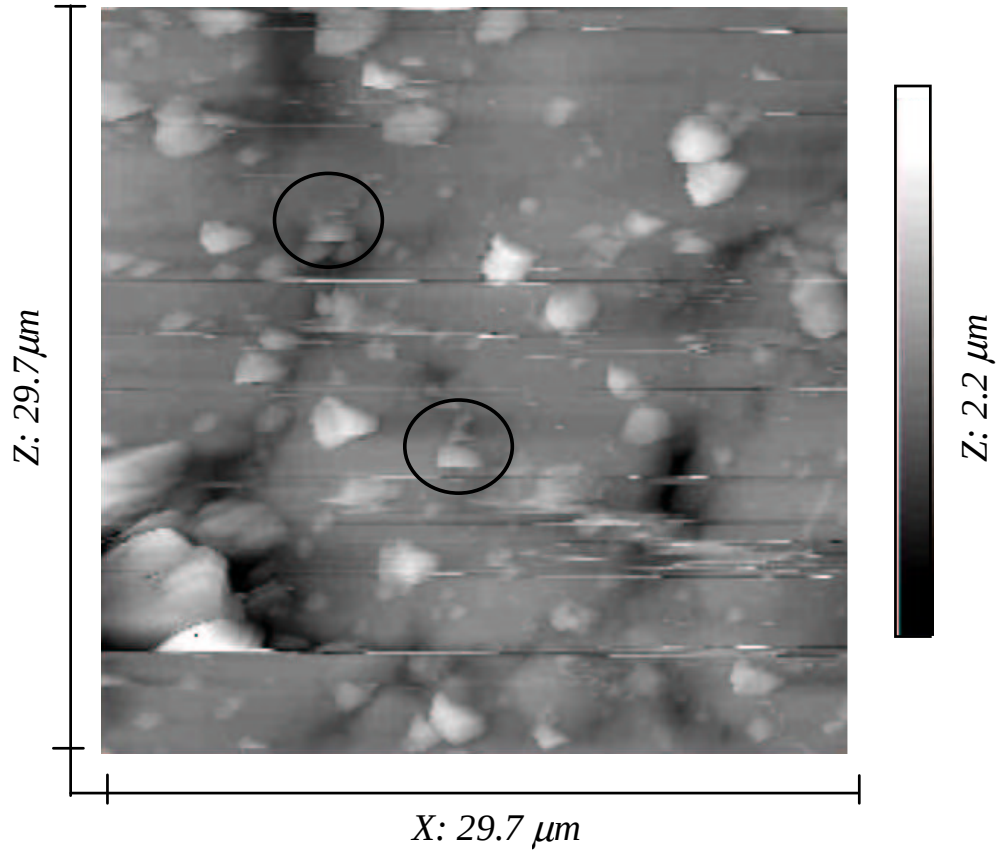

Figure 3-11

Large AFM scan showing about 69 particles. The image was scanned from top to bottom. Some particles are displaced by the tip while others stay in place. The particles highlighted by black circles have been partially imaged before being moved out of the scan area. The size distribution retrieved from this image is already close to the typical distribution (see Figure 3-12).

3.2.3.3 Size distribution

The respirable α-quartz used for the AFM measurements is normally used as a quantitative x-ray powder diffraction standard and hence, a well characterized sample. The NIST has used laser diffraction to characterize its size distribution. The mean particle diameter specified by the provider was 1.6 µm.

By measuring the maximum length and minimum width directly on the AFM images, a mean diameter could be evaluated for each particle by assuming a spheroid shape with circular section. A set of 8 images containing a total 130 particles has been analyzed. The mean diameter that has been determined is 1.47 µm with a spread of 0.54 µm. A separate size distribution analysis of a single image shown in Figure 3-11 has been performed. The large size of this image (30 µm) enables the investigation of 69 quartz particles at once. The retrieved mean diameter is of 1.28 µm with a spread of 0.41 µm. Both values determined by AFM are in the range of the value determined by laser diffraction. The typical distribution, as well as the experimental distribution for a single image and for all AFM images are shown in Figure 3-12.

To be able to estimate the embedment of the particles in the polymer, the height of the particle and the minimum width have been compared. Statistical analysis showed that the measured particle height represents 34 % $^{+}$/- 12% of the minimum particle width. By considering spheroids with circular sections, the particles are embedded by 2/3 in the polymer.

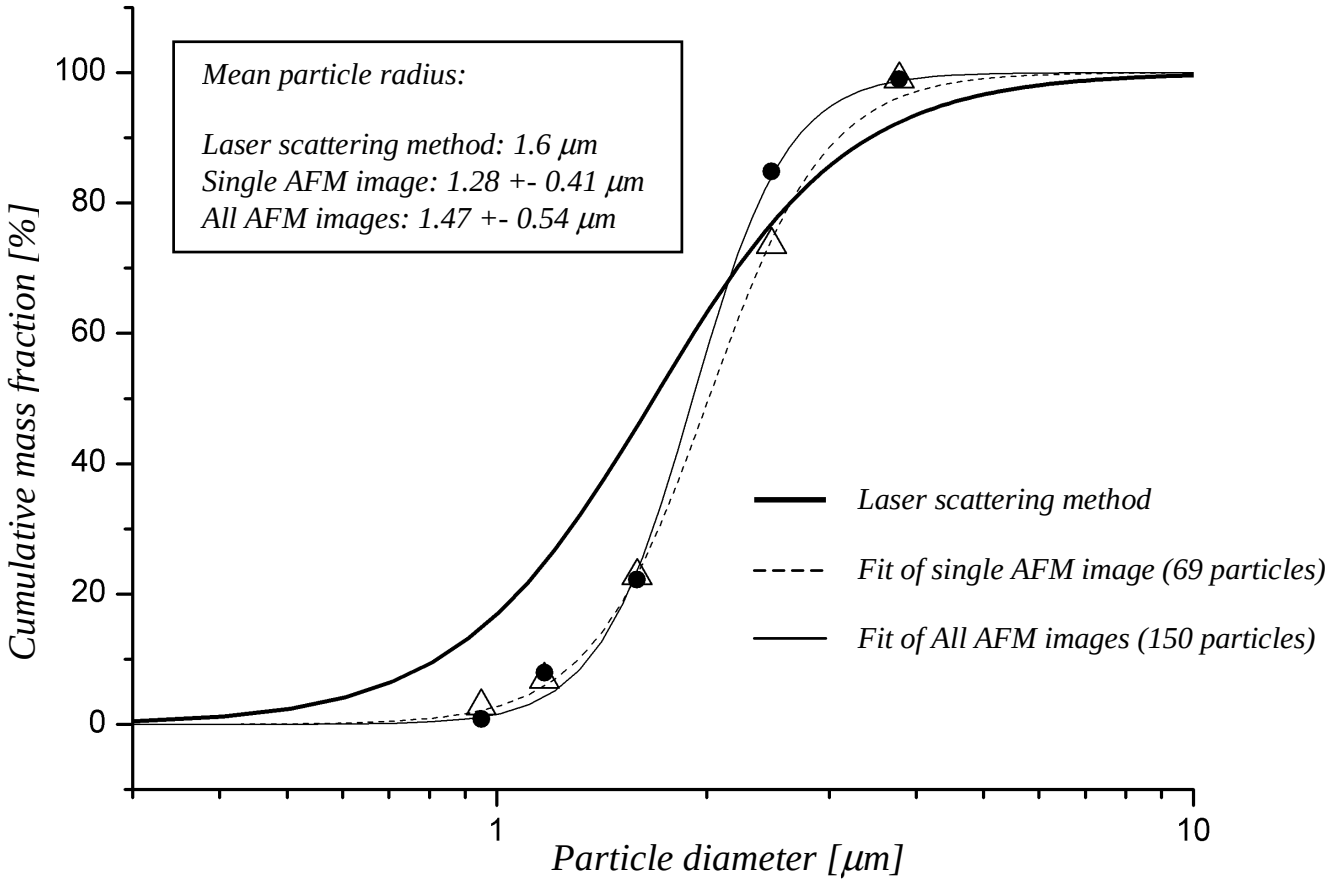

Figure 3-12
Particle size distributions of the α-quartz particles expressed as cumulative mass fraction.

3.2.3.4 JPEG compression

The flight software described in § 2.5.1 is based on different routines for autonomous measurements. In particular, the routine *AFM_Autozoom* will analyze the information of a recorded image by using the JPEG compression algorithm implemented on the lander computer.
JPEG compresses the picture by intelligently removing information to reduce the file size. The compression scheme divides the image into 8 x 8 pixel squares and uses a discrete cosine transform (DCT) and quantization to round off changes in brightness and hue. For our application, as the changes in brightness correspond to a change in height, this algorithm will assign a constant height to areas with small topographical variations.

The *AFM_Autozoom* algorithm will then analyse the data of the JPEG algorithm and choose the least compressible sub-area as target for the next image. Executing this zoom algorithm will prevent from selecting a sub-area with very little topographical changes.
To be able to validate this procedure, which has not been programmed and tested to this date, a typical AFM image of particles has been analysed. The chosen AFM image has a size of 8.2 µm and depicts a total of 9 particles ranging in size from 1.1 µm down to 260 nm in diameter (see Figure 3-13). The image is divided into 16 sub-areas, which corresponds to a nestratio for the zoom parameters of 4. A slight measurement error present in one of the scan lines crosses a particle at the bottom of the image. Such an abrupt topographical change can be induced by a loose particle or a tip crash and is therefore, depending on the measurement technique and the substrate, relatively frequent.
The compressibility of an area with measurement errors is much lower than for a clean area. Therefore, the sub-areas N°13 and 16 of Figure 3-13 have a bigger size than sub-area N°5, which in a clean-image case, would have been the least-compressible area. Using the autozoom algorithm in its present state bears the risk to the select a sub-area with measurement artefacts instead of particles.

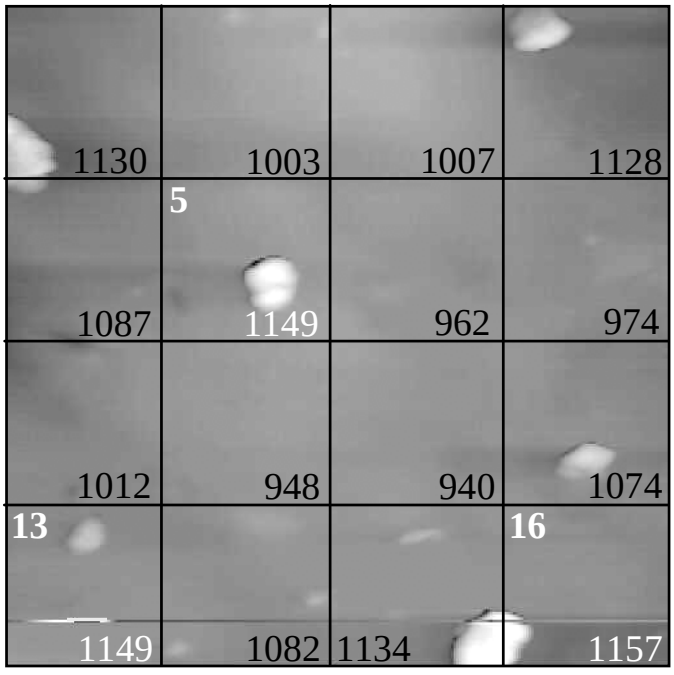

Figure 3-13
Compressibility of sub areas of an AFM image.The image has a size of 8.2 by 8.2 µm and a height of 450 nm. The size of each sub-area is expressed in Bytes. The least compressible area corresponds to field N° 16. Without the measurement error in fields 13 to 16, the sub area N°5 would have been the least compressible.

3.2.3.5 Measurement of scratches

Nanoscratch techniques are widely used to evaluate the mechanical and wear behavior of thin films. It provides a simple and rapid mean to assess the scratch resistance and adhesion of a protective layer [25]. These techniques rely on indentation measurements and the calculation of hardness coefficients determined by analytical formulas. Coefficients called Rockwell, Brinell or Vickers hardness can be derived from these indentation experiments. On a more empiric scale, the Mohs hardness test consists in scratching minerals with different hardness against each other to assess the harder of the two. The primary goal of the scratch experiments performed on the MECA experiment is to identify materials by their hardness. The ability to measure scratches with the FAMARS AFM is therefore of primary importance. To create the scratches on the previously described aluminum substrate, the quartz particles have been spread over the aluminum layer and rubbed against it with the edge of flat tweezers coated with Teflon.

The measured areas present several scratches and indentations with different orientations. As no particular care of the scratch direction was taken when rubbing with the tweezers, this observation could be expected.

The depth of the scratches varies from a few nanometers up to 150 nm. The width to depth ratio stays at a constant value of 6 for all the measured scratches. Figure 3-14 shows two AFM images of the same area representing several scratches produced by the quartz particles. Particles still present on the substrate during AFM investigations were simply pushed out of the scan area like it has been observed previously when performing static mode measurements. The flat aluminum substrate presents insufficient adhesion to immobilize the particles.

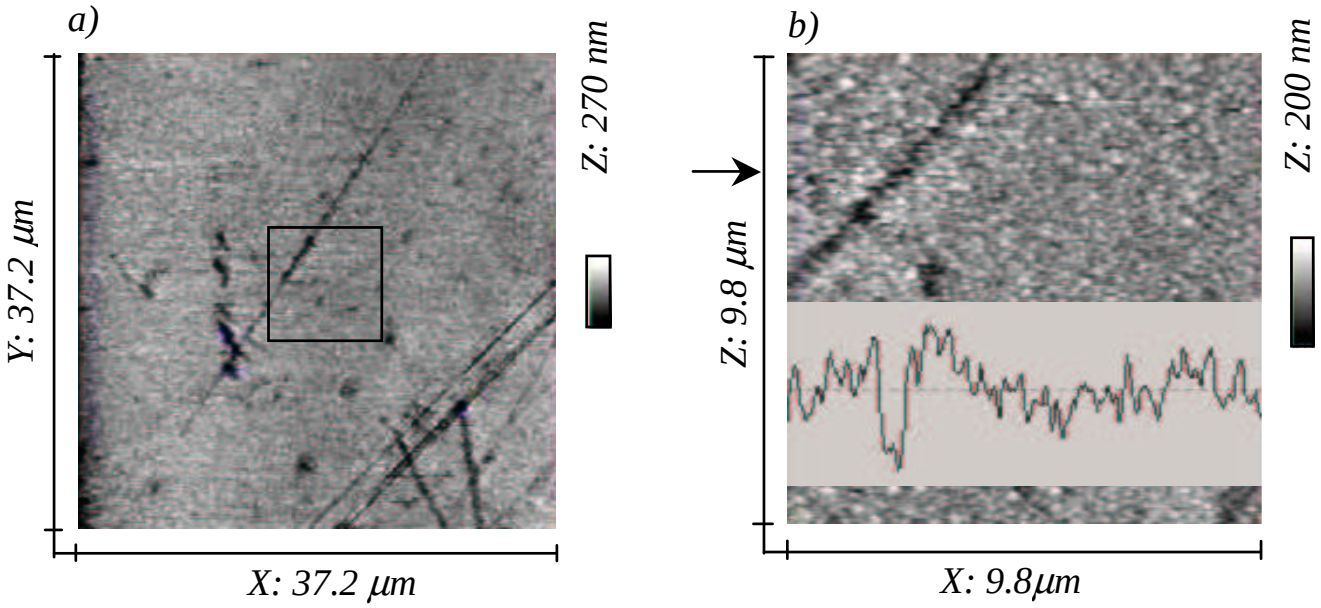

Figure 3-14

AFM images of scratches produced by the quartz particles. Figure b) is a zoom in the center of figure a). The cross section shown in figure b) is located at the position of the small arrow. The scratch has a width of 500 nm and a depth of 80 nm.

3.2.4 Reverse imaging

3.2.4.1 Tip contamination

While measuring quartz particles present on a substrate, the AFM tip can be contaminated by loose particles. In most cases, this contamination is due to electrostatic attraction. Since the electrical potential of the tip can be changed, these effects can be partially compensated, but not completely excluded. Additionally, the direct contact between the AFM tip and a particle can produce a tip-crash that will push the tip into the sample surface, which can lead to the contamination of the whole cantilever. Figure 3-15 shows SEM images of a contaminated cantilever and tip.

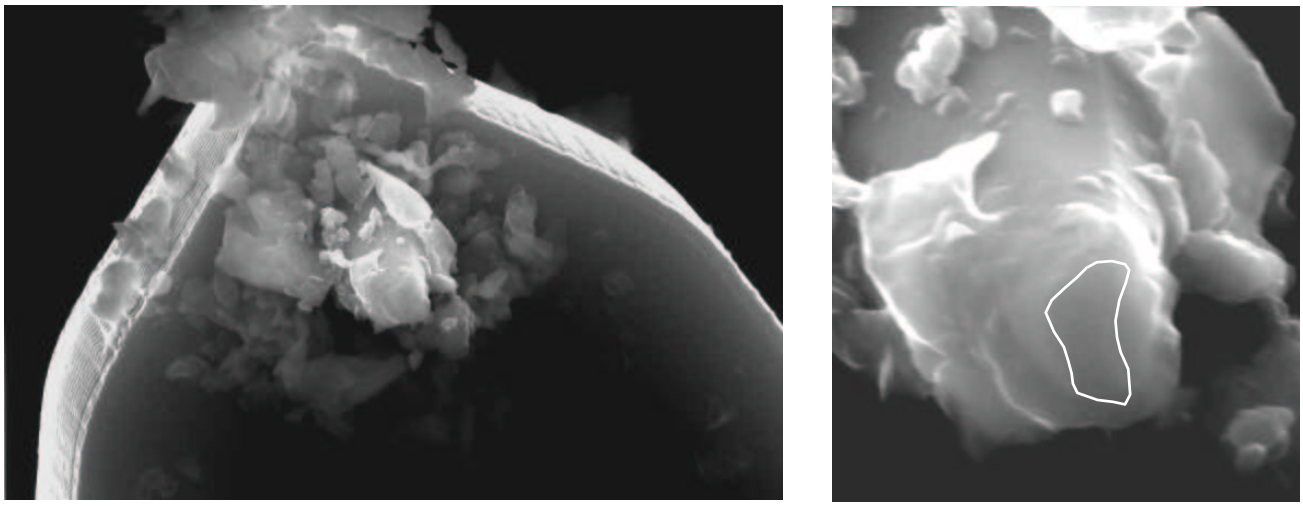

Figure 3-15
SEM images of a cantilever contaminated with quartz particles. The partial shape of the particle located at the silicon tip apex highlighted in white corresponds to the particle measured by AFM shown in figure 3-17 (rotated by 180°).

3.2.4.2 Mass measurements

When a tip contamination has occurred, the total mass of the cantilever is slightly changed due to the additional particle sticking on the tip and cantilever. This is translated in a reduction of the resonance frequency of the cantilever. The following analytical formula describes the relation between the change in mass Δm and the initial frequency f_1 and final frequency f_2 [26].

$$\Delta m = \frac{K}{0.72\pi^2}\left(\frac{1}{f_1^{\,2}} - \frac{1}{f_2^{\,2}}\right)$$

Δm: Mass change
K: Force constant of the cantilever
f_1: frequency without additional mass
f_2: frequency with additional mass

Using the values for the cantilever force constant and resonance frequency determined in table 2.1, the sensitivity to a mass change on the cantilever is 20 picograms per Hz. Knowing the resolution of the PLL frequency detection, the minimum detectable mass change is 2 picograms, which would correspond to 2 individual quartz particles with a diameter of 1μm.

3.2.4.3 Reverse-imaging principle

When a tip is contaminated, the AFM image quality is significantly deteriorated by tip convolution (see Figure 3-3). However, the scientific impact of images produced with a contaminated tip can still be of great importance. It is useful to reverse-image the contaminated tip in dynamic mode by using the tip-calibration sample shown in Figure 3-5. As the curvatures of the tips present on this sample are much smaller than the curvature of the particle on the AFM tip, the particle itself will be imaged repeatedly. Figure 3-16 illustrates the described principle.

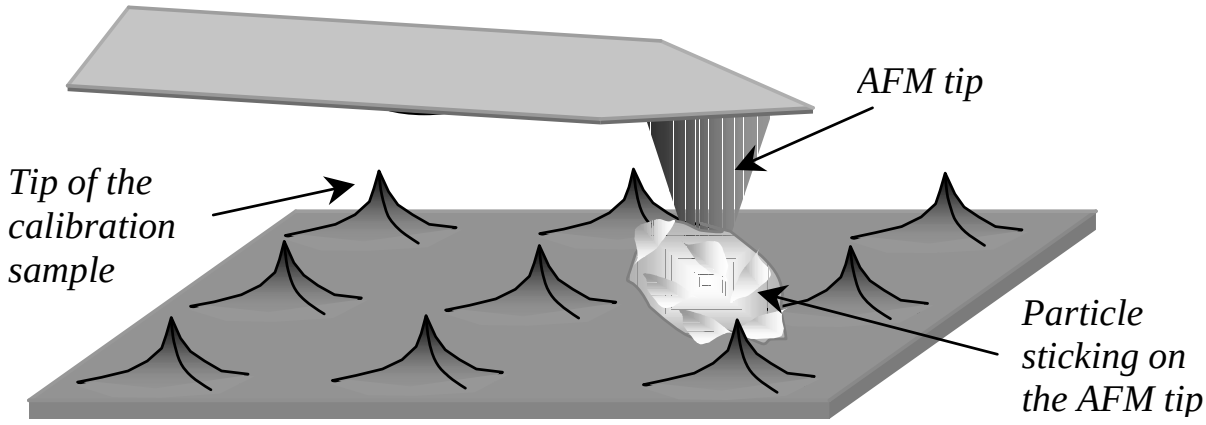

Figure 3-16
Principle of reverse-imaging a contaminated tip on a tip calibration sample.

The advantages of the repeated imaging of a single feature are as follows:

- The X, Y and Z calibration of the particle is directly present on the image since the periodic spacing between the tips as well as their height is known.
- As the tips of the calibration sample are displayed in an orthogonal configuration, distortion of the image produced by the scanner (see Figure 3-5 b) can be identified immediately and corrected by image processing techniques.
- By analyzing the correlation of the repeated shapes, an optimal particle shape can be determined which will take into account bad tip curvatures of the calibration sample.

Figure 3-17 shows AFM measurements of the tip calibration grid measured with a contaminated tip. The reverse-imaged particle is the same as the one shown in the SEM image of Figure 3-15. Depending on the actual height of the calibration tips, the reproduced particle will be imaged further down and will therefore have a less high topography. Replicas produced by an array of smaller calibration tips are highlighted by a black circle. The average height of the calibration tips is 800 nm.

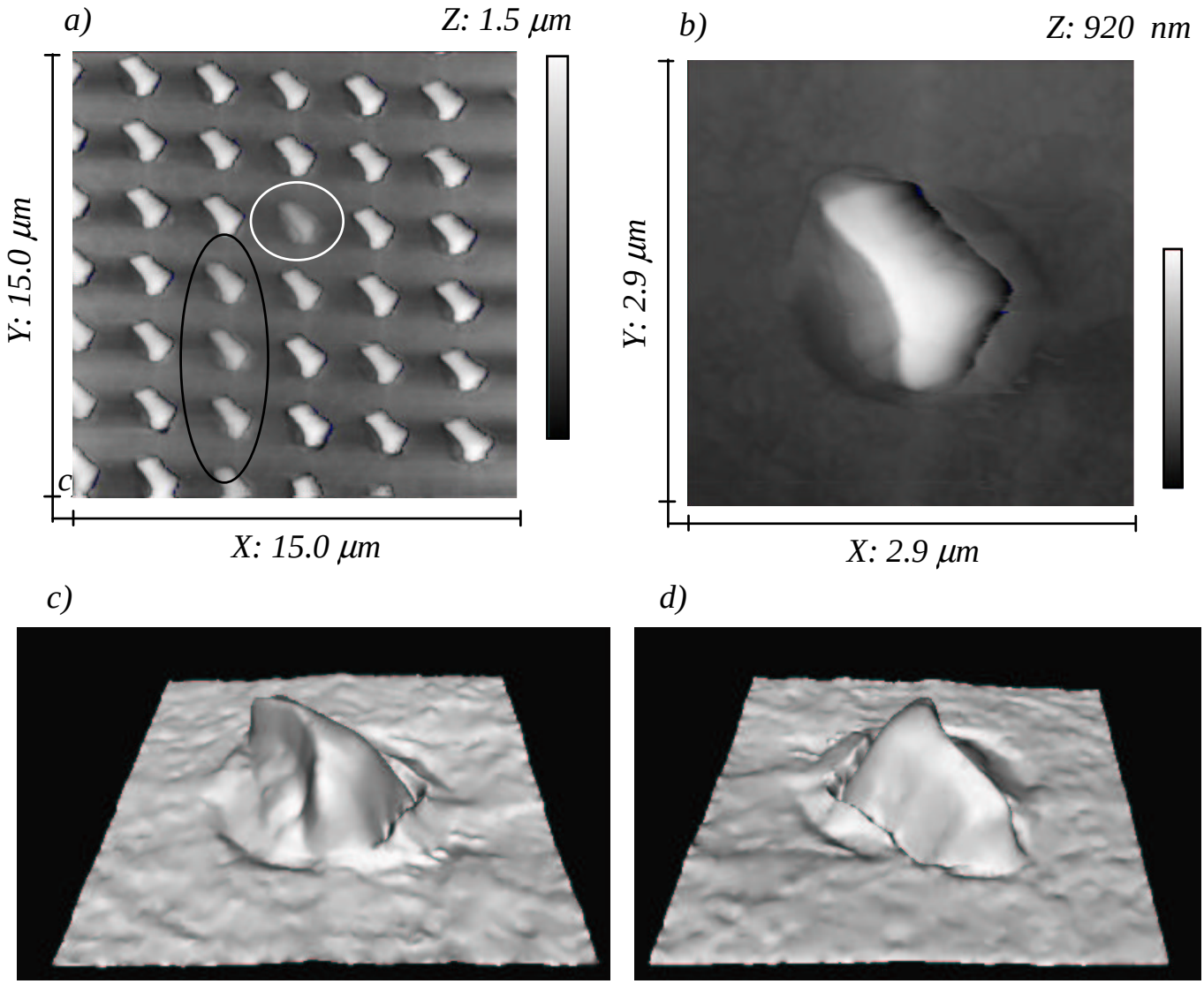

Figure 3-17

Dynamic mode measurements of a tip calibration sample measured with a tip contaminated with a quartz particle. Figure a) shows repeatedly the particle sticking on the AFM tip. Less high calibration tips produce features with less contrast (black circle), and blunt apexes produce fuzzier replicas (white circle). Figure b) shows a zoom of a typical replica. Figures c) and d) show 3-dimensional representations of the same particle.

The fuzziness of one of the replicas of Figure 3-17 a) is a result of a blunt tip of the calibration sample. This feature is highlighted by a white circle. The resemblance of the remaining replicas consolidates us in the assumption that the particle sticking on the AFM tip has exactly the shape as displayed.
In a more "terrestrial manipulation", which will probably not be possible in an autonomous operation mode on Mars, the orientation of the measured particle could be changed. By executing an approach procedure in static mode, the particle has been slightly moved relatively to the AFM tip. It was then re-images in dynamic mode. Thus, the same particle could be imaged under a new angle. These measurements helped to build a 3D micro-object model based on alignment of overlapping parts [27].

3.2.4.4 Effect of the calibration tip shape

Ideally, the exact reproduction of the features present on the AFM tip apex would be produced by scanning "dirac-like" pins with finite height. Since the tips of the calibration sample have shapes with finite dimensions, their effect on the particle shape by convolution is non negligible.

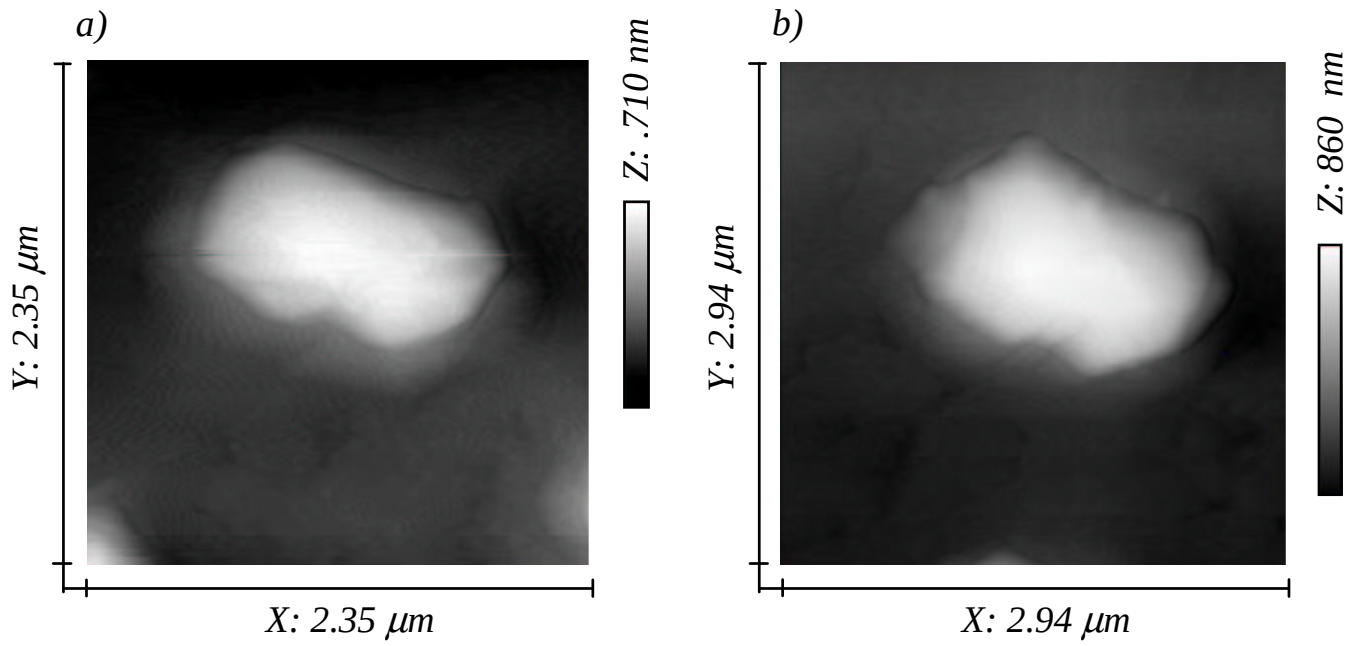

Figure 3-18
Shape of a particle sticking on the AFM tip measured with 2 different alignments of the calibration sample. The protrusions produced by the tip edges of the calibration sample visible in both images are not located in the same regions.

To be able to analyze the effect of the tip shapes, the relative alignment between the calibration sample and the AFM tip has to be changed to produce images that present different convolution patterns. This can be easily experimented by rotating the calibration sample and record another image. Figure 3-18 shows two images taken before and after rotating the calibration sample by 45°.
It seems that the sharp edges present on the tips of the calibration sample have a fairly large effect on the outline of the particle shape. These edges, generated during the fabrication process of the tips (see Figure 3-5 a), mimic small protrusions at regular angles around the particle. Depending on the particle shape itself and its orientation relative to the tip edges, these protrusions will be more or less pronounced and located differently around the particle periphery.
A deconvolution software[1] taking into account the tip curvatures of the tip calibration sample can help to correct artifacts to a small amount. However, the deconvolution algorithm does not take into account the sharp edges of the tips.

3.2.4.5 Tip cleaning

The main reason evocated for the particles to stick to the AFM tip is electrostatic charging. This phenomenon is relatively uncontrollable since many factors like substrate conductivity, particle properties and cantilever potential influence the charging behavior. Thus, once particles have been caught by the AFM tip, it is rather difficult to get rid of it by using autonomous procedures. The only parameter that can be adjusted is the potential of the cantilever, which will eventually repel the particles from the tip. However, this adjustment has been tried several times without producing satisfying results.
Mechanical interaction between the contaminated tip and a relatively rough surface can be used to free the tip from contaminations. By scanning over a calibration grid in static mode, the lateral interaction between the tip and the surface is increased which will eventually push the particle from the tip apex. Figure 3-19 shows an AFM image during which the tip has been cleaned by increasing the interaction force in the middle of the image.

[1] µ-mash Deconvo, www.siliconmdt.com.

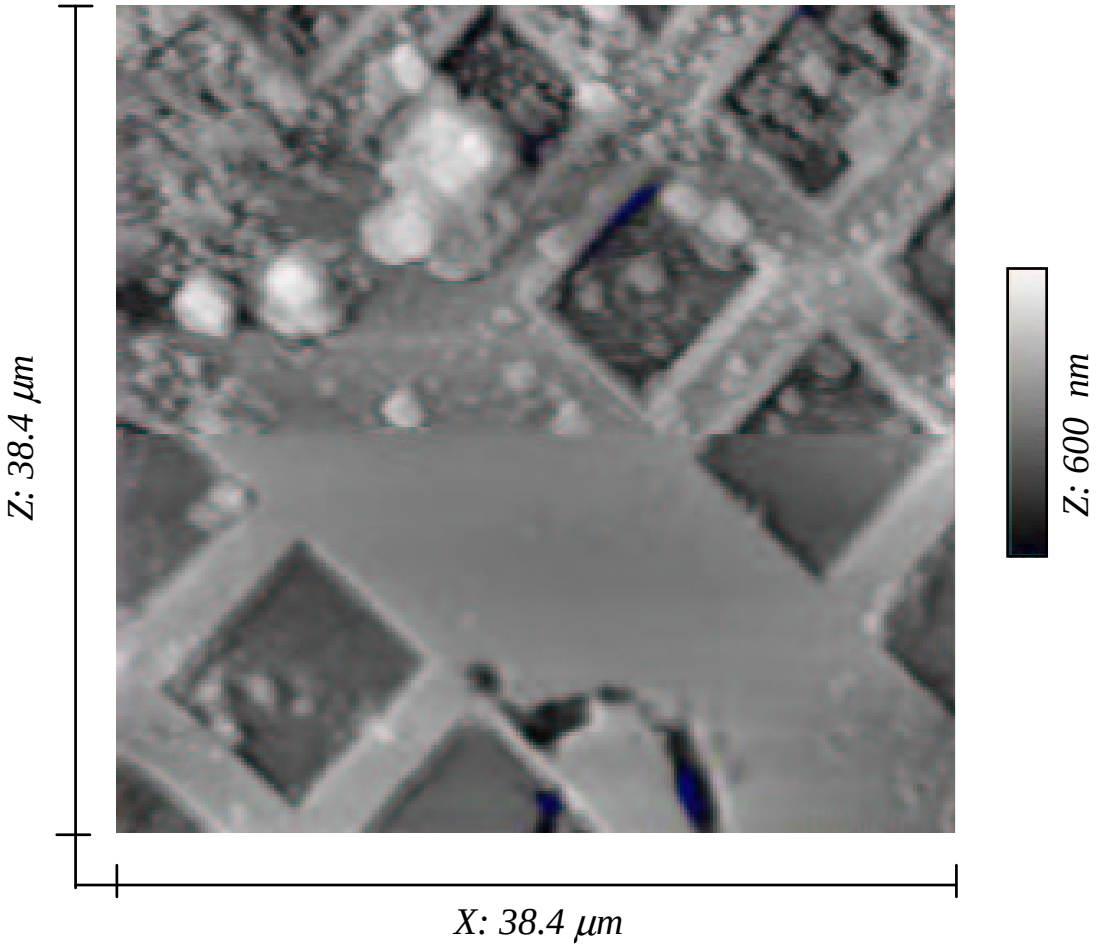

Figure 3-19
Static mode image of the calibration grid partially taken with a quart-contaminated tip. The image has been scanned from top to bottom. In the middle of the image, the contact force between the tip and the surface has been increased. Thus, the particle sticking on the tip apex has been removed, producing a cleaner lower part of the image, less influenced by convolution.

3.2.4.6 Particle fixation by polymer coated tips

As mentioned in the previous section, attaching particles to the AFM tip by using electrostatic effects is quite challenging and occurs in an uncontrolled manner. In order to benefit from the advantages of repeatedly reverse imaged features, a more reproducible technique for attaching particle to the AFM tip must be found.
Looking for a technique that could be implemented on the FAMARS AFM and lead to autonomous reverse imaging, the AFM tips were coated with a film of PMMA. The relatively high viscosity of a concentrated solution of this polymer could be used to coat the AFM tips by simply dipping the tips into the dissolved polymer. A first AFM image of the tip calibration sample has been taken with the PMMA coated tip prior to particle deposition (Figure 3-20 a). This image has been taken from bottom to top and

shows that the soft polymer surface is progressively flattened by the tip to sample interaction in dynamic mode.
The particle attachment to the polymer coated tip has been performed by approaching the coated cantilever to a substrate with deposited particles. This attachment procedure has been performed immediately after the polymer deposition to profit from the viscous properties of the polymer solution before complete evaporation of the solvents. Figure 3-20 b) shows the reverse imaged particle group sticking on the AFM tip apex. A total of 10 particles are visible within the first 800 nm imaged by the calibration tips. The particle diameters range from 370 nm up to 1.1 µm.

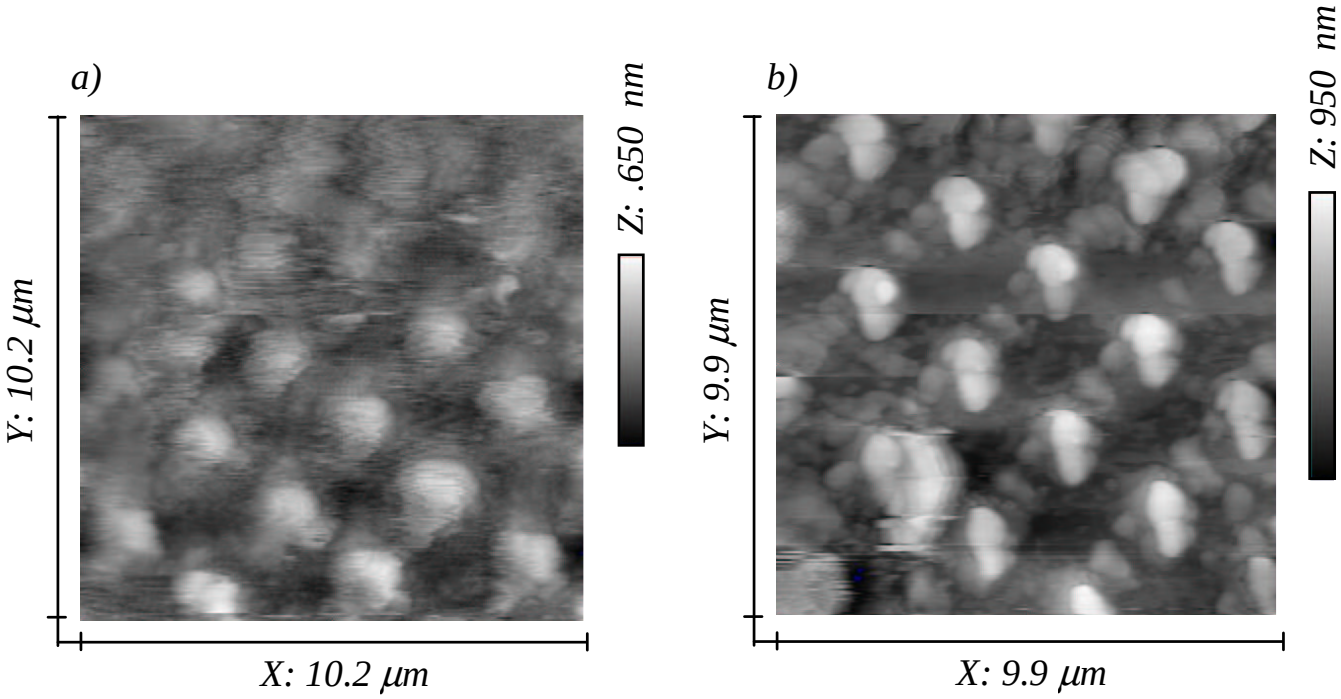

Figure 3-20

a) AFM image of the tip calibration sample recorded from bottom to top, taken with a PMMA coated tip prior to particle deposition. The progressive flattening of the topography is due to deformation of the polymer film at the tip apex.

b) AFM image of the tip calibration sample taken with a PMMA coated tip after particle deposition. The repeated features show a set of 10 particles with sizes ranging from 1.1 µm down to 370 nm in diameter.

3.3 Conclusion and discussion

3.3.1 Results based on direct imaging technique

It has been shown that the characterization of dust particles in the expected size range of Martian dust is possible with the FAMARS AFM. All valuable measurements have been performed in dynamic mode to reduce the lateral interaction forces with the particles. The following characteristics related to dust could be retrieved using the direct measurement technique:

- Shape: The shape of individual particles can be resolved by AFM. Due to the partial embedment of the particles in the PMMA polymer, only one side of the particle can be investigated. A reasonable minimum image size of 3 μm gives a resolution of 12 nm/pixel.

- Size distribution: The typical size distribution of the sample determined by laser diffraction could be reproduced by measuring the size of the particles on the AFM images. A large AFM image with 69 particles could already reproduce the overall size distribution (determined by AFM).

- Hardness: The scratch tests performed with quartz particles on an aluminum substrate demonstrated that hardness differentiation is possible and that the instrument gives good quality images of scratches.

- Mass: Modification of the resonance frequency of the cantilever due to particle contamination can lead to mass prediction of the particles sticking on the AFM tip. The resolution corresponds to the mass of two 1μm-sized quartz particles.

The recorded AFM images revealed that even with a perfectly sharp tip, particles with aspect ratios close to 1 could not be imaged correctly. As the opening angle of the silicon tips is of 35°, the periphery of the particles measured with these tips will not present sidewalls steeper than 17.5 ° due to tip convolution (see Figure 3-3). However, the surface structure on top the particles is only limited by the AFM tip curvature, which is about 10 nm.

3.3.1.1 JPEG compression

To validate the principle of autonomous selection of a sub-area with particles, a typical AFM image of particles has been analysed in terms of JPEG image compressibility. A slight measurement error induced by a loose particle can significantly alter the data size of a sub-area. The sub-area might therefore only be selected due to a measurement artefact instead of a real particle.
As a completely clean image is rarely produced, the use of this algorithm for sub-area selection needs to be reviewed and tested before being implemented.

3.3.2 Results based on reverse imaging technique

In addition to the direct measurement of particles placed on a substrate, a novel technique for creating repeated features of a single particle has been used. By scanning a particle-contaminated AFM tip over a tip calibration sample, the particle itself could be imaged repeatedly.

3.3.2.1 Reverse imaging review

Similar techniques based on reverse imaging have been used in the past to characterize tip shapes, without trying to attach other features of interest to it. Since the TGT01 sample was not available at those times, other high aspect ratio features were used like gold particles [28], InP columns etched by plasma [29], sharp pin-like structures present on copper films [30], and steep and high steps for STM measurements [31]. All of these examples had no calibration capabilities since the features had unknown heights and were arranged in a random manner on the surface.
The height calibration aspect of reverse-imaging has been reported 1993, when a sharp tip with well-known aspect ratio has been used as a z-calibration standard [32].
A particular example of a fullerene adsorbed tip measured in STM mode over a defect covered graphite surface is maybe the closest example to our application since the AFM tip itself was not the point of focus [33].
As the knowledge of the exact AFM tip shape is of great importance when interpreting AFM data, several algorithms for surface reconstruction and tip estimation have been developed [34,35,36].

- Calculating an image given a sample and a tip (dilation).
- Reconstructing the sample surface given its image and the tip (erosion).
- Reconstructing the tip shape from the image of a known tip characterizer (erosion)
- Estimating the tip shape from an image of an unknown tip characterizer (blind reconstruction).

3.3.2.2 Advantages and drawbacks

In a first step, particles could not be attached to the AFM tip in a controlled manner since only electrostatic forces held the particles. This phenomenon is relatively uncontrollable since many factors like substrate conductivity, particle properties and cantilever potential influence the charging behavior. The reverse imaging of particles fixed by electrostatic forces produced very satisfying results. A small modification of the orientation of a particle sticking on the AFM tip could be produced by a static approach to a hard substrate. The particle could then be imaged under a modified angle.
In a second step, particles could be attached to the cantilever using a PMMA coated AFM tip. By simply approaching the AFM to a substrate covered with particles, a more controlled and reproducible technique to place particles onto the AFM tip could be found. The images produced this way showed repeatedly a group of particles. Thus, reverse imaging can be used to characterize several particles on a single image.

Reverse imaging will be of great importance to increase the amount of relevant scientific data coming back from Mars. The repeated replicas of an individual shape displayed with known period and in an orthogonal configuration will give reliable information on the size of the feature and account for distortions produced by the scanner. In this way, a very detailed and extensive investigation of the particle shape can be done. Tip artefacts due to worn tips of the calibration sample will be easily detected by comparison with neighbouring features. As in many experiments based on multiple measurements, reverse imaging could be used to calculate the average and the standard deviation and other statistical properties of the repeated replicas.

The geometrical limitations of this technique are due to the height of the calibration tips and to their lateral spacing. If the reverse-imaged feature has a surface covering the first 800 nm of height larger than a square with 2.12 µm side length (dimensions applicable to the TGT01 grating), the topography will not be recorded correctly since multiple tips will be in contact with the shape sticking on the AFM tip. Figure 3-21 shows a schematic of the geometrical limitations.
The effect of the shape of the calibration tips has been investigated by changing the alignment between AFM tip and calibration grid. The same remarks as for the direct imaging observation can be made. Even with perfectly sharp calibration tips, the periphery of the particles will not be represented correctly due to the edges present on the side walls.
The software used to reconstruct the particle shape from the image of the tip characterizer TGT01 could not account for these edges. However, the surface structure on top the particles is only limited by the calibration tip curvature, which is, as for the AFM tip, about 10 nm.

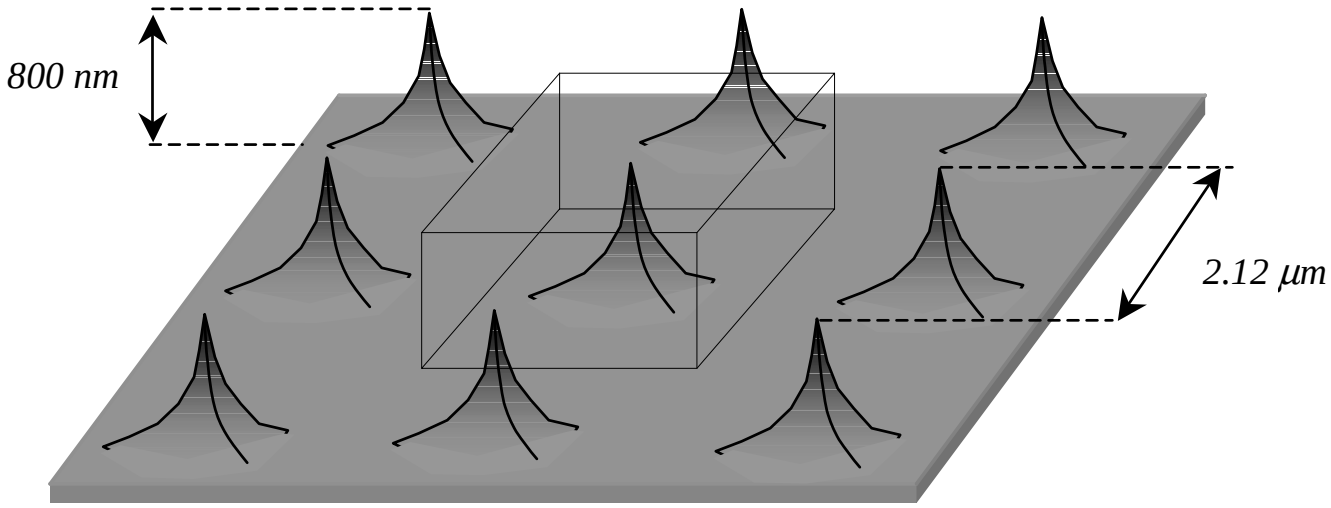

Figure 3-21

Schematic of the geometrical limitations for reverse-imaging a feature over a tip calibration sample. The wire framed box shows the maximum space that the feature sticking the AFM tip can occupy. The indicated dimensions are those of the µ-Mash sample TGT01.

3.3.2.3 Other applications of reverse imaging

In principle, all known SPM (scanning probe microscopy) applications could benefit from the advantages of reverse imaging. As most SPM probes rely on microfabrication to build the dedicated tips, the creation of an array of these tips would not be very difficult.

In this way, an array of SNOM tips could be fabricated to create repeated optical properties of a sample scanned over the array. The light would be collected by the SNOM tip on the cantilever side in transmission mode.

The principle of tip functionalization on the sample side for Biomolecule interactions has already been proposed by Drexler et al in 1990 [37].

3.3.3 Compatibility of measurements with operations on Mars

Some of the above mentioned results could only be achieved by using procedures not planned in the current Mars operation plan of the FAMARS AFM.

- The procedure of heating the substrate to “melt” the particles into the polymer is not implemented on the MECA experiment. The sample wheel of MECA uses a set of 7 substrates with different adhesion properties to find other means to fix the particles. Such properties have not been investigated within this work.

- The low temperature and outgassing properties of the polymer PMMA used to coat the substrates and the AFM tip has not been characterized in this work. A space qualified coating made of cured organo-siloxane gel has been proposed recently which could have the desired properties to act as a dust collector. Its sticking efficiency is much higher compared to common organic resins and polymers [38]. This sol-gel derived resin has not been used for the AFM measurements for availability reasons.

- The scientific measurements have been performed in a dry environment and at pressures equivalent to Martian conditions. The temperature however, was mostly kept between 10°C and room temperature. As the low temperature behavior (-10°) of the AFM scanner has been characterized in previous experiments (see § 2.6.2), it was chosen to avoid the distortional effects at lower temperatures while investigating the particle properties.

3.3.4 Further developments

The reported measurements show initial results of particle measurements. At the present status, the quality of the AFM images returned from Mars would be altered for the following reasons:

- Loose particles moved by the tip will not be imaged completely and provoke tip crashes.
- The opening angle of the AFM tips will limit the accuracy of the peripheral particle shape.
- The modified scanning behavior of the AFM at low temperatures will distort the AFM images and modify the inferred particle dimensions.

For the mentioned reasons, new means for particle immobilization, image calibration and tip quality must be fabricated and tested before being incorporated into the sample wheel of the MECA microscopy station. The following developments are proposed:

- Characterize the mentioned sol-gel-derived resin [38] and its capabilities to immobilize particles. Depending on its properties at low temperatures, a heating device might have to be incorporated, as it is the case for the PMMA coating.

- Fabricate and characterize special substrates for mechanical immobilization of the particles. The substrates shown in Figure 3-22 could significantly enhance the particle stability. As the substrate is vertically oriented during AFM measurements, the proposed high aspect ratio poles of figure a) or the holes of figure b) could also prevent particle from falling off the substrate. In

addition, as it is the case for the tip calibration sample, the geometrical arrangement of the features would provide X, Y and Z calibration marks present on every AFM image. The high aspect ratio of the poles in figure a) can be used as particle characterizers if a tip contamination has occurred. The main advantage is that the steep walls with circular section of these poles can be more easily used for shape reconstruction of high aspect ratio features like particles sticking on the AFM tip. Similar structures have been proposed to trap interplanetary dust particles during the ROSETTA mission [39].

- High resolution imaging on rough samples with high aspect ratios can be achieved by carbon nanotube (CNT) tips. These nanotubes can either be manually glued or grown onto the AFM tip.

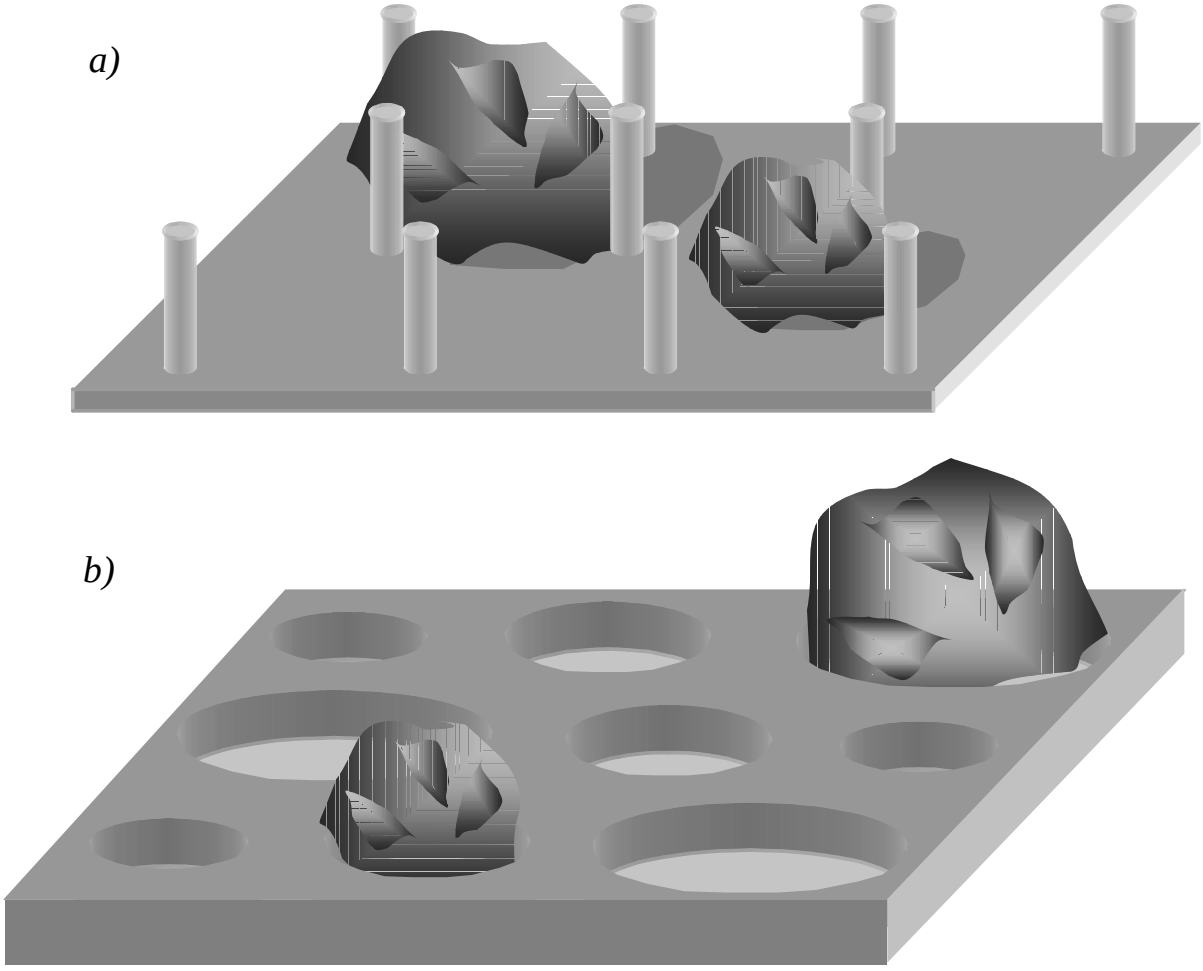

Figure 3-22

Particle immobilization and calibration samples

a) High aspect ratio poles placed in a well-defined orthogonal manner.

b) Holes with different diameters placed in a well-defined orthogonal manner.

3.4 References

1 : Stenhouse, J. I. T. and K. B. "Aerosol Deposition in Electrostatic Precipitators", Journal of Aerosol Science, **21**, 703, (1990).
2 : http://www.upstate.edu/pathenvi/basics/index.html
3 : K. R. Kuhlman, J. Marshall, N. D. Evans, and A. Luttge, "Multi-Technique Study of a Martian Aeolian Sand Analog", Proc. 32nd Lunar and Planetary Science conference, 1887.pdf, Houston, TX, (2001).
4 : K.R. Kuhmann, J. Marshall, N.D. Evans, A. Luttge, "Australian Red Dune Sand: A Potential Martian Regolith Analog", Field Trip and Workshop on the Martian Highlands and Mojave Desert Analogs, 4021.pdf, Las Vegas, Barstow, (2001).
5 : J. Marshall, K. Kuhlmann, R. Stevens, M. Meyyappan, "Study of Martian Aeolian Sand Analog with MECA Microscopy", 32nd Lunar and Planetary Science conference, 1265.pdf, Houston, TX, (2001).
6 : T.M. Zobeck, A. Amante-Orozco, "A New Dust Aerosol Analysis System", Proc. of the Dust Aerosol, Loess Soils and Climate Change meeting, Seattle, 89, (1998).
7 : K. Ramsey, "The Emergence of Triboelectric Technology", Pollution Engineering, September Issue, (1998).
8 : Joseph Leonelli, Dennis K. Killinger, William Vaughan, Michael G. Yost, "Optical Instrumentation for Gas Emissions Monitoring and Atmospheric Measurements ", SPIE Proceedings, **2366**, ISBN: 0-8194-1712-2, (1995).
9 : G. A. Landis, P. Jenkins, " Characterization of Settled Atmospheric Dust by the DART Experiment ", Proc. Mars 2001: Integrated Science in Preparation for Sample Return and Human Exploration, Houston, TX, (1999).
10 : G.A. Landis, P. Jenkins, D. Scheiman, C. Baraona, " MATE and DART: an Instrument Package for Characterizing Solar Energy and Atmospheric Dust on Mars ", Proc. Concepts and approaches for Mars Exploration, 6136.pdf, Houston, TX, (2000).
11 : G. A. Landis, P. Jenkins, J. Flatico, L. Oberle, M. Krasowski, S. Stevenson, "Development of a Mars Dust Characterization Instrument", Planet. Sci, **44**, 1425, (1996).
12 : S.F. Hviid, M.B. Madsen, H.P. Gunnlaugsonn, W. Goetz, J.M. Knudsen, R.B. Hargraves, P. Smith, D. Britt, A.R. Dinesen, C.T. Morgensen, M. Olsen, C.T. Petersen, L. Vistisen, "Magnetic Properties Experiments on the Mars Pathfinder Lander: Preliminary Results", Science, **278**, 1768, (1997).
13 : G.A. Landis, P. Jenkins, D. Scheiman, C. Baraona, « MATE and DART: An Instrument Package for Characterizing Solar Energy and Atmospheric Dust on Mars", Concepts and approaches for Mars Exploration, 6136.pdf, Houston, TX, (2000).
14 G.A. Landis, P.P. Jenkins, "Characterization of Settled Dust by the DART Experiment", Proc. Mars 2001: Integrated Science in Preparation for Sample Return and Human Exploration, Houston, TX, (1999).
15 : C.H. Schoen, D.L. Dickenshets, "Tools for In Situ Optical Microscopy and Raman Spectroscopy on Mars", Proc. Concepts and approaches for Mars Exploration, 6202.pdf, Houston, TX, (2000).
16 : L. Colangeli, MAGO consortium, "The Martian Atmospheric Grain Observer (MAGO) for In Situ Dust Analysis", Proc. Concepts and approaches for Mars Exploration, 6031pdf, Houston, TX, (2000).
17 : H. Arends, J. Gavira, J. Romstedt, B. Butler, K. Torkar, G. Fremuth, H. Jeszenszky, G. Coe, M. Yorck, "The MIDAS Experiment for the Rosetta Mission", Proc 9th European Space Mechanisms and Tribology Symposium, 67, Liège, Belgium, (2001)
18 : W. Barth, T. Debski, N. Abedinov, H. Heerlein, B. Volland, T. Gotszalk, I.W. Rangelow, K. Torkar, K. Fritzenwallner, P. Grabiec, K. Studzinska, I. Kostic, P. Hudek, "Evaluation and Fabrication of AFM Array for ESA-MIDAS/Rosetta Space Mission", Microelectronic Engineering, **57-58**, 825, (2001).
19 : K. Nakamura, W. Kloeck, W. Erfurth, M. Wiegand, "FE-SEM, AFM & TEM Study of Interplanetary Dust Particles for the Rosetta Mission", Proc. 31st Annual Meeting of the DPS, (1999).

20 : S. Gautsch, T. Akiyama, R.Imer, N.F. DeRooij, U. Staufer, Ph. Niedermann, L. Howald, D. Brändlin, A. Tonin, H.-R. Hidber, W.T. Pike, "Measurement of Quartz Particles by Means of an Atomic Force Microscope for Planetary Exploration", Surface and Interface Analysis, **33**, 163, (2002).
21 : Ken Westra et al., "Tip Artefacts in AFM Imaging of Thin Film Surfaces", J. Appl. Phys. **74**, 3608, (1993).
22 : Ken Westra et al., "AFM Tip Radius Needed for Accurate Imaging of Thin Film Surfaces", J. Vac. Sci. Technol. **B 12**, 3176 (1994).
23 : D. Nyyssonen, L. Landstein, E. Coombs, "Two-Dimensional Atomic Force Microprobe Trench Metrology System", J. Vac. Sci. Technol. **B9**, 3612, (1991).
24 : P. Grütter, W. Zimmermann-Edling, D. Brodbeck, "Tip Artefacts of Microfabricated Force Sensors for Atomic Force Microscopy", Appl. Phys. Lett., **60**, 2741,(1992).
25 : G. Wei, T.W. Scharf, J.N. Zhou, F. Huang, M.L. Weaver, J.A Barnard, "Nanotribology Studies of Cr, Cr2N and CrN Thin Films Using Constant and ramped Load Nanoscratch techniques", Surface and Coatings Technology, **146-147**, 357, (2001).
26 : H.P. Lang, R. Berger, F. Battiston, J.-P. Ramseyer, E. Meyer, C. Andreoli, J. Brugger, P. Vettiger, M. Despont, T. Mezzacasa, L. Scandello, H.-J Güntherodt, C. Gerber, J.-K. Gimzewski, "A Chemical Sensor Based on a Micromechanical Cantilever Array for the Identification of Gases and Vapours", Applied Physics, **A66**, 61, (1998).
27 : T. Jost, H. Hügli, "3D Modelling From AFM Measurements", Proceedings of Photonics West, *SPIE* Vol. 4275-08, San Jose, CA, (2001).
28 : S. Xu, M.F. Arnsdorf, "Calibration of the Scanning (Atomic) Force Microscope with Gold particles", J. Microscopy, **173**, 199, (1994).
29 : L. Montelius, O.J. Tegenfeldt, "Direct Observation of the Tip Shape in Scanning Probe Microscopy", Appl. Phys. Lett, **62**, 2628, (1993).
30 : F. Atamny, A. Baiker, "Direct Imaging of the Tip Shape by AFM", Surface Science, **323**, 314, (1995).
31 : G. Steiss, J. Vancea, H. Wittman, J. Zweck, H. Hoffmann, "Scanning Tunnelling Microscopy on Rough Surfaces: Tip-Shape-Limited Resolution", J. Appl. Phys, **67**, 1156, (1990).
32 : F. Jensen, "Z-calibration of the Atomic Force Microscope by Means of a Pyramidal Tip", Rev. Sci. Instrum, **64**, 2595, (1993).
33 : K.F. Kelly, D. Sarkar, S. Prato, J.S. Resh, G.D. Hale, N.J. Halas, "Direct Observation of Fullerene-adsorbed Tips by Scanning Tunnelling Microscopy", J. Vac. Sci. Technol, **B14**, 593, (1996).
34 : J.S. Villarrubia, "Algorithms for Scanned Probe Microscope Image Simulation, Surface Reconstruction, and Tip Estimation", Journal of research of the national institute of standards and technology, **102**, 425, (1997).
35 : P. Markiewicz, S.R. Cohen, A. Efimov, D.V. Ovichinnikov, A.A. Bukharaev, "SPM Tip Visualization Through Deconvolution Using Various Characterisers: Optimisation of the Protocol for Obtaining True Surface Topography from Experimentally Acquired Images", Probe Microscopy, **1**, 255, (1999).
36 : P. Markiewicz and M.C. Goh, "Atomic Force Microscopy Tip Visualization and Improvement of Images Using a Simple Deconvolution Procedure", Langmuir, **10**, 5, (1994).
37 : K. E. Drexler, "Molecular Tip Arrays for Molecular Imaging and Nanofabrication", J. Vac. Sci. Technol., **B9**, 1394, (1991).
38 : Y. Haruvy, "Space-Environment Aspects of Fast-Sol-Gel-Derived Glassy Materials and Coatings", Aerospace Materials Technology Testhouse, Internal report of the Austrian Research Centers, ÖFZS-W-0013, (1999).
39 : W. Fallmann, E. Cekan, A. Chalupka, E. Hammel, P. Hudek, H. Löschner, F. Rüdenauer, J. Schalko, G. Stangl, G. Stengl, "Microstructure Lithography", Gme internal report n° 12, (1995).

4. CONCLUSIONS

Since the first opportunity for this AFM to fly to Mars has been cancelled, this last chapter highlights the important arguments that will give the FAMARS instrument another ride to Mars.
The experience acquired and the results obtained during this work helped to draw several conclusions concerning the preparation of AFM operations on Mars and the scientific impact of the returned data.
The last sections are based on more philosophical reflections on NASA's faster better cheaper motto and the utility of AFM for future robotic and human exploration of Mars.

4.1 Technical achievements and scientific results

In a first assessment, bulkiness, high sensitivity and required interaction between the instrument and an operator render AFM unsuitable for planetary missions. However, MEMS technology combined with innovative design ideas allowed us to build an error tolerant system with functionality for addressing the challenges generated by a 9-month space travel and the Martian surface conditions.

4.1.1 Instrument characteristics

The initial desire to easily change the AFM probe in case of tip dullness or broken cantilever could be fulfilled by using MEMS fabrication techniques to build a sensor array out of silicon. The cleaving of the thick beams, which support each cantilever, could be executed several times without harming the remaining probes. The topographical sensing by piezoresistive detection significantly reduces the size of the instrument. Initial problems in dynamic mode measurement, induced by cross talk between the sensors of the array, could be resolved by a second-generation chip with cantilevers of different dimensions. The use of finite element simulations was very helpful for these improvements.
The AFM produces a maximum stroke of 53 μm in the X-Y plane while having a Z-range of 14 μm. Due to the necessary damping mechanism provided by viscous grease, the scanning behavior deteriorates at low temperatures. This problem can be partially overcome by increasing the scanning times, but remains a serious problem in the present design.
The protection circuit implemented in the electronics to prevent SEL's from harming the components has not been tested by means of a real latch-up produced by radiation,

which is very expensive to do. However, manually induced shortcuts, simulating a latch-up to some extent, immediately resulted in the expected power shutdown and reboot sequence.

4.1.2 Particle measurements

It has been shown that the characterization of dust particles in the expected size range of Martian dust (0.2 - 3 μm in diameter) is possible with the presented AFM. Advantages over commonly used dust analysis techniques are the much higher resolution of the individual particle shape and the small size and weight of the instrument.
During the period of investigation of almost 2 years, 350 images have been recorded with the FAMARS instrument. This database will be very useful when comparison with Martian images is necessary to draw scientific conclusions.
Physical characteristics related to dust like shape, size distribution, hardness and mass could be retrieved using two different measurement techniques: direct and reverse imaging. The first technique could be used to characterize the particle size distribution since a large number of particles could be imaged on a single frame. Direct imaging was also used to characterize scratches produced by the particles in order to assess their hardness.
Reverse imaging gives very reliable information on the shape of a single or a group of particles sticking on the AFM tip. This technique will be of great importance to increase the amount of scientific data coming back from Mars. The repeated replicas of an individual shape displayed with known period and in an orthogonal configuration, will give reliable information on the size of the feature, and account for distortions produced by the scanner. In this way, a very detailed and extensive investigation of a small amount of particles can be obtained.
All valuable measurements of particles have been performed in dynamic mode to reduce the lateral interaction forces with the particles. The characterization of blank surfaces and scratches is also possible in static mode.
Some of the mentioned results could only be achieved at room temperature and by using procedures not planned in the current Mars operation plan like particle fixation by a melted polymer.
The recorded AFM images revealed that even with a perfectly sharp tip, particles with aspect ratios close to 1 could not be imaged correctly. The AFM tips and the tips used to reverse-image the particles have both a finite opening angle and present edges along their sides, which induce artifacts on the recorded particles shapes. However, the surface structure on top of the particles is only limited by the AFM tip curvature, which is about 10 nm.

4.1.3 Preparation of Martian operation plan

4.1.3.1 Telemetry and timing

By taking into account the parameters influencing the data volume like image resolution, number of recorded channels, number of subsequent images and compression ratio, a data size of 1Mbyte per investigated area has been obtained.
The observations made on the particle behavior during AFM measurements are of great importance for building the operation plan on Mars. Considering the factors that influence the measurement time of an image like its size, topography and surface properties, the average time to fully investigate one area will be 2 hours.

4.1.3.2 Autonomous operations

A command dictionary for autonomous AFM operation has been created. Two command levels with different complexity can be distinguished: block level commands and high-level commands.
Block level commands will permit the quick preparation of sequences by putting together operational blocks. Typical examples of block level actions are: performing a health check, approaching the sample to the instrument and taking an image with specified size and measurement parameters.
High-level commands have been created to permit a safer imaging and to increase the scientific relevance of the images. In a first procedure, this is achieved by analyzing the surface topography prior to scanning the whole image to determine its dimensions and adapting the scan range to the physical limitations of the scanner. Subsequent images with reduced scan sizes can then be generated automatically.
A special sub-routine of a high level command has been created to smartly select a sub-area with particles. This procedure relies on JPEG compressibility. By analyzing a typical AFM image with particles, this subroutine could not be validated since topographical artifacts, frequently present on AFM images of dust particles, alter the compressibility of a sub-area. The selection of a sub-area by this algorithm must therefore be optimized.
The routines for autonomous operation have not been programmed to this date. Due to the cancellation of the 2001 opportunity for MECA, software developments have been stopped before completion. Thus, most of these sequences have not been tested in practice.

4.1.4 Further developments

At the present status of the instrumentation, the genuine topographies of Mars samples, as they would be returned from Mars, would be affected by the measurement concepts and by technical limitations. To improve the image quality at low

temperatures and the reliability of particle measurements, several developments are proposed.
Better ways to immobilize the particles on the substrate or the AFM tip would be to incorporate a heatable device both on the AFM tip or on the substrates of the MECA sample wheel. Both techniques will require additional characterization of the heatable resin. The particles could also be fixed by mechanical poles or holes etched in a special substrate.
The growth of carbon nanotubes on the AFM tip apex could significantly increase the lateral resolution of the particle shape and minimize convolution effects.
Additional information on the particle hardness relative to the substrate could be obtained by implementing an energy-loss measurement mode comparable to "phase contrast"[1] imaging.
The distortions of the scanning field could be improved by finding a damping grease with optimized thermal properties. As the temperature range for storage and operation on Mars is large (-120° to 50°), it may be difficult to find a suitable damping substance. An active linearizer to completely overcome this problem would necessitate a complete design review of the scanner. Depending on the time frame of a new flight opportunity, this option will be privileged.

4.1.4.1 Field testing

The FAMARS AFM has been implemented in the MECA microscopy stage and preliminary AFM measurements on calibration samples have been performed. However, except for the approach procedure, no autonomous measurements have been performed, as the flight software has not been programmed to this date.
In a first step, the testing and optimization of the measurement protocols needs to be performed to suppress any human interaction with the AFM and MECA. Extensive field-testing will involve measurements of soil samples (Mars equivalent sand, quartz, clay) using the whole system such as robot arm, sample wheel, optical microscope and AFM in order to validate the autonomous procedures. To evaluate the effects of windy environments on the sensitivity of the instrument, the complete lander platform would have to be involved in the field-testing.

4.2 Scientific impact of measurements

The presented instrument allows investigations on Martian dust particles present in surface soil and atmosphere. Properties like shape, size distribution, hardness, and mass can be determined with high accuracy.
The returned data will give new insights into the history of Martian geology. As described in the first chapter, predictions on the mineralogical composition of the airborne dust relies on theoretical diffraction models where the particles size

[1] Denomination used by Digital Instrument.

distribution plays a major role. Until this day, this characteristic is non-deterministic and, throughout the last 30 years of scientific research, has undergone relatively large variations as illustrated in table 1-2 of page 23. Scientific results returned by FAMARS will start new investigations in this field and limit the speculations on mineral composition.
The risks for future human explorers of the planet will be accurately assessed by the set of instruments onboard the payload MECA. The above mentioned dust properties and in particular the presence of quartz particles in the respirable size range will be evaluated by the FAMARS AFM. This study will lead to important conclusions for the design of exploration equipment and for human safety measures.

4.3 FAMARS project timeline

The 1-year development phase of the FAMARS instrument experienced NASA's faster better cheaper philosophy [1]. The project lead could profit from its academic environment, which enabled very close collaboration with the industrial partners of the project and the respect of the delivery schedule.

- August 1998 – September 1999: AFM design and building phase
- October 1999 – March 2000: AFM implementation into MECA
- April 2000 – December 2001: AFM characterization under Mars equivalent conditions and establishment of a Mars equivalent sample database
- *(April 2001: Launch of Mars surveyor)*

Until the AFM delivery date, MECA was planned to be launched in April 2001 with the Surveyor lander. If this mission had been kept on schedule, only a year of extensive testing of the payload would have been available before launch. Considering the almost-2-years spent on the presented results, the acquirement of equivalent results with the original time schedule would have required a much bigger effort than the Swiss or NASA's financial support would have permitted. Even if this ongoing effort has been performed after the cancellation of MECA's flight opportunity, and thus submitted to less time pressure, the previous remark is still valid.
In addition, as mentioned in the previous section, technical optimizations, design reviews and extensive field testing without any human interaction will be required in the future to increase the chance of getting valuable scientific data back from Mars. These additional developments will require further efforts based on more time and/or money.
The blame for this incompatibility between fast, cheap and good cannot be put on anyone on the FAMARS or the MECA team. For a visionary proposal to even have a chance of becoming a payload for a Mars mission, the same "3 characteristics" must

be admitted to be compatible. Or in other words, the teasing of a selection committee has the absolute priority.
The additional time and money might be available now, since the chances for another opportunity for MECA or a MECA follow-on are very realistic. This will also enable the AFM characteristic adjective to change from good to best.

4.4 AFM in robotic and human exploration of Mars

The robotic exploration of Mars with Mariner 9, the Viking missions, Pathfinder and Mars global surveyor has followed a path with little progression in terms of mission complexity and science yield. However, thanks to these missions, a global view of the planet's surface conditions could still be obtained. Future exploration plans by robotic in-situ missions, sample return missions and human exploration will focus on the detailed characterization of the geologic diversity. The advantages and drawbacks of AFM for all three exploration steps are highlighted in this last section.

The progression in knowledge along with past robotic missions is mostly due to improved sensitivity rather than to novel scientific instrumentation. The lack of will to take higher risks on payloads has driven the selection procedures for the last 10 years. Orbiters always carried infrared spectrometers while landers were mainly equipped with panoramic imagers. Today, sample return missions and human exploration plans have been set back. Small in-situ missions will mark the next ten years of Mars exploration. By implementing never before flown instrumentation, new scientific data could be obtained to answer questions that have been raised by the experimental results of previous missions. The advantages of using AFM on a robotic mission for gaining information on the dust and soil properties of Mars have been highlighted in this work, and will hopefully be understood.
Future Mars instrumentation will rely on extreme miniaturization, which is made possible by MEMS technology. As the FAMARS case is a good example of implementing silicon technology with traditional mechanical surrounding and thus, for overcoming the main concerns related to space MEMS, it might give the necessary push forward for other MEMS components to be flown on commercial satellites or on planetary missions.
Even if the in-situ type of analysis seems to be the next best step before sample return missions, conclusions drawn from remote analysis of samples will never have the same relevance as Earth-based laboratory analysis. The geological history of Earth has been determined in 200 years of rock analysis. These investigations with powerful instrumentation like AFM, SEM, TEM, EDX, X-ray diffraction or isotopic dating did not limit itself to bulk properties but focused on the internal chemical structures of the minerals. The preparation and analysis of samples with the mentioned methods mostly requires heavy machinery impossible to implement on small robotic missions.

In addition to the limitations due to sample preparation, in-situ instruments can show diminished capabilities compared to their terrestrial analogs. On the engineering side, the reduction in size, weight and power consumption can lead to lower resolutions and poorer sensitivity. On the operation side, the versatility and repeatability of the measurements are diminished by the required autonomous procedures. Scientific knowledge generally comes by iterating the measurements of a single sample and by focusing on different aspects that can difficultly be preprogrammed. Our understanding of Mars will therefore stay limited until samples of the planet can be studied in terrestrial laboratories.

Tomorrow, samples of Mars will be brought back to Earth. The main goal of such a mission will be to return samples of relevant sizes while preserving its scientific integrity. These samples will have unique value since scientists worldwide will study them using the most powerful analytical instruments available. The capabilities of the presented AFM can then be extended to the study of atomic structures, magnetic force microscopy or Raman spectroscopy. However, samples brought back from Mars will stem from one or a few sites that will never reflect the geological diversity that has been inferred by remote sensing. The only way to bring the historical knowledge of Mars to level with Earth's is to send humans to Mars.

Someday, humans will walk the surface of Mars. This will provide an unprecedented opportunity to use the human mind to understand Martian processes and history with much better detail than previously assessed by robotic missions. Answers to fundamental scientific questions will be provided by human field explorations and by sampling and analysis of Martian material by compact and powerful instrumentation. A prototype of a manned science station called MarsLab has been recently proposed by the HEDS department [2]. Among other very promising experiments, MarsLab comprehends an AFM, which, in addition to characterizing the dust and soil, will assess the landing site's ability to preserve biological traces.

Whether it is today, tomorrow or someday, the FAMARS team looks forward to have its AFM on Mars!

4.5 References

1 : H.E. McCurdy, "Faster, better, cheaper, Low-Cost Innovation in the U.S. Space Program" 0-8018-6720-7, 208 pages, (2001).

2 : M.H. Hecht, C. McKay, G. Briggs, J. Connolly, "MarsLab: A HEDS Lander Concept", Proc of the Concepts and Approaches for Mars Exploration conference, Houston Texas, 2000

5. ACKNOWLEDGEMENTS

5.1 The FAMARS team

The achievements presented in this thesis are the result of an intensive collaboration with many research partners forming the FAMARS team. Without their help, this project would not have come to realization. I am indebted to all members of this team:

One person guided me through this project and represented a tremendous source of inspiration for my work. I deeply thank Dr. Urs Staufer for intense discussions, the creation of well-structured presentations, enriching travels, constant encouragements and for the transmission of his impressive knowledge in the field of Physics.
I'm very much indebted to Dr. Terunobu Akiyama. He designed the first generation AFM chips and guided me during the fabrication process in the clean room. I express my gratitude to him for all the precious hints he could give me.
Special tanks also go to my semester student Raphael Imer that spent four months recording AFM images with the FAMARS instrument. His contribution helped to stay on track with the very tight delivery schedule.
The scanner design and the manufacturing of scanner components has been the duty of the company Nanosurf in Liestal. They also were responsible for the software adapting for the FAMARS instrument. I would like to address my special thanks to Dominik Brändlin, Lukas Howald and Robert Sum for their help and advice. I wish Nanosurf to continue to be as successful in their new technological developments.
The space-qualified electronics have been designed, assembled and characterized by the electronics department of the Institute of Physics of the University of Basel. Without the skills of Hans-Rudolf Hidber and Andreas Tonin for electronic design and website mastering, the FAMARS project would not have had such an impressive success.
I am very grateful to Philippe Niedermann from CSEM for providing the diamond tips placed on the cantilevers of the flight instruments and to Chris Musil from PSI for cutting the overlapping edges with the focused ion beam.
I acknowledge the board of Swiss Federal Institutes of Technology for financial support through the Swiss Priority Program MINAST.

5.2 The MECA team

The FAMARS project enabled me also to work for four months at the Jet Propulsion Laboratory in Pasadena, California. I would like to express my deep thoughts to Tom Pike, his wife Philippa and his kids Aidan and Eleanor who gave me a warm welcome at their house during this period. Tom was a wonderful microcopy team leader and taught me how to live as an English man in America.
The MECA team also played a major role in rendering this Californian dream as enjoyable as possible. I owe thanks to Tom Meloy for a wonderful evening at Caltech's Athenaeum, Michael Hecht for his support and organizing dinner outings with the MECA team, Joel Rademacher (future astronaut and valuable sixflags magic moutain adviser), Lynn Cooper (sorry for insisting), Jason Feldman (LA Kings win and loose), Terry Friedman (don't worry about the software), Mark Anderson, Lisa Tatge, Ken Manatt, Sabrina Feldman (thank you for the wonderful trip to Joshua tree), Kevin Watson (thanks for the headphones and introducing me to LGL), Kjartan Kinch and Catherine Frandsen (did the Los Angeles galaxy won that day ?).

5.3 The SAMLAB group

During the period of my PhD, I was surrounded by an amazing group of people in Neuchâtel: the Sensors, Actuators and Microsystems Laboratory (SAMLAB) team. The special atmosphere in this group helped me greatly to achieve my goals. I especially would like to express my gratitude to the following people:
Prof. Nico de Rooij for offering me a research position in such a multidisciplinary team. He showed me his confidence in my capabilities by sending me to JPL and by offering me the opportunity to represent the group at various occasions.
I'm very much indebted to the SAMLAB technical staff: Pierre-André Clerc for DRIE etching, Massoud Dadras and Mireille Leboeuf for SEM pictures, Gianni Mondin for depositions, Pierre-André Künzi for e-beam lithographies, Claudio Novelli for computer issues, Sylviane Pochon for wire bonding, and all the other members of the technical team: Sylvain Jeanneret, Nicole Hegelbach, Sabina Jenny, Edith Millotte, and José Vaquera.
Special thanks go to Gian-Luca Lettieri and Arash Dodge with whom I've spent my complete education, starting from primary school at the age of seven until this very day as a PhD student in the SAMLAB group. During all theses years, they taught me to never forget the fun part of life. I hope that we'll have a start-up together someday…
The enriching experience of making crosswords has been brought closer to me by Laure Aeschimann. She was a close listener to technical and non-technical problems and certainly a bright ray of light in this group. Thanks for all the encouragements during this project!

My office colleagues with whom I shared a lot of emotions (Vincent Auger (I'm still not listening), Luca Berdondini (une petite clope) and Patrick Weber (Stealth Fighter)) are to be thanked as well as the other members of the SAMLAB group: Giovanni Bergonzi (beach volley guru), Danick Briand (KOH guru), Patrick Carazzetti, Laura Ceriotti (Lauralo ?), Laurent Dellmann (I enjoyed my diploma with you), Philippe Dubois (surfing in La Chaux-de-Fonds), Giovanni Egidi (lightly dressed at the Christmas party), Jean-Charles Fiaccabrino (exhibitions and webmastering), Olivier Guenat (my biggest swim fan), Maurizio Gullo, Fernando Herrera, Alexandra Homsy (same remark as for Giovanni E.), Sander Koster, Milena Koudelka-Hep (Malta was great), Andreas Kuoni, Eva L'Hostis (thanks for good advice), Jan Lichtenberg (Labview guru), Scharazede Mouaziz, Wilfried Noell (Astro guru and bagels lover), Thomas Overstolz, Phuong Quyên Pham, Sylvain Roth (a suivre …), Gregor Schürnann, Winston Sun, Kaspar Suter (nice piece of cake), Peter van der Wal, Sabeth Verpoorte (μTAS guru) and Michael Zickar.

5.4 Everyone else

Other extra-academic occupations helped me to refresh my "body and soul" and enabled me to never have just one log in the fire. I would like to thank all members of the Red-Fish swimming team of Neuchâtel for the intense work-outs and funny moments. I send my deepest respect to my actual swim-coach Christopher Morgan that woke the American fighting spirit in me. He made my swimming experience what it is today.

I would like to thank the teaching profession that took care of my education. For primary and secondary school: Mrs Ducommun, Mrs Martinet, Mrs Zingg, Mrs Robert, Mr Jeanneret, Mrs Chappuis, Mrs Jeannot, Mr Gentil, Mrs Hagelstein, Mr Fasnacht, Mr Thorens, Mr Fevrier, Mr Spichiger, Mrs Geiger, Mrs Quellet-Lanz, Mrs Renfer-Percassi, Mr Cachelin. For my highschool years: Marcel Maumary, Eric Bubloz, Christian Zülly, Philippe Gern, Denise Bovet, Jacques Bovet, Jean-Luc Bovet, Eric wessner, Mr Weber, Mr Bitterli, Mr Ketterer.

I owe my academic education to the following professors: Prof.F. Sigrist, Prof. U. Suter, Prof. Y. Baer, Prof. O. Besson, Prof. H. Beck, Prof. Collins, Prof. J.-L. Vuilleumier, Prof. P.-J. Erard, Prof. G. Süss-Fink, Prof. Jeannet, Prof. J.-P. Derendinger, Prof A. Shah, Prof. H. Hügli, Prof. R. Dändliker, Prof. H.-P. Herzig, Prof. F. Pellandini, Prof N.F. de Rooij, Dr. P. Seitz, Prof. C. Piguet, Dr. M. Degrauwe, Dr. N. Bui.

I deeply thank Annick Vautravers for her good mood and inexhaustible energy. Finally, I express my gratitude to my parents, who supported me during my studies and always showed interest in my research.

6. ACRONYMS

ADC	Analog to Digital Converter
AFM	Atomic Force Microscope (Microscopy)
APXS	Alpha Proton X-ray Spectrometer
CCD	Charge Coupled Device
CNT	Carbon Nano Tube
CSEM	Centre Suisse d'Electronique et de Microtechnique
CVD	Chemical Vapour Deposition
DAC	Digital to Analog Converter
DART	Dust Accumulation and Removal Test
DCT	Discrete Cosine Transform
DDS	Direct Digital Synthesizer
DRIE	Deep Reactive Ion Etching
EDL	Entry Descent and Landing
EDX	Energy Dispersive X-rays
EPF	Emission Phase Function
ESA	European Space Agency
EVA	Extra-Vehicular Activity
FAMARS	First AFM on MARS
FAMOS	FAst scanning probe Microscopes On Silicon
FPGA	Field Programmable Gate Array
GCR	Galactic Cosmic Rays
GRS	Gamma Ray Spectrometer
HEDS	Human Exploration and Development of Space
HMP	Haughton Mars Project
IDP	Interplanetary dust particles
IFP	Institute of Physics, University of Basel
IMP	IMager for Pathfinder
IMT	Institute of Microtechnology, University of Neuchâtel
IRIS	Infra Red Interferometer Spectrometer
IRTM	Infra Red Thermal Mapper
JPEG	Joint Photographic Experts Group
JPL	Jet Propulsion Laboratory
LED	Light Emitting Diode
LET	Linear Energy Transfer
MAE	Material Adherence Experiment
MAGO	Martian Atmospheric Grain Observer
MARIE	MArs Radiation Environment Experiment

MATE	Mars Array Technology Experiment
MCO	Mars Climate Orbiter
MECA	Mars Environmental Compatibility Assessment
MEMS	Micro Electro Mechanical Systems
MFM	Magnetic Force Microscopy
MGS	Mars Global Surveyor
MIDAS	Micro-Imaging Dust Analysis System
MINAST	Micro and Nano System Technology
MIP	Mars In-Situ Propellant precursor experiment
MOC	Mars Orbiter Camera
MPL	Mars Polar Lander
NASA	National Aeronautics and Space Administration
NIST	National Institute of Standards Technology
NS	Nanosurf AG, Liestal
OSHA	Occupational Safety and Heath Administration
PEL	Permissible Exposure Limit
PLL	Phase Locked Loop
PMMA	Polymethyl methacrylate
PSG	Phosphor Silicate Glass
PSI	Paul Scherrer Institut
SEL	Single Event Latchup
SEM	Scanning Electron Microscope
SEP	Solar Energetic Particles
SEU	Single Event Upset
SOI	Silicon On Insulator
SPM	Scanning Probe Microscopy
SRM	Standard Reference Material
STM	Scanning Tunnelling Microscopy
TEM	Transmission Electron Microscopy
TES	Thermal Emission Spectrometer
THEMIS	Thermal Emission Imaging System

7. PUBLICATIONS

Refereed articles

S. Gautsch, T. Akiyama, R.Imer, N.F. DeRooij, U. Staufer, Ph. Niedermann, L. Howald, D. Brändlin, A. Tonin, H.-R. Hidber, W.T. Pike, "Measurement of Quartz Particles by Means of an Atomic Force Microscope for Planetary Exploration", Surface and Interface Analysis, **33**, 163, (2002).

S. Gautsch, T Akiyama, N.F. de Rooij, U. Staufer, Ph. Niedermann, L. Howald, D. Müller, A. Tonin, H.-R. Hidber, W.T. Pike, M.H. Hecht, "Atomic Force Microscope for Planetary Applications", Sensor and Actuators, A 91, 321, (2001).

S. Gautsch, U. Staufer, "Un microscope sonde les poussières martiennes", Journal Ingénieurs et Architectes Suisses, **11**, 228, (2000).

U. Staufer, T. Akiyama, C. Beuret, S. Gautsch, W. Noell, G. Schürmann, C. Stebler and N.F. de Rooij, "Micr-electromechanical systems for nanoscience", Journal of nanoparticle Research 2, pp. 413-418, 2000

Conference and workshop papers

Related to this thesis

S. Gautsch, T.Akiyama, N.F. de Rooij, U. Staufer, Ph. Niedermann, L. Howald, D. Müller, A. Tonin, H.-R. Hidber, "Miniaturized Atomic Force Microscope for Planetary Applications", Proc. 9th European Space Mechanisms & Tribology Symposium, ESA SP-480, 11, Liège, Be, (2001).

S. Gautsch, T. Akiyama, N.F. de Rooij, U. Staufer, Ph. Niedermann, L. Howald, D. Müller, A. Tonin, H.-R. Hidber, W.T. Pike, "Development of an AFM Microsystem for Nanoscience in Interplantary Research", Proc: 3rd Round table on Micro/Nano-technologies for space – Scientific Payloads, 173, Noordwijk, NL, (2000).

S. Gautsch, T.Akiyama, N.F. de Rooij, U. Staufer, Ph. Niedermann, L. Howald, D. Müller, A. Tonin, H.-R. Hidber, W.T. Pike, M.H. Hecht," Atomic Force Microscope for Planetary Applications", Proc. Solid-State Sensor and Actuator Workshop, 267, Hilton Head Island, USA, (2000).

L. Howald, T.Akiyama, S. Gautsch, H.-R. Hidber, D. Müller, Ph. Niedermann, T. Pike, A. Tonin, U. Staufer, ”Development of the space SFM for interplanetary missions”, Proc. 4th Seminar on Quantitative Microscopy QM 2000, 209, Semmering, A, (2000).

W.T. Pike, M. H. Hecht, M.S. Anderson, S. Gautsch, T. Akiyama, N.F. de Rooij, U. Staufer, Ph. Niedermann, L. Howald, D. Müller, A. Tonin, H.-R. Hidber, “Atomic Force microscope for imaging and spectroscopy”, Proc. Concepts and approaches for Mars exploration, 6186.pdf, Lunar and Planetary Institute, TX, USA, (2000).

In other areas:

L. Dellmann, T. Akiyama, D. Briand, S. Gautsch, O.T. Guenat, B. Guldimann, P. Luginbuhl, C. Marxer, U. Staufer B. van der Schoot, N.F. de Rooij, “Microsystems for diverse applications using recently developed microfabrication techniques”, Proc. MOEMS and Miniaturized Systems, pp. 16-27. (Santa Clara, USA, 2000).

U. Staufer, T. Akiyama, C. Beuret, S. Gautsch, W. Noell, G. Schürmann, C. Stebler and N.F. de Rooij, “Micr-electromechanical systems for nanoscience”, Journal of nanoparticle Research 2, pp. 413-418, (2000).

L. Dellmann, S. Gautsch, G.-A. Racine, N. F. de Rooij, “New integrated axle fabrication for piezoelectric motors based on a rotor clip assembling operation”, Digest of Technical Papers 10th Internat. Conf. on Solid-State Sensors and Actuators, TRANSDUCERS '99, Sendai, J, pp. 1752-1755, (1999).

8. BIOGRAPHY

Sebastian Gautsch was born on October 13. 1975, in Zürich, Switzerland. He worked in the field of electronic circuits for welding machines at FAEL SA and in the marketing department of the company Mikron SA in Boudry, Switzerland. In 1999, he received his diploma in electronics-physics delivered by the Institute of Microtechnlogy (IMT) from the University of Neuchâtel, Switzerland. In March 1999, he joined the research group of Prof. N. F. de Rooij at IMT as a research and teaching assistant. His research interests include ultrasonic motors for the watch-making industry and the development of tools for nanoscience.